Supplementary Information

From time dependent incorporation of molecular building blocks to application properties for inorganic and organic three-dimensional network polymers

L. De Keer et al.

Supplementary Methods

Figure 2 in the main text highlights the concept of the developed generic framework in the present work to explicitly track the 3D chemical variation of each building block of each initial and formed molecule thus all functional moieties at specific user-defined synthesis times, so-called plotting times $t_{plot,i}$ (i=1, 2, ...) along the network synthesis. Two computational methods from two scientific fields are connected to be successful in this respect:

(i) ***Computational method 1*** comprises ***matrix-based kinetic Monte Carlo*** (*k*MC) simulations from the field of chemical kinetics in which (molar) concentration (C) changes of all distinguishable species are followed, hence, differentiating for species with a variation in composition and topology. This specifically implies that for a given network molecule one has information if each of its crosslinking points (CPs) is fully connected (so fully linked to other CPs) or still possesses (unreacted) functional group (FGs) or dangling chains not yet connected to other CPs. Internal loops due to intramolecular reactions, *i.e.* cyclization, are also tracked per network molecule. Molecular information on how the CPs are connected and the composition of the shared network segments between two CPs is additionally available. Also the composition of the dangling chains is known at any synthesis time t. No information on 3D configurations is although stored in matrix format and thus a 2D representation of all individual connectivities is strictly only possible based on the matrix-based *k*MC simulations only. A default transition to a 3D visualization can although be done by considering expected bond lengths and angles as linked to general statistical (e.g. Gaussian) functions.

(ii) ***Computational method 2*** comprises ***molecular dynamic*** (MD) simulations from the field of polymer physics, which allow to access for each well-defined or ideal structural element in the network polymer (*e.g.* the direct surrounding of a fully connected CP) a thermodynamically feasible 3D configuration. Hence, the MD data allow to obtain proper bond lengths and bond/dihedral angles for the involved atoms and FGs in the structural

element selected. The MD simulations can thus be utilized to spatially depict structural elements that are interconnected by the population of CPs as trackable with the *k*MC model. Correction factors, as developed in the present work, are considered in case a structural defect thus non-ideality (e.g. due the occurrence of an intramolecular reaction) needs to be represented in 3D format. Corrections on bond lengths and angles are thus needed as typical MD simulations focus on a basic number of reaction possibilities for the bulk and thus well-connected part of the network material.

In this section, the specific details of the communication between both computational methods (**first part** and **second part** of the Supplementary Methods section) are provided, starting from three flowsheets and a conceptual figure on (reaction event) stochastic sampling that are included as Supplementary Figure 1-4 and which cover (i) the main consecutive steps in the underlying numerical algorithms through the introduction of labeled boxes (A to N) and (ii) the input parameters of which some need to be updated along the simulation. Notably Supplementary Figure 2 is embedded in Supplementary Figure 1, and Supplementary Figure 3 in turn in Supplementary Figure 2. We have thus two links with the first from Supplementary Figure 1, being the core kinetic Monte Carlo (*k*MC) algorithm, to Supplementary Figure 2, which allows to retrieve molecular information on individual connectivities, bond lengths, bond angles, and dihedral angles for a molecule selected. In Supplementary Figure 2, we differentiate between ideal and non-ideal structural network elements, which can be automatically verified as the *k*MC algorithm allows to determine whether a given network molecule has locally structural defects due to internal loops or not. For the ideal structural elements that are thus thermodynamically stable we utilize the second link thus the one going from Supplementary Figure 2 to Supplementary Figure 3, which contains the detailed MD computational steps. For the non-ideal elements we have in Supplementary Figure 2 an extra modification, as explained further.

In the present work, as discussed in detail in the Supplementary Discussion, we follow a general approach for the determination of the aforementioned kinetic input parameters for all three chemistries, with in a first phase the consideration of reaction conditions in which we have no impact of diffusional limitations or viscosity effects. This can be the consideration of lower synthesis times for actual network

synthesis or the direct examination of intrinsic kinetics with monofunctional analogues. In a next phase, we use the already determined chemistry kinetic parameters as input in a detailed network kinetic model to tune the remaining diffusional limitations related parameters.

For illustration purposes, in this Supplementary methods section, focus is on batch isothermal chemistry, hence, all reactants are present at the start of the polymer synthesis and no temperature variations are allowed. The algorithms are however easily extendable to semibatch and non-isothermal operation modes, following the principles as outlined in our previous work on chemical kinetics for linear copolymers.[1-4] Alongside the aforementioned two parts with the first part covering the details of computational method 1 and the second part the details on computational method 2, a **third part** is included in the current section addressing the a posteriori calculation of molecular properties. For each part, a new page is commenced.

The main steps of the ***matrix-based kMC algorithm*** or thus the main principles of ***Computational method 1*** (Part 1 of the Supplementary Methods section) are shown in Supplementary Figure 1, employing boxes that are labeled by a capital letter ranging from A to I to facilitate the description of the method. A link is made to Supplementary Figure 2 based on the box with Label I in Supplementary Figure 1. This box addresses the feature to plot detailed simulation results at the aforementioned plotting times ($t_{plot,i}$ values), including the possible linkage with the MD simulation results (Computational method 2) to enable a 3D visualization of individual (network) molecules.

The matrix-based *k*MC algorithm Supplementary Figure 1 starts at t = 0 s. The associated input parameters are highlighted in the box with Label A. The algorithm requires (i) a list with all reaction types or so-called MC reaction channels as defined based on FGs with the total number of reaction types abbreviated as $tot_{nr,rt}$ and a single MC reaction channel as ν; (ii) the functionalization degrees (fd values) of the monomers or building blocks enabling crosslinking (*e.g.* bi- or trifunctional monomers; fd value of 2 or 3 respectively); (iii) the polymerization temperature (T_p) and pressure (p_p); (iv) a list of all intrinsic kinetic (*e.g.* Arrhenius) and molecular diffusion (*e.g.* free volume theory; FVT) parameters, with the former enabling the calculation of the intrinsic rate coefficients, *i.e.* the k_{chem} values, and the latter the calculation of the (molecular) diffusion rate coefficients, *i.e.* the k_{diff} values; (v) the initial concentrations (initial C values; thus C_0 values); (vi) the initial total number of molecules ($n_{tot,0}$) allowing to calculate the initial MC simulation volume V_0; (vii) the total simulation time (t_{tot}) and the plotting times ($t_{plot,i}$; i=1, 2, ...); and (viii) the initial physicochemical properties, *e.g.* the initial individual densities (ρ_0 values) and the molar masses of all molecule types (MM values).

Note that $n_{tot,0}$ should be sufficiently high to enable a stochastically correct representation of the chemical kinetics. This can be tested by its gradual increase until numerical convergence is reached (example: Supplementary Figure 16) in line with previous *k*MC simulations on the synthesis of linear or slightly branched (co)polymers.[5,6] For the reaction types a distinction can be made between several main and side reactions, which is a strong point of kinetic modeling approaches in which easily a high number of reaction types can be considered (*e.g.* up to 100).[7,8] It should be stressed that the k_{chem} values in the box with Label A are defined based on the FGs involved and are denoted as single-event chemical rate

coefficients (cf. Fig. 2a in the main text). Hence, if a molecule contains four FGs of the same chemical composition it can react four times with the same k_{chem} value provided that there is no effect of the local environment (case of one reaction type with four reaction possibilities) or with four different k_{chem} values if the opposite is valid (case of four reaction types each with a single reaction possibility as the presence of already reacted FGs now matters upon a further modification of the chemical environment around the CP). To allow for a realistic value of $tot_{nr,rt}$ and thus the overall number of kinetic parameters (cf. 2 Arrhenius parameters per reaction type and several related molecular diffusion parameters) we perform lumping (e.g. Supplementary Figure 8-10) but still ensuring a sufficient representation of (groups of) reactions with an essential different (intrinsic) reactivity or leading to the creation of essentially different chemical structural (network) elements.

Examples of input variables according to this ordering from (i)-(vii) for the box with Label A are provided in Supplementary Table 1-3, selecting the three network syntheses considered in the main text. Chemistry 1 corresponds to organosilica network synthesis, chemistry 2 covers epoxy-amine curing, and chemistry 3 focuses on Diels-Alder reactions. Note that inter- and intramolecular reactions are considered separately as they are respectively bimolecular (intermolecular) and unimolecular (intramolecular) reactions, leading to different structural elements.

Upon providing all input parameters in the box labeled A an initialization is performed as highlighted in the box with Label B, e.g. all the elements of matrices associated with the composition of network molecules (so molecules with connected CPs) are given a value of 0 as no network molecules are present yet. Also based on the input in the box labeled A, the initial number of molecules and concentrations of all molecule types (example given in Supplementary Table 1; organosilica synthesis case) are calculated as well as the individual initial numbers of FGs.

In the next box labeled C in Supplementary Figure 1, we calculate at a given time t (first entry at t=0 s; later on entries per (stochastic) time step τ) the so-called microscopic Monte Carlo (MC) rates for all individual reaction types ($R_{MC,i}$; i=1, ..., $tot_{nr,rt}$). These rates are by definition expressed in s^{-1} and thus highlight how many times the reaction type is (mathematically) expected to occur per second. This implies that for intermolecular reactions a correction for the simulation volume V is made, reflecting

that for a given number of reactants intermolecular reactions are less likely for larger volumes. This explains why k_{chem} values are translated into k_{mic} values to enable a reaction rate calculation as a turn over frequency, e.g. $k_{mic}=k_{chem}\ (VN_A)^{-1}$ for an intermolecular reaction, with N_A the Avogadro number. Also correction factors are employed if the reactants are distinguishable species or not (factor 2 omitted or incorporated in the denominator of k_{mic}).[9-11] Note that for a given reaction type chain length dependencies can be relevant as well. At this stage, a representative reactivity is considered for the complete population with as explained below a continuous correction (so reaction by reaction event) for chain length dependencies ones the actual individual species need to be selected.

Moreover, as explained in the Supplementary discussion, in general, k_{chem} values for intermolecular (thus bimolecular) reactions need to be replaced by values for apparent rate coefficients (k_{app} values), which implies for the example above that $k_{mic}=k_{app}\ (VN_A)^{-1}$ and thus apparent MC rates can be observed in practice.[12,13] These k_{app} values are needed to account for a possible influence of diffusional limitations thus a deviation from intrinsic reaction rates (cf. Fig. 3b in the main text), as the observed reactivity related to a given reaction type can be codetermined by both the intrinsic reactivity and the diffusivity of the reactants and their FGs involved, taking into account the increasing dynamic viscosity of the reaction mixture (η) upon progression of the network formation. For extremely slow diffusivities (low diffusion coefficients; low *D* values), the rate determining step can even become the (intermolecular) diffusion rate coefficient k_{diff} (Supplementary Equation (6)) which is the counterpart of k_{chem} in the equation to calculate k_{app} (Supplementary Equation (5); also included in box C in Supplementary Figure 1). For the calculation of k_{diff} chain length dependencies are highly expected,[14,15] with a slower diffusion for larger species. A different mobility is also expected for macrospecies containing a different amount of CPs. In general, at higher polymer network yields one can expect a strong impact of diffusional limitations for intermolecular reactions on the observed kinetics. This aspect is often ignored even in kinetic modeling studies although more recent conventional so not matrix-based *k*MC simulations on network formation already proved that such limitations are crucial to fully grap the kinetics at larger *t* values.[16] Furthermore, it is well-known that for the accurate description and design of the synthesis of linear polymers diffusional limitations need to be accounted for.[17,18] For illustration purposes

Supplementary Figure 18 (organosilica case) highlights the relevance of diffusional limitations toward higher polymer network yields for intermolecular reactions by formally altering the apparent rate coefficients so by performing a sensitivity analysis. For intramolecular reactions possible diffusional limitations are also accounted for but this is done in a separate box labeled F in Supplementary Figure 1, as explained further and with a similar sensitivity analysis included in Supplementary Figure 19.

Based on the total (apparent) MC reaction rate ($R_{MC,tot}$), which is sum of the (apparent) MC rates for all the reaction types ($R_{MC,i}$; i=1, ..., $tot_{nr,rt}$)), the stochastic time for the next reaction type to be executed (τ introduced above) is subsequently calculated in the box with Label C in Supplementary Figure 1. For this purposes a random number r_1 is considered as put forward in the original Gillespie algorithm[9] so that the computational results at $t = t+\tau$ are generated based on the MC reaction rates at t. Note that for sufficiently high total reaction rates the reactions are almost executed immediately (low τ), whereas toward the end of the chemical process a (slight) delay is accounted for. Then in the box labeled C the microscopic (apparent) MC rates for the reaction types are converted into reaction type probabilities ($P_{MC,i}$; i=1, ..., $tot_{nr,rt}$). From these probabilities a cumulative probability curve is constructed, as illustrated in Supplementary Figure 4 again selecting the organosilica network synthesis case with for illustration purposes only the 6 reaction types from Supplementary Figure 5. In the latter figure, there is no distinction between inter- and intramolecular reactions and it is assumed that reverse reactions are kinetically relevant. Hence, the 6 reaction types in Supplementary Figure 5 correspond to 3 chemical processes labeled as (1), (2) and (3) in this figure.

The next box labeled D in Supplementary Figure 1 addresses a second random number generation (random number r_2) to select the reaction type taking place at $t + \tau$, based on the cumulative curve generated in the box labeled C, as illustrated by y-axis random sampling in Supplementary Figure 4 and in agreement with the original method of Gillespie.[9] This random sampling on the y-axis generates a number between 0 and 1 (here 0.15) with reactions characterized by a higher probability more favored, highlighting the correct relation between the random selection and the reaction probabilities at each t.

The next step is the stochastic identification of the reactants involved so the determination of the actual species containing the FGs linked to the microscopic MC rates. If the reactants contain already reacted

FGs the box labeled E is subsequently considered. To set the mind one can focus here on reaction type 3 in Supplementary Table 1 (intermolecular water condensation in organosilica synthesis, hence, the reaction of two OH FGs located in two different (network) molecules containing several or at least one OH FG). One first stochastically selects a first FG A (so first OH) out of the total population of such groups using a functional group binary sampling tree (Part 1 in box E in Supplementary Figure 1). The use of trees to store structural information has been previously put forward in the field of polymerization kinetics at Ghent University and by collaborators.[19-21] Each leaf node (bottom row of the functional group binary sampling tree) represents a (network) molecule and the number stored is the amount of free (available/unreacted) FGs in that specific molecule. Also a functional group sampling matrix is considered (Part 2 in box E in Supplementary Figure 1), which contains a number that locates the specific FG in the key composite topology matrix. The latter matrix, which is updated in the box labeled G and which contains numbers highlighted in the same color (orange) as the functional group sampling matrix to visualize the link with box E, contains for all molecules in the *k*MC volume the individual connectivities and compositions and specifically stores the local chemical environment around the selected FG. Similarly one can use the sampling tree and matrix to select the possible second FG B (so selection of the second OH for the same example from before; Part 3 in box E in Supplementary Figure 1). It can be automatically checked if this second group belongs to another molecule as required for the example of an intermolecular reaction. For an intramolecular reaction one can have automatically the opposite check so one is able to ensure a selection of two FGs from the same molecule.

As explained above there is a direct link between the box labeled E - with the selection of FGs of multifunctional reactants based on reaction probabilities - and the box labeled G covering the update of the overall network chemical make-up due to the former selection(s). Here the core of the matrix-based *k*MC algorithm is located as the composite topology matrix stores the composition of all segments (matrix T in the middle) and the connectivities of all segments with respect to the CPs (two vertical arrays left and right of the former matrix; CA_1 and CA_2). Note that this combination of a matrix and two arrays, as introduced in the present work, explains the use of the concept composite matrix. For

intermolecular crosslinking, the created segment is highlighted by explicitly updating that it is now connected between two CPs (now non-zero values in CA_1 and CA_2).

For intramolecular reactions, a direct update of the box labeled G is not done but first it is checked (box labeled F in Supplementary Figure 1) if the selected FGs are sufficiently close to each other so that such reaction can physically occur, *i.e.* the intramolecular diffusion of the selected FGs in the selected molecule is sufficiently fast to bring these groups at reaction distance σ. For this a fundamental distance rule is applied, as explained in the Supplementary discussion and with the key formula depicted in the box labeled F in Supplementary Figure 1. If the selected FGs are not suited two new FGs are selected and thus the algorithm goes back to the box with Label E. Upon evaluation of the running algorithms the number of redirections is very limited, highlighting the relevance of this approach.

The next box H in Supplementary Figure 1 covers the update of the number of molecules and concentrations so that one is able to update the reaction probabilities (switch from t to $t+\tau$, the latter becoming the new t) as defined based on the reaction types. Note that such update can be done without the update of the composite topology matrix in case the reaction type selected involves basic reactants (*e.g.* a conventional initiator dissociation in hydrogel synthesis). Before doing this update, which relates to the closing of the main internal loop in Supplementary Figure 1 (so back to the box labeled C), it is checked if one wants to plot (thus at one of the input plotting times; $t_{plot,i}$ values) intermediate concentrations (*e.g.* the concentrations of several types of molecules such as monomer, dimer, and network molecules with for instance x crosslinking points) or to plot the structure of the individual network (or remaining initial/branched) molecules (box labeled I in Supplementary Figure 1) at the selected t. The closing of the main internal loop in Supplementary Figure 1 is ended if the final synthesis time (input parameter t_{tot}) is reached (end element in flowsheet in Supplementary Figure 1 on top left).

As indicated in Supplementary Figure 1, the details of the additional plotting features of the box labeled I are covered in Supplementary Figure 2. Here we have the possibility to focus on different levels of molecular detail in view of the desired application (cf. the consecutive plotting questions in the left panel of Supplementary Figure 2). Note that one can decide to simply plot conventional kinetic information and not to depict 2/3D structures, e.g. one can focus on a so-called univariate description of a distributed

property, e.g. the molar mass distribution (MMD) with the variate being the total MM for a molecule type or all types together. A derived (average) characteristic can be the number or mass average molar mass (M_n and M_m). The bivariate analogue of an MMD is not limited to a differentiation based on only MM but adds also the variation of e.g. the average content of a certain comonomer type so that focus can be on the copolymer composition – MMD. Alongside univariate or in general multivariate characteristics, the individual network molecules can be represented in 2D or 3D format. The former can be directly performed based on the information of the composite topology matrix from the *k*MC simulations, whereas the latter requires the input from e.g. MD simulations (see details in next part).

In order to visualize the 2D and 3D network structure of individual molecules in Supplementary Figure 2 (box I in Supplementary Figure 1) the external programs Gephi and GaussView have been used.[22, 23] To facilitate the communication with these programs the information stored in the composite topology matrix is translated in other matrix formats, as highlighted by the box labeled J in Supplementary Figure 2 for 2D visualization, and the boxes K and L in Supplementary Figure 2 for 3D visualization. For 2D visualization, a list of connected nodes and edge lengths needs to be obtained. A label is given to the (remaining) FGs (e.g. the label A and B) according to the types of FGs (or the types of moieties containing a certain FG). The list is saved and used as input file for Gephi. For 3D visualization, internal coordinates need to be determined and stored for the composition of every network molecule (box labeled K in Supplementary Figure 2). For every atom or atom group in each molecule (e.g. the (atom) groups A or B), it needs to specified to which other atom(s) or atom group(s) it is connected, while acknowledging the chemical nature of CP thus the chemical structure of the moiety defining CP (e.g. C). Also bond lengths, bond angles and dihedral angles need to be identified (box labeled L in Supplementary Figure 2). As highlighted above starting/default values based on basic statistical distributions can be used.

In ***computational method 2*** (Part 2 of the Supplementary Methods section) the aforementioned bond lengths and angles for box L in Supplementary Figure 2 follow from ***MD simulation*** results (box labeled M in Supplementary Figure 2) of which the general principles are outlined in Supplementary Figure 3, focusing on the organosilica network case with the application of the Large-scale Atomic/Molecular Massively Parallel Simulator (LAMMPS), as previously done by Stanford University.[24,25] Upon proper manipulation of the raw MD data (cf. Supplementary Figure 3a) distributions of bond lengths and bond/dihedral angles (examples at bottom right of Supplementary Figure 2) can be generated that define thermodynamically feasible configurations (cf. Supplementary Figure 3b). As for the selection of chemical reaction types (box labeled D in Supplementary Figure 1), cumulative distributions (cf. Supplementary Figure 4) are constructed and additional random numbers are used to stochastically deliver the lengths and angles per atom (group) in the selected network molecule. Again more likely lengths and angles are automatically selected as the original Gillespie principles[9,10] are followed although now for a molecular property distribution.

In Supplementary Figure 3b it is shown in detail how the aforementioned distributions on bond lengths, and bond and dihedral angles are obtained from the output of LAMMPS that describes the equilibrated molecular network structure. The simulated annealing approach is used to generate the model molecular network, in which the NPT ensemble is performed on a cubic simulation box with periodic boundary conditions that contain randomly distributed precursor main building blocks (e.g. Si, Si-C-C-Si) and a certain number of free oxygen atoms to achieve a desired level of condensation degree which can at most reach unity. Typically, simulations are done with three different initial random distributions of the precursor main building blocks and free oxygen atoms and average final distributions of bond lengths, bond angles and dihedral angles are calculated. However, it is challenging to achieve a full network condensation in experiments due to steric hinderance effects, thus the model networks are formed such that the condensation degree is lower than unity. Likewise, condensation degree is set to be around 0.9 for the fully dense silica network model used in this study. NPT dynamics is preferred as it enables pressure control and volume relaxation depending on the network connectivity or the type of precursors used to generate the system. Harmonic bond length and bond angle potentials are defined for the bonded

interactions between the atoms that belong to a precursor molecule. Dihedral potential parameters are modeled with the OPLS potential function. All bonded interaction parameters were generated through ab-initio bond, angle and dihedral angle energy scans completed in GaussView. In the case of a silica network, no bonded interactions are defined. Hydrogen atoms are implicitly modeled with the united atom approach.

First a soft potential is applied to prevent the presence of overlapping atoms in the simulation box that has randomly distributed precursors and oxygen atoms. Simulated annealing starts after the soft potential is completed at which the temperature of the system is decreased linearly from 12000 K to 6000 K over 10000 one-femtosecond timesteps, and then from 6000 K to room temperature (298 K) over 100000 one-femtosecond timesteps. Similarly, the pressure of the system is decreased linearly from 90000 bar to 60000 bar over 10000 one-femtosecond timesteps, and then from 60000 bar to 1 bar over 100000 one-femtosecond timesteps. The system is then relaxed at room temperature and pressure for another 20000 one-femtosecond timesteps to obtain the final equilibrated (ideal) network structure. An empirical Stillinger-Weber potential is used to define the non-bonded interactions during the simulated annealing process.[24,25] The potential parameters for the empirical Stillinger-Weber potential field were calibrated based on the NMR spectra results obtained from experimentally synthesized glasses. Stillinger-Weber potential enables accurate modeling of both two body and three body terms in the network (i.e. Si-O bonds and Si-O-Si and O-Si-O bond angles). The potential parameters for the interaction between the non-bonded atoms were calibrated to be repulsive. Radial distribution functions and bond/angle distributions of the final equilibrated networks match well with experimental values.[24,25]

The temperature and pressure schedule, as well as the number of time steps were all calibrated to achieve the lowest energy configuration that will yield a density within 5% of the experimental values. Once the structure is equilibrated, an adjacency matrix is formed through post processing representing the connectivity of the network. Via a loop over the adjacency elements, e.g. bond pairs, triplet of atoms and groups of four atoms are identified and grouped based on their types. The corresponding bond distance and angles (bond/dihedral) are then jointly represented by the introduction of distributions.

As indicated above, the MD calculations relate to the 3D structure of ideal bulky (so well- thus strongly connected) network elements and thus not to e.g. the non-ideal structural elements related to intramolecular reactions and consequently loop formation. As every connectivity is stored in the composite topology matrix in the *k*MC simulations (box G in Supplementary Figure 1) one knows if the selected structural element is due to an intramolecular reaction and thus a proper correction can be made in the box labeled N in Supplementary Figure 2 regarding the angles and lengths under non-ideal configurational conditions. The reasoning behind these corrections is covered in the Supplementary discussion (see examples in Supplementary Table 5: organosilica case). The final internal coordinates are saved in a file per network molecule. Upon repeating the loop (n_{mol}=n_{mol}+1) containing the boxes K, L and M in Supplementary Figure 2 until the total number is reached n_{mol} =$n_{mol,tot}$ all the required files are generated and can be directly used as input files for GaussView. Also the remaining linear/loosely branched molecules can be depicted if desired.

It should be repeated that in case no reliable MD data are available for a given network polymer chemistry one can use typical average lengths and angles from literature or use simplified Gaussian distribution around these typical averages (alternative or default input for box M in Supplementary Figure 2). In a broader context, at any moment progress in the MD field (e.g. on polymer-solvent interactions) can be translated to the generic multi-scale platform in the current work as only input files are required (cf. the plug in of Supplementary Figure 2 in the flowsheet represented by Supplementary Figure 1). This illustrates the long-term potential of the development tool, highlighting the relevance of combining research from the fields of chemical kinetics and physics.

For the **a posteriori calculation of a broad spectrum of molecular properties** (Part 3 of the Supplementary Methods section) the information stored in the composite topology matrix can be employed as well. Here we can focus for instance on the molecular pore size distribution (mPSD). In the present work, the starting point is the algorithm developed by Johnson,[26] which is an optimization of the algorithm developed by Tiernan[27] in terms of time complexity. This algorithm was originally employed to generate the complete set of closed elementary trajectories in mathematical graphs, implying the presence of each CP only once. First, a so-called mPSD connectivity matrix is constructed out of the composite topology matrix (box labeled G in Supplementary Figure 1), summarizing only connectivities between all CPs, i.e. for every CP it is stored to which other CPs it is connected and what the corresponding segment length is. Subsequently, a process of path extension is conducted identifying for every path whether a closed trajectory or molecular pore is formed, while making sure that all paths of each network molecule are elementary and only considered once. A list of all molecular pores (thus number frequencies) in terms of the number of CPs included and the corresponding molecular pore sizes result, which can be translated in a straightforward way to the mPSD (example: Figure 3 (bottom layer) in the main text).

Another example is the calculation of the hydrophilicity, as used in Figure 3a in the main text (chemistry 1). Hydrophilicity is defined in this work as the fraction of hydroxyl (OH) groups at the surface of the network molecules. This macroscopic property is calculated using density-based outlier detection.[28] In this method, the density of each hydroxyl group is compared to the density of its neighboring atoms/atom groups. A hydroxyl group is identified as being at the surface (an outlier) if its density is relatively much lower than that of its neighbors. Density is defined as the number of atoms/atom groups within a certain distance of the atom/atom group under consideration and can be calculated based on the (x,y,z) coordinates of each atom/atom group from the 3D visualization. This procedure is applied to a representative number of network molecules and the hydrophilicity is calculated as the average fraction of hydroxyl groups at the surface.

Examples of other derived more conventional distributed properties are given in Fig. 4 in the main text and Supplementary Figure 20.

Supplementary Discussion

As highlighted in Supplementary Figure 1 (box labeled A) we need input parameters to run the matrix-based kinetic Monte Carlo (*k*MC) simulations (Computational method 1; full details in the Supplementary Methods section above). Some of these input parameters need to be updated along the *k*MC simulation so from synthesis time t = 0 s to the final synthesis time t=t_{tot}. For example, diffusion coefficients (D values) as required for the calculation of diffusional rate coefficients (k_{diff} values; box labeled C in Supplementary Figure 1) are a function of the (network) polymer yield or the dynamic viscosity of the reaction mixture (η), and need to be updated upon the execution of reaction events (box labeled H in Supplementary Figure 1).

In what follows, the main aspects of the calculation of input parameters are highlighted focusing consecutively on (i) chemical rate coefficients (k_{chem} values; ***parameter set 1***) as needed to reflect the competition between main and side reactions on the intrinsic level; (ii) apparent rate coefficients (k_{app} values; ***parameter set 2***) as needed to correct for possible diffusional limitations so updating k_{chem} values by k_{app} values; (iii) diffusional rate coefficients (k_{diff} values) and diffusion coefficients (D values; both ***parameter set 3***) to enable the calculation of the aforementioned k_{app} values, and this all (so (i)-(iii)) for bimolecular thus intermolecular reactions. Finally, the focus is shifted to the parameters for the kinetic representation of unimolecular thus intramolecular reactions (***parameter set 4***), covering both the chemical and diffusional contributions, including for the latter contribution the explanation of the distance rule (box F in Supplementary Figure 1).

During the discussion regarding parameter set 1 also the detailed explanation of the synthesis and analysis procedures is included. Moreover, we follow a generic approach with first emphasis on the lower network synthesis times or the deliberate use of monofunctional analogous to enable the determination of chemistry related parameters without bias due to diffusional limitations. Once these chemistry related parameters are available they are utilized as fixed parameters in a detailed network kinetic model to describe large time network synthesis data to further tune the diffusional limitations related parameters. Hence, the current work has an inherent mitigation regarding parameter correlation.

Parameter set 1 (***k_{chem} values; intermolecular reactions***) is determined for the three network chemistries in the main text based on the experimental data in Supplementary Figure 11 and 12 (network chemistry 1; organosilica case; main focus in the main text with results displayed in Figure 2, 3 and 4a), Supplementary Figure 13 (network chemistry 2; epoxy-amine curing; results in Figure 4b in the main text), and Supplementary Figure 14 (network chemistry 3; Diels-Alder chemistry; results in Figure 4c and 5 in the main text). For the three chemistries the focus is first on parameter tuning based on experimental data that are recorded at small times with negligible or at most a minimal impact of side phenomena such as diffusional limitations or intramolecular reactions or experimental data based on monofunctional systems. Literature data are used for network chemistry 1[29] and for the other two chemistries own data are reported in the present work (cf. Methods section in the main text).

In what follows we discuss in detail the determination of the kinetic parameters for the three chemistries. For readability for each chemistry a new page is started. Also the future plans and potential with regard to expansion of experimental data sets are included, further demonstrating the general applicability of the developed approach.

For parameter set 1 for *network chemistry 1* (organosilica synthesis case; main case; start tetraethyl orthosilicate; TEOS), the general reaction scheme ignoring at this stage intramolecular reactions is given in Supplementary Figure 5 and is constructed around three reversible chemical processes denoted as (1), (2) and (3). It consists of hydrolysis (substitution of OH by OR; reaction 1 (forward) in Supplementary Figure 5), re-esterification (reverse hydrolysis reaction; reaction 1 (reverse) in Supplementary Figure 5), water-forming condensation (Si-O-Si bridging based on Si-OH and Si-OH merging; reaction 2 (forward) in Supplementary Figure 5), hydrolysis of siloxane bonds (reverse of water-forming condensation; reaction 2 (reverse) in Supplementary Figure 5), alcohol-forming condensation (Si-O-Si bridging based on Si-R and Si-OH merging; reaction 3 (forward) in Supplementary Figure 5), and alcoholysis (reverse of alcohol-forming condensation; reaction 3 (reverse) in Supplementary Figure 5). Note that in case the presence of reacted FGs matters many k_{chem} values need to be determined, namely 24 (4 times 6).

For illustration purposes, in the present work, we work at low pH thus acidic conditions for the organosilica case, considering the experimental data from Pouxviel et al.[29] The experimental procedure and conditions, starting with TEOS (R: ethyl group; Et) are summarized in the Methods section in the main text. Experiments are first analyzed for a small timeframe (up to 3 h; data in Supplementary Figure 11) compared to the gelation (thus network) timeframe (extra experimental data in Supplementary Figure 12a). This limitation in time is ideal to determine k_{chem} values based on a simplified kinetic Monte Carlo (*k*MC) model without the need to take into account diffusional limitations and the explicit network molecule topologies (no box G needed as in Supplementary Figure 1). These small-time experimental data are depicted as symbols in Supplementary Figure 11, with $Q_a(b,c)$ denoting a moiety with a Si atom with *a* bridging oxygen atoms, *b* OH ligands, and *c* OEt ligands. Supplementary Figure 11a focuses on the reactants and products of the first hydrolysis steps and Supplementary Figure 11b on the condensation product variations as a function of *t*. Supplementary Figure 11c focuses on overall FG characteristics. Following the work of Pouxviel et al.[29] a hydrolysis (*h*) and condensation (*c*) ratio are considered, as defined by:

$$h = \frac{X_{-OH} + X_{-O-}}{4X_{Si}} \quad (1)$$

$$c = \frac{X_{Q_1} + 2X_{Q_2} + 3X_{Q_3} + 4X_{Q_4}}{4X_{Si}} \quad (2)$$

with X_{-OH} the number of OH groups, X_{-O-} the number of bridging oxygens, X_{Si} the number of Si atoms, and X_{Qi} the number of Si atoms with *i* bridging oxygens. As also depicted in Supplementary Figure 11c from the varying *h* and *c* values the evolution of the number of OR (τ_{OR}) and OH (τ_{OH}) remaining FGs can be obtained:

$$\tau_{OR} = 1 - h - \frac{c}{2} \quad (3)$$

$$\tau_{OH} = h - \frac{c}{2} \quad (4)$$

In Supplementary Figure 8a, it is shown how we track the organosilica species types (the *Q* species introduced before) during the small time *k*MC simulations to tune the majority of the k_{chem} values based on the experimental data in Supplementary Figure 11. Information about the ligands of each Si atom is stored in a so-called composition of building blocks (BB) matrix covering in the first column the number of bridging O atoms, in the second column the number of OH ligands, and in the third column the number of OEt ligands. In Supplementary Figure 8b, it is shown how we lump the individual hydrolysis and condensation reactions into 6 reaction types. As explained below not 24 k_{chem} values are needed but a determination of 7 k_{chem} values (6 forward rate coefficients and 1 reverse rate coefficient) suffices for the timeframe considered that is well below strong gelation, as explained above. These k_{chem} values are reported in Supplementary Table 1 and their determination is discussed in the next paragraphs.

Previous kinetic studies[30,31] have showed that alcoholysis and hydrolysis of siloxane bonds are mainly important under basic conditions and can therefore be ignored in alcoholic solutions at low pH. There is thus no need of the consideration of the reverse reactions for chemical processes (2) and (3) in Supplementary Figure 5 in the present work. In other words, we a first sight go from 6 unknown k_{chem} values to 4. It has also been highlighted that the hydrolysis in alcoholic solutions (chemical process (1) in Supplementary Figure 5) strives for equilibrium. Such hydrolysis occurs with a transition state with S_N2-type character,[30] with in the forward direction the water molecule attacking from the rear and acquiring a partial positive charge. Notably, preliminary parameter tuning highlighted that the reverse

hydrolysis can be neglected for the smallest times. A shown in Supplementary Figure 12a we can focus at experimental data up to 3 h to avoid the impact of the reverse reaction of process (1). This observation apparently lowers the number of k_{chem} values from 4 to 3, at least at these smallest times as covered in Supplementary Figure 11. There only forward reactions need to be considered. However, the (forward) hydrolysis rate coefficient is dependent on the type of ligands on the Si atom. That is why correction factors (f_4, f_3, f_2 and f_1), as defined in Supplementary Figure 8b, are introduced. So at low times we need to eventually determine 6 forward rate coefficients.

Note that the subscript for f corresponds to the number of remaining OEt groups, explaining the reverse ordering starting with 4 for the original TEOS molecule. For the condensation reactions, which mechanistically involve the attack of nucleophilic protonated silanols on a neutral silicate species, lumping is although afforded. This increases the number of k_{chem} values to be determined (and thus the number of reaction types) only from 3 to 6 for the smallest times. The values of the aforementioned 4 correction factors are determined by the interplay of steric and inductive effects and follow from a comparison of modeled and experimental data, as the ^{29}Si NMR spectrum in Supplementary Figure 11a exhibits five peaks with different t locations of the maximum values, corresponding to the initial TEOS monomer $Q_0(0,4)$ and the four silanol species $Q_0(1,3)$, $Q_0(2,2)$, $Q_0(3,1)$, and $Q_0(4,0)$. Consistent with the hydrolysis mechanism, the hydrolysis rate is increased by substituents which reduce steric crowding around Si, *e.g.* by replacing the first OEt of TEOS by OH one obtains $f_3 > f_4$. Electron withdrawing substituents (-OH) destabilize however the positively charged transition state under acidic conditions therefore decreasing the further hydrolysis rate and explaining why for the subsequent substitutions one observes $f_3 > f_2 > f_1$. This reducing effect is although still limited so that it still holds that $f_1 > f_4$. The relevance of this differentiation based on f values is additionally highlighted in Supplementary Figure 11d which clearly shows that with equal f values (dashed line) the relative experimental positions of species types in Supplementary Figure 11a cannot be explained. Furthermore, it has been reported that the water-forming condensation rate is larger than the alcohol-forming condensation rate,[31] explaining the larger $k_{cond,W}$ value compared to the $k_{cond,A}$ value in Supplementary Table 1.

If we in a next step focus on the time evolution of the hydrolysis ratio *h* at larger times in Supplementary Figure 12a (e.g. from 3 hours onwards), it follows that its value decreases, while the condensation ratio *c* value keeps increasing. This shows that at sufficiently larger reaction times, the reverse hydrolysis reaction starts to play a role. The rate coefficient of this reesterification reaction is determined from the large-time data in Supplementary Figure 12a and represents the 7th and last intermolecular k_{chem} value in Supplementary Table 1. The relevance of this extra reactivity is highlighted in Supplementary Figure 12b (mismatch with dashed lines). Note that these large-time data are also used to describe the intramolecular reactivity (focus although on other responses; full vs. dashed lines Supplementary Figure 12c-d), as explained in the discussion of parameter set 4.

It should be stressed that parameters values in Supplementary Table 1 are in agreement with literature data[29,30] but are of a greater level of detail with respect to the state-of-the-art. There *f* values of 1 are mostly considered and the water- and alcohol-formation condensation reactivity are mostly the same. Thanks the stepwise consideration of certain experimental reponses or the specific time variation for such an experimental response we are capable to have such detailed chemistry related kinetic parameters. Note that in future work it is also interesting to further record experimental data as in Supplementary Figure 11 and 12 for other precursors than TEOS. Currently we are doing so to further study the relation of the material level with the molecular level.

It can be concluded that for the first network chemistry considered (the organosilica case) the simultaneous consideration of all experimental data in Supplementary Figure 11a, Supplementary Figure 11b, Supplementary Figure 11c (and Supplementary Figure 12a) allows to extract 7 reliable intermolecular k_{chem} values. An excellent agreement between experimental and modeled data is obtained in Supplementary Figure 11a and Supplementary Figure 11c. The match seems at first sight somewhat less in Supplementary Figure 11b but one should realize that a kinetic model can inherently correct for experimental inconsistencies in case the overall data set (so all experimental points in Supplementary Figure 11) is sufficiently large. This strength has also been recently demonstrated by Van Steenberge et al.[32] regarding the simulation of dispersity values in the synthesis of linear copolymers. To make the

larger uncertainty for the experimental data in Supplementary Figure 11b more clear we also included larger error bars here.

It is further mentioned here that besides Supplementary Eq (1)-(4) one can also put forward a conventional product yield for the organosilica case, as used in the top part of Figure 3 in the main text:

$$Yield = \frac{2X_{-O-}}{4S_{si}} \quad (5)$$

Note that on overall basis a successful crosslinking is associated with a loss of an O atom through the formation of solvent, explaining the extra 2 in the nominator. For example grouping process (1) and (2) in Supplementary Figure 5 leads to 2 alkoxysilanes and 1 water molecule going to one desired –O- crosslink and 2 ethanol molecules. An extra solvent molecule with an extra O is thus created justifying the introduction of the extra 2, as the product yield is defined with respect to the targeted network molecule. Upon comparison of Supplementary equation (5) and Supplementary equation (2), it can be seen that the condensation ratio *c* actually represents the yield.

For parameter set 1 for *network chemistry 2* (epoxy-amine curing case), the general reaction scheme is provided in Supplementary Figure 6 and consists at first sight of only 3 reaction types (focus on only intermolecular reactions as for network chemistry 1 at this stage). The basic reaction of epoxides based on diglycidyl ether from bisphenol F (DGEBF) with primary and secondary amines involves the addition of respectively the primary and secondary amino groups of the amine to the epoxy group, with the simultaneous formation of one OH group, due to opening of the epoxy ring. Analogously with the first network chemistry *f* values are thus introduced to compared relative chemical reactivities in a direct manner. Literature data however indicate that similar (or even the same) intrinsic reactivities are obtained, leading to a random clicking of epoxy and amine FGs.[33] Reaction of the epoxy groups with the OH groups may also occur as a third reaction type (last reaction in Supplementary Figure 6), forming an ether group. However, this reaction type is mainly important if the amine is present in less than stoichiometric concentrations.[33] In the present work, such conditions are not selected (see Methods section in the main text and Supplementary Table 2).

Importantly, the OH groups formed by the amine/epoxide addition reaction act as catalytic species, accelerating the overall network formation and exhibiting the typical course of an autocatalyzed reaction.[33,34] Hence, for the simulation of the epoxy-amine curing autocatalytic reaction types are additionally used, as secondary alcohols are continuously generated. The OH groups catalyze the reaction through the formation of a trimolecular complex, which facilitates the nucleophilic attack of the amino groups. The relevance of this additional reaction pathway becomes clear upon the inspection of Supplementary Figure 13b. The dashed lines (case without the autocatalysis but aiming at similar rates) cannot provide the shapes in temporal FG concentration variations as experimentally observed in Supplementary Figure 13c.

In order to determine the intermolecular k_{chem} values experiments have been performed of which the procedure is summarized in the Methods section in the main text. A summary of the obtained chemical rate coefficients is given in Supplementary Table 2, according to the short notation in Supplementary Figure 9. The comparison between experimental and simulated data for the time evolution of the different FGs is represented in Supplementary Figure 13a. An excellent agreement is obtained. Again

the *t* values are very low (now minute scale to a couple of hours) to avoid the impact of side phenomena such as intramolecular reactions (more than a couple of hours). Consistent with the discussion above the k_{chem} values in Supplementary Table 2 are of that relative nature that (i) the autocatalytic effect is dominant (highest impact with $k_{PA,cat}$ and $k_{SA,cat}$), except at the very low *t* (non-zero value for k_{PA}) at which no OH is present, and (ii) formation of ether groups is negligible (zero value for $k_{ether,cat}$).

The parameters in Table 2 are in agreement with literature data[35] but it should be stressed that curing kinetics are typically studied in a quite formal way by considering differential scanning calorimetry. From such measurements one obtains the reaction heat that is translated in (approximate) conversion data to then use an overall kinetic model to tune less fundamental lumped parameters. This lumped character becomes further clear in previous models at the higher synthesis time with a very formal lumping of viscosity effects and not a detailed consideration of individual diffusion coefficient variations. Many kinetic models therefore only represent the overall conversion as function of curing time and temperature in a pragmatic manner, while from a fundamental point of view the progress of the different elementary reactions affects the molecular structure and macroscopic properties. In the present work, we consider an elementary reaction driven kinetic modeling approach from small to large synthesis times that this applicable to also other curing systems. Currently, we selected a model diamine to avoid steric hindrance issues but in general a more complex 3D incorporation pattern is expected. Novel experimental data are currently recorded and also the expansion to dynamic epoxy-amine systems, as relevant for recycling of thermosets or self-healing, is planned.

It can be concluded that also for the epoxy-amine curing case (second network chemistry) very reliable intermolecular k_{chem} values are obtained, benefiting from high frequency data recording (Supplementary Figure 13a) combined with *k*MC modeling focusing in essence at the disappearance and formation of FGs at the lower *t* values, as in the organosilica case (cf. Supplementary Figure 11).

For parameter set 1 for *network chemistry 3* (Diels-Alder synthesis case), the general reaction scheme (no intramolecular reaction yet) is presented in Supplementary Figure 7 (case with OH bilinker). The associated k_{chem} values are listed in Supplementary Table 3, following the FG definitions as outlined in Supplementary Figure 10 and considering the experimental data in Supplementary Figure 14 (procedure is summarized in the Method section in the main text). Here we were able to use the monofunctional analogues for the network formation to determine the associated intermolecular rate coefficient.

These chemical parameters are highly novel as this a quite recently introduced chemistry. In previous research emphasis was more on the self-healing potential of the network material and less on the its actual kinetics. In the present work, we selected this case study as a proxy toward drug delivery systems also considering 50% modification of the OH groups in Fmoc (see in detail in the Methods section in the main text). Here the long-term goal is to open the chemistry portfolio to both network chemistry following step- and chain-growth mechanisms and small and macromolecular initial building blocks.

With the chemical kinetic parameters determined for the three chemistries considered the focus can be now shifted to the ***calculation methods of k_{app} values*** (***parameter set 2***), which covers corrections for diffusional limitations (still only intermolecular or bimolecular reactions). As explained above, in polymerization chemistry, bimolecular reactions can become diffusion controlled, which implies that besides k_{chem} values we also need to consider (bimolecular) diffusional rate coefficients (k_{diff} values) describing how fast two molecules can diffuse to the reaction distance σ to enable the chemical reaction. In the present work, the fundamental encounter pair modeling approach[13,17,36,37] (Supplementary Equation (6)) is considered in combination with the Smoluchowski theory[38] (Supplementary Equation (7)) to calculate the k_{app} value for a given reaction type:

$$\frac{1}{k_{app}} = \frac{1}{k_{chem}} + \frac{1}{k_{diff}} \tag{6}$$

$$k_{diff} = 4\pi N_A \sigma D_{X1X2} \tag{7}$$

In Supplementary Equation (7), D_{X1X2} is the mutual diffusion coefficient for the considered reaction type as defined based on the reactants X_1 and X_2 containing certain FGs and σ is approximated by the Lennard Jones diameter (see Supplementary Table 1-3). Note that for slow diffusion ($k_{chem} >> k_{diff}$) we obtain $k_{app}=k_{diff}$ and for slow chemical reaction ($k_{chem} << k_{diff}$) we obtain $k_{app}=k_{chem}$. For intermediate cases, k_{app} is determined by both k_{chem} and k_{diff}, explaining the statement before that in general k_{chem} values need to be replaced by k_{app} values in Supplementary Figure 1. For a given reaction type (still intermolecular), D_{X1X2} can be obtained by summation of the individual or self-diffusion coefficients:[13,17,39]

$$D_{X1X2} = D_{X1} + D_{X2} \tag{8}$$

so that:

$$k_{diff} = 4\pi N_A \sigma (D_{X1} + D_{X2}) \tag{9}$$

In the discussion of the next parameter set we address the determination of these coefficients.

It is clear that to obtain the k_{app} values (still intermolecular thus bimolecular reactions; Supplementary Equation (6)) we need to have the individual diffusion coefficients (***parameter set 3; D values***) available. Here an important distinction exists between *non-macromolecules* (e.g. small monomer molecules) and *macromolecules* (e.g. polymeric species with for instance a certain number of monomer units and CPs). In the present work, *D* values are calculated based on the well-established free volume theory (FVT)[40-42] with universal scaling laws to account for the switch from non-macromolecules to macromolecules thus chain length dependencies, as explained in the next paragraphs. Note that at each time step in the matrix-based *k*MC algorithm the apparent rate coefficients for the reaction types are updated (box C in Supplementary Figure 1). If such rate coefficient for a reaction type is chain length dependent, either intrinsically or on the level of the *D* value or both, the apparent rate coefficient for a novel sampling is updated (box C in Supplementary Figure 1) based on the structural information of the last (two) macrospecies involved (e.g. the last (two) chain length(s); box H in Supplementary Figure 1). Such approach has already been shown successful in accounting for apparent chain length dependencies for bimolecular terminations in radical polymerization[43,44] and enables due to the fast stochastic sampling of reaction events (small τ values) to reflect the average apparent reactivity in case chain length dependencies matter for a reaction type.

According to the FVT theory the *D* value for a *non-macromolecule* X in the reaction mixture with N_{comp} components is given at a certain polymer mass fraction w_p by:

$$D_X = D_{0,X} exp\left(-V_X^* M_{j,X} \frac{\sum_{Y=1}^{N_{comp}} \frac{w_Y}{M_{j,Y}}}{\frac{V_{FH}}{\gamma}} \right) \quad (10)$$

in which V_{FH} is the specific hole free volume of the mixture, $D_{0,X}$ an average pre-exponential factor describing the ease of jumping of molecule X in the hole free volume available for diffusion, V_X^* the specific critical hole free volume required for a diffusional jump of X (accessible based on group contribution methods),[45,46] $M_{j,Y}$ the molar mass of a jumping unit of component Y (to a first approximation equal to the molar mass of the non-macromolecule), and w_Y the mass fraction of component Y in the reaction mixture. An average overlap factor γ is also introduced because the same

free volume is available for several jumping units. Note that Supplementary Equation (10) reflects the translational diffusivity of the non-macromolecule selected, as one can safely approximate the global diffusion as the movement of the theoretical sphere containing/surrounding the non-macromolecule.

The free volume related parameter $\frac{V_{FH}}{\gamma}$ follows from a weighted function of the specific hole free volume of the pure components ($\frac{V_{FH,Y}}{\gamma_Y}$ parameters):

$$\frac{V_{FH}}{\gamma} = \sum_{Y=1}^{N_{comp}} w_p \frac{V_{FH,Y}}{\gamma_Y} \tag{11}$$

In practice, we can focus only on those components having the largest mass fractions, typically monomer, solvent and polymer. The associated $\frac{V_{FH,Y}}{\gamma_Y}$ (Y = m,s,p) parameters can be estimated based on dynamic viscosity experimental data of the pure components (e.g. recorded with rheological measurements[47-49]) and applying regression analysis typically based on a constant expansion coefficient for the selected temperature interval, which mathematically relates to following temperature dependency:[50-52]

$$\frac{V_{FH,Y}}{\gamma_Y} = K_{1,Y}\left(K_{2,Y} - T_{g,Y} + T_p\right) \tag{12}$$

with K_{1Y} and $K_{1Y} - T_{g,Y}$ fitting parameters available in tabular format for representative non-macromolecules alongside estimated values for the pre-exponential factors $D_{0,Y}$.[50-52]

For the *D* value of *linear macromolecules*, chain length dependencies need to be accounted for (switch from D_X to $D_{n,linear}$ values with *n* the number of monomer units) and one needs to verify if other diffusion modes than the translational one matter. In this context, segmental diffusion corresponds to the reorientation of the actual FGs (or active centers) to execute the chemical reactions once translational diffusion has brought the theoretical spheres around the polymer coils containing these FGs in contact. Previous derivations of Barner-Kowollik and Russell[14] have although indicated that to a first approximation Supplementary Equation (9) can still be used based on translational *D* values, provided that one acknowledges the chain length dependencies and it is evaluated if a so-called reaction diffusion

term is needed. If two polymer coils are immobile their center of masses can still change if monomer can diffuse to the reactive centers. Due to the propagation reaction on an overall basis diffusion can thus still take place leading to an apparent variation of the translation diffusion coefficient, explaining the concept of reaction diffusion. This reaction diffusion contribution is proportional to the intrinsic propagation rate coefficient, the monomer concentration, and the mean-square end-to-end distance of the complete molecule ($< R_e^2 >$),[53,54] and needs to be added for the calculation of the apparent rate coefficient. For the selected chemistries in the present work the length of the linear molecules is although too small so that we can ignore the reaction diffusion correction. Furthermore, the chain length dependency of D for linear macrospecies can be normalized with respect to the monomer diffusion coefficient D_m bearing in mind that a linear macrospecies with a chain length of 1 is similar to a monomer molecule. Following universal scaling law has been e.g. determined for linear macrospecies:[55,56]

$$D_{n,linear} = \frac{D_m}{n^{(0.664+2.02w_p)}} \quad (13)$$

in which D_m is the monomer translational diffusion coefficient which can be calculated based on Equation (10), as monomer is a non-macromolecule. Note that for low w_p values (so low polymer yields or low t values) a Stokes-Einstein diffusion behavior is reflected (power for n close to 0.5) and for high w_p values (so high polymer yields or high t values) a reptation diffusion mode results (power for n close to 2).[13,57]

For *network (macro)molecules*, hence, non-linear molecules Supplementary Equation (13) needs to be further adapted (switch from $D_{n,linear}$ to $D_{n,network\ mol.}$) to reflect the impact of the number of CPs in the molecule (N_c), still defining n as the number of monomer units in the molecule. For the translational contribution, it has been indicated that the presence of CPs decreases the hydrodynamic volume of the molecules and, hence, increases the translational diffusion coefficient.[56] However, the presence of CPs also alters the segmental diffusion coefficient. As the bimolecular crosslinking reaction is significantly defined by the mobility of the FGs in the case of network molecules the latter diffusion mode can be seen at least to a first approximation as dominant and thus one expects on an overall basis a lower

mobility with an increasing relative number of CPs (ratio of N_c and n). In the present work, following update is therefore utilized for Supplementary Equation (13):

$$D_{n,network\ mol.} = \frac{D_m}{n^{(0.664+2.02w_p)(q\frac{N_c}{n}+1))}} \tag{14}$$

Note that in the absence of CPs (N_c=0) Supplementary Equation (13) is obtained and q is in general chemistry dependent with the resulting parameters listed in Supplementary Table 1-3. The q value is obtained by focusing on the time evolution of kinetic variables (or in the limit macroscopic properties) at larger times. Specifically for the organosilica case this implies the consideration of the experimental and simulated data in Supplementary Figure 12. For the epoxy-amine curing case a clear link with the storage modulus in Figure 4b in the main text is established. A tuned overall value of 7 is proposed in the present work. Note that at very high yield the number of network molecules goes down and the number of monomer units up. Also N_c increases but this is always constrained with respect to the number of monomer units. Hence, a very steep decrease is physically expected at higher synthesis times, as also induced in Supplementary Figure 19.

A final parameter set to be covered is ***parameter set 4***, which relates to the ***intrinsic and apparent reactivities of intramolecular reactions***, as the discussion above has been solely devoted to intermolecular or thus bimolecular reactions. The reaction between two FGs belonging to the same network molecule, hence, an intramolecular reaction is not always physically possible but is dependent on the 3D structure of the network molecule, from the very close environment (so at reaction distance σ; k_{chem} effect) to the local environment comprising the mobilities of the FGs selected (so k_{diff} effect; length scale much larger than σ).

Note that the (numeric value of the) intrinsic rate coefficient for a unimolecular reaction (as defined at σ) $k_{chem,intra}$ can be formally related to the corresponding (numeric value of the) intrinsic rate coefficient of the bimolecular reaction $k_{chem,inter}$. Based on extensive parameter screening and tuning to experimental yield data, a value of 0.2 is selected in the present work (see Supplementary Figure 18e). Furthermore, we use in the matrix-based *k*MC simulations a criterion that determines whether the FGs selected in the same network molecule based on overall MC reaction rates (so over all the FGs; box C in Supplementary Figure 1) can be brought to σ by intramolecular diffusion during the selected time step. This criterion, the so-called distance rule (box F in Supplementary Figure 1) covers the aforementioned k_{diff} effect and is related to previous studies on the Brownian motion of polymer network molecules. Specifically for a crosslinked melt in which most of the molecules/building blocks are linked by a crosslinking agent the mean square end-to-end distance for the direct thus local region as defined by the FGs ($< R^2_{e,FGs,local} >$) has been determined as:[49,58]

$$< R^2_{e,FGs,local} >= \alpha \frac{l^2 \cdot n'}{N'_c} \qquad (15)$$

with n' the number of monomer units along the shortest path between the two FGs in the network molecule and N'_c the number of CPs along this path, both structural parameters accessible based on the information in the topology matrix (box G in Supplementary Figure 1) and very likely lower then n and N_c, being the total values for the selected network molecule. In Supplementary Equation (15), l is the main bond length defining the monomer unit and α a correction factor to account for the influence of solvent-polymer interactions (and the excluded volume) on $\langle R^2_{e,FGs,local} \rangle$. The latter parameter is given

for illustration purposes a value of 1 in the present work but can be fine-tuned in follow-up work. As it can be expected that the observed intramolecular rate coefficient is inversely proportional to $< R^2_{e,FGs} >$, it can thus be postulated that $\sqrt{N'_c/n'}$ being a measure for the compactness needs to be sufficiently high for a given network molecule to allow for intramolecular crosslinking to take place. In the present work a default value of 0.5 is employed based on the sensitivity analysis in Supplementary Figure 18 (see implementation of this value in box F in Supplementary Figure 1).

It can therefore be concluded that for each selected pair of FGs in view of an intramolecular reaction it is verified based on fundamental principles (cf. Supplementary Equation (15)) if the reaction is allowed, benefiting from the potential of matrix-based *k*MC simulations to store all relevant structural information in the composite topology matrix. This again highlights why box G in Supplementary Figure 1 is seen as the core of Computational method 1.

Supplementary Figures

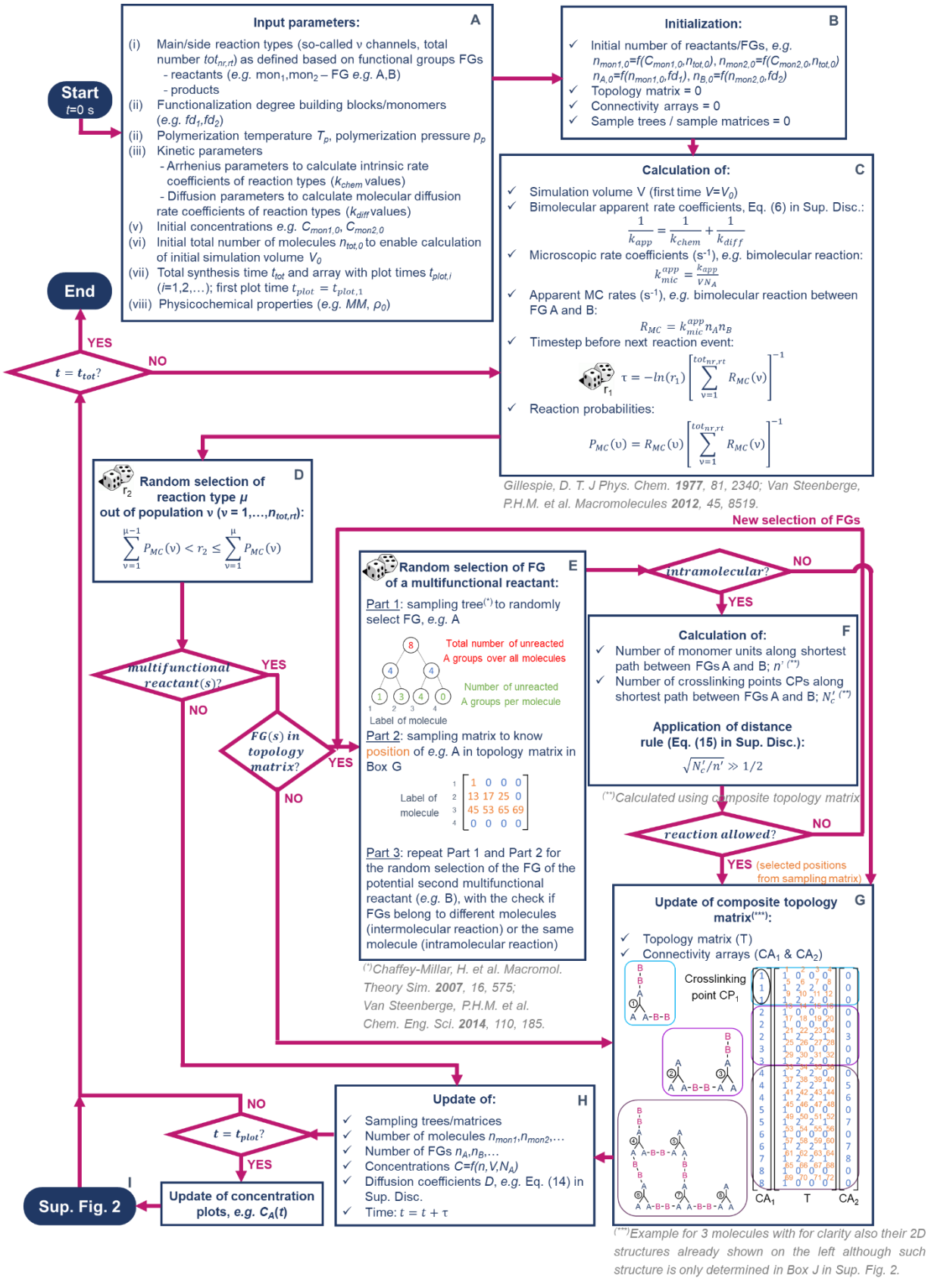

Supplementary Figure 1 with its caption provided at the top of the next page

Caption of Supplementary Figure 1:

Main steps of the developed matrix-based kinetic Monte Carlo (*k*MC) method (Computational method 1) in a flowsheet notation to enable a temporal tracking of the incorporation of each building block and all types of molecules from linear to highly crosslinked; functional group (FG) per FG is converted and tracked up to a final synthesis time (t_{tot}). At specific times we can plot (i) concentration changes (update of concentration plots) or (ii) uni- and multivariate characteristics (box labeled I with more details in Supplementary Figure 2) or (iii) visualize all individual molecules either in 2D or 3D format (also box labeled I with more details in Supplementary Figure 2). For the 3D format, a connection with molecular dynamic (MD) simulations (Computational method 2) can be made; isothermal batch synthesis.

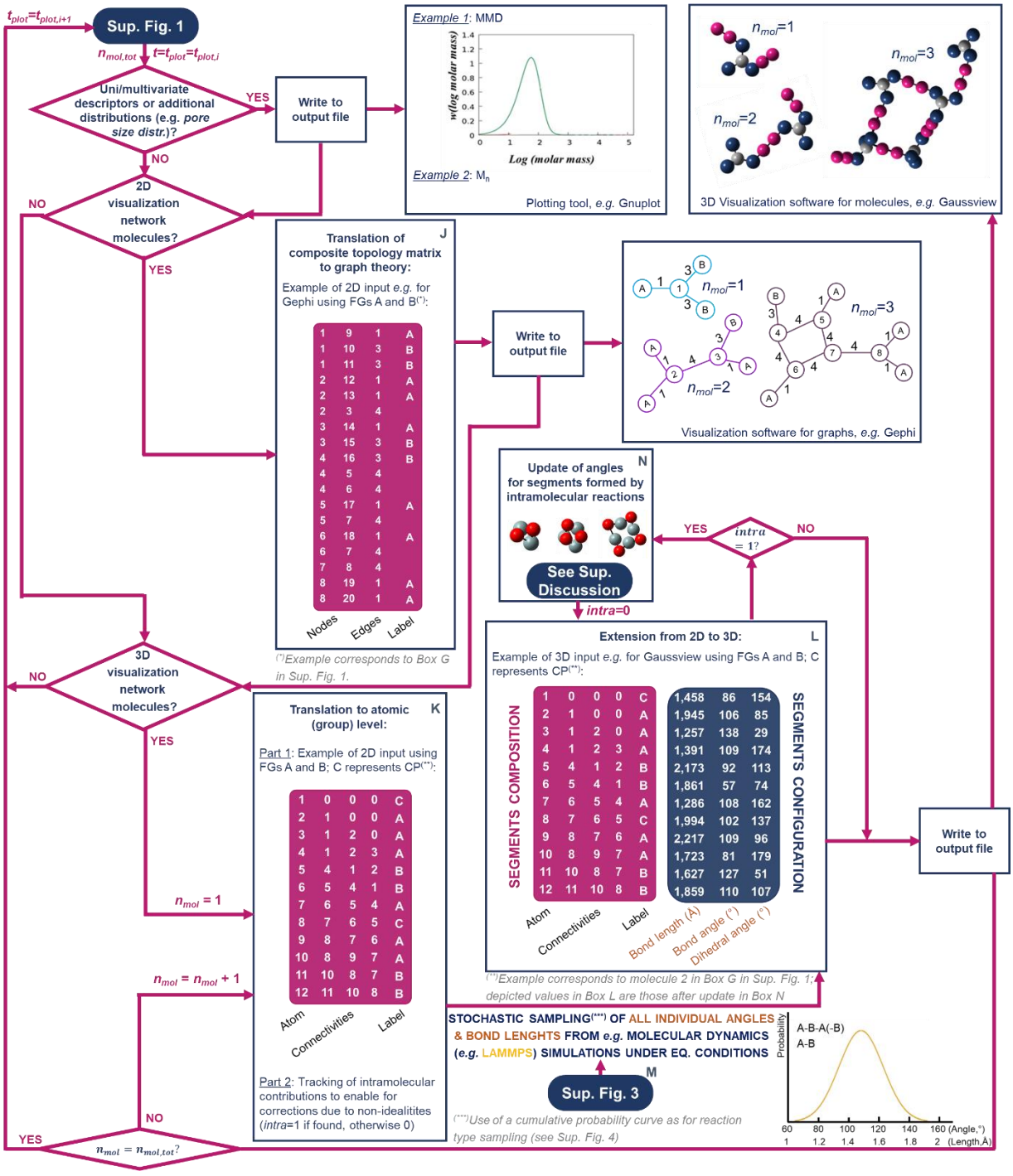

Supplementary Figure 2: Specific part in the flowsheet regarding the kinetic Monte Carlo (*k*MC) simulations (Computational method 1) in which the link is made to plotting univariate characteristics (*e.g.* molar mass distribution; MMD), multivariate characteristics, additional distributions (*e.g.* the molecular pore size distribution; mPSD), and the 2/3D structure of the individual (network) molecules (total number $n_{mol,tot}$) at selected plotting times. For the 3D visualization the link is here made to molecular dynamic (MD) simulations (Computational method 2) for all network molecules, as highlighted in Supplementary Figure 3.[24] For illustration purposes, the 2D and 3D visualization is performed with the same 3 molecules as in box G in Supplementary Figure 1. Example is given in which MD simulation output is generated with Large-scale Atomic/Molecular Massively Parallel Simulator (LAMMPS).

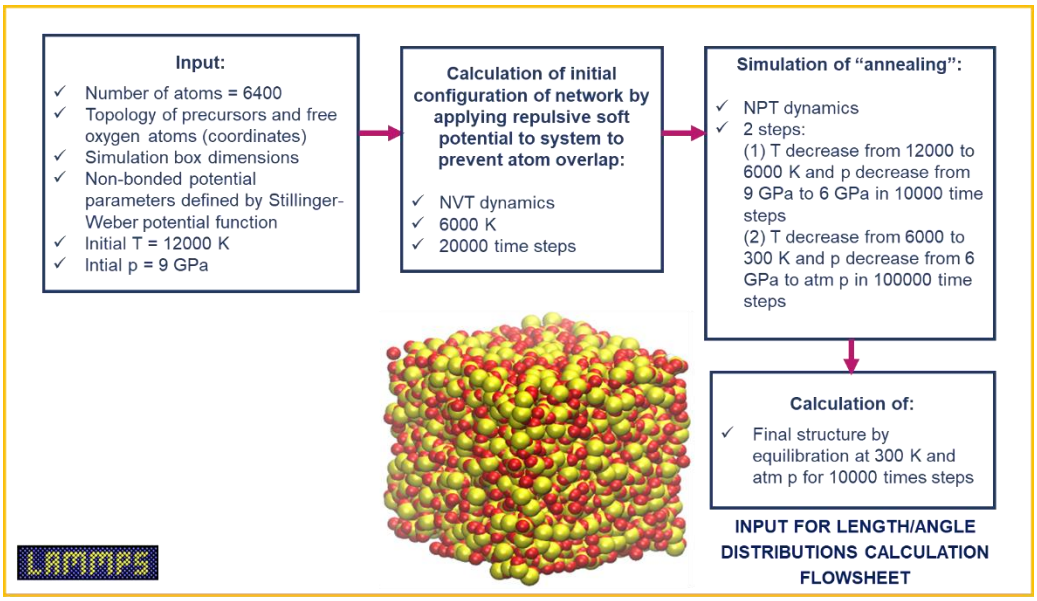

(a)

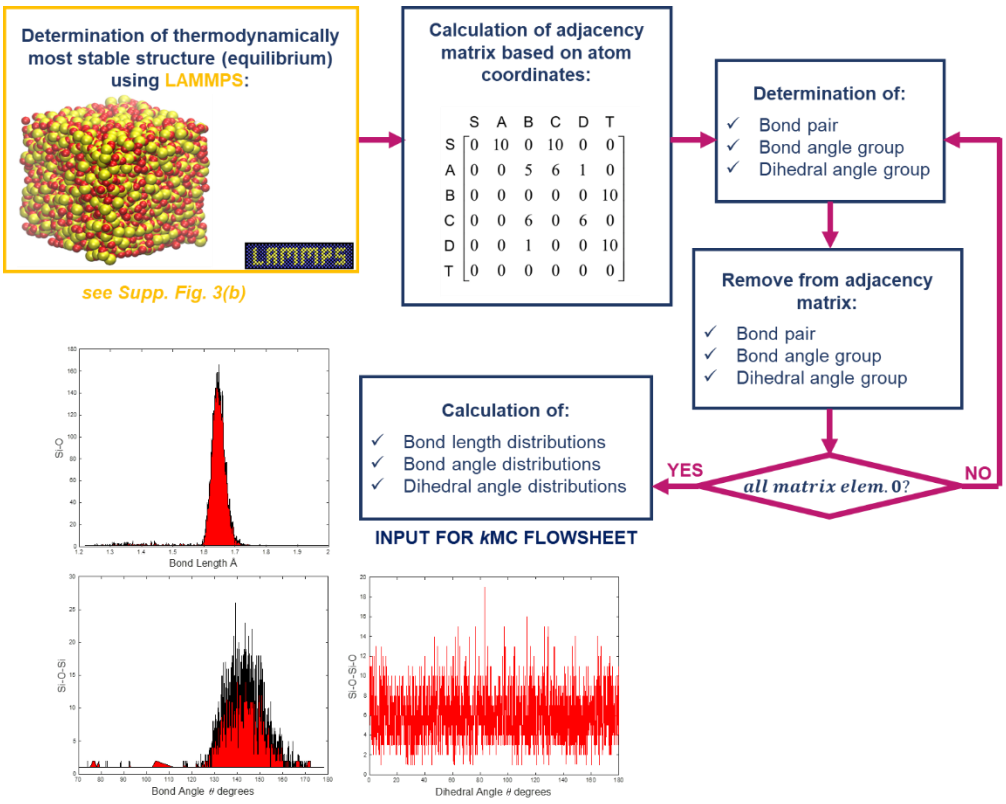

(b)

Supplementary Figure 3: (a) Principles of molecular dynamics simulations via the Large-scale Atomic/Molecular Massively Parallel Simulator (LAMMPS; example of Computational method 2)[24,25] to enable (b) the calculation of thermodynamically feasible bond length, bond angle, and dihedral angle distributions for ideal network elements that are used in Supplementary Figure 2 to visualize at a given plot time the 3D structure of a given network molecule of the kinetic Monte Carlo (*k*MC) simulations.

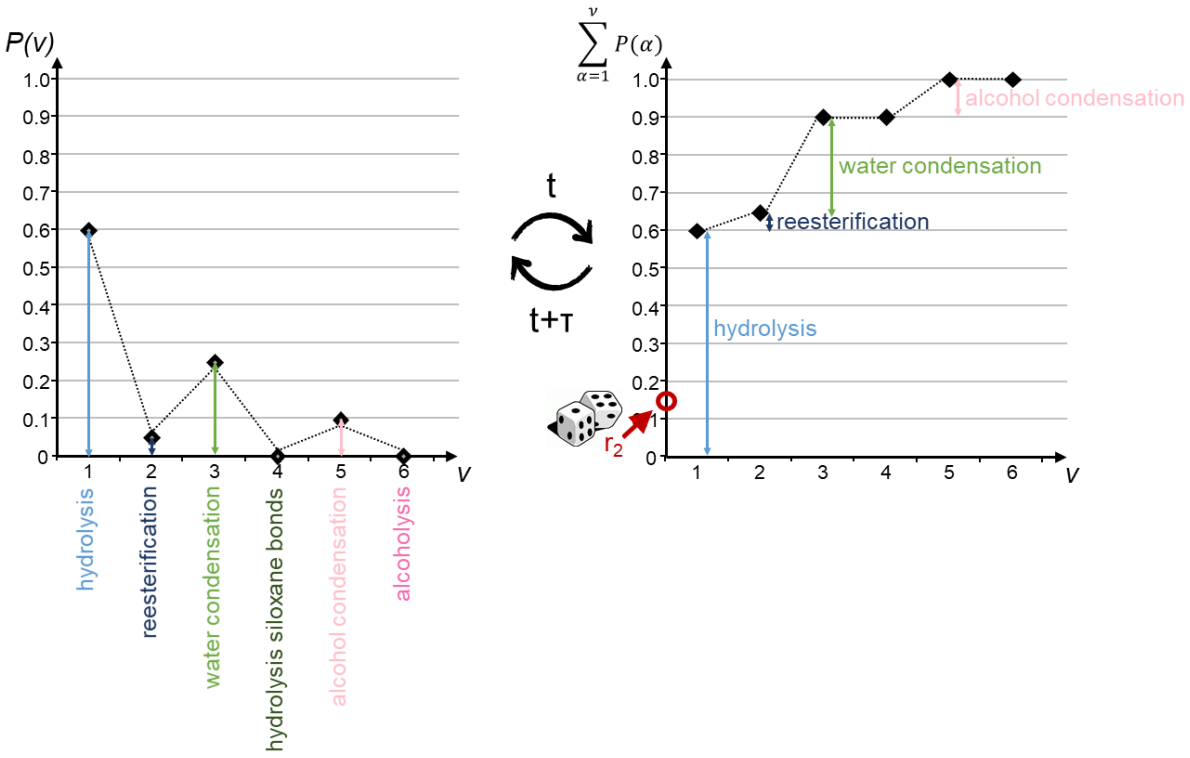

Supplementary Figure 4: Principle of box D in Supplementary Figure 1 focusing on the selection of a reaction type in kinetic Monte Carlo (*k*MC) simulations (here hydrolysis with 5 other reaction types or ν channels possible cf. Supplementary Figure 5) through a random number (r_2; r_2=0.15 in this figure). This is done based on the cumulative distribution at a selected time (right), considering the individual probabilities (left); example for organosilica-based network synthesis with here for simplicity only bimolecular thus intermolecular reactions and no effect of the presence of already reacted groups to not overload the figure. Note that this stochastic sampling approach also works for the selection of bond lengths and angles (cf. box M in Supplementary Figure 2). The *x*-axis is then a discrete listing of the related properties in histogram format.

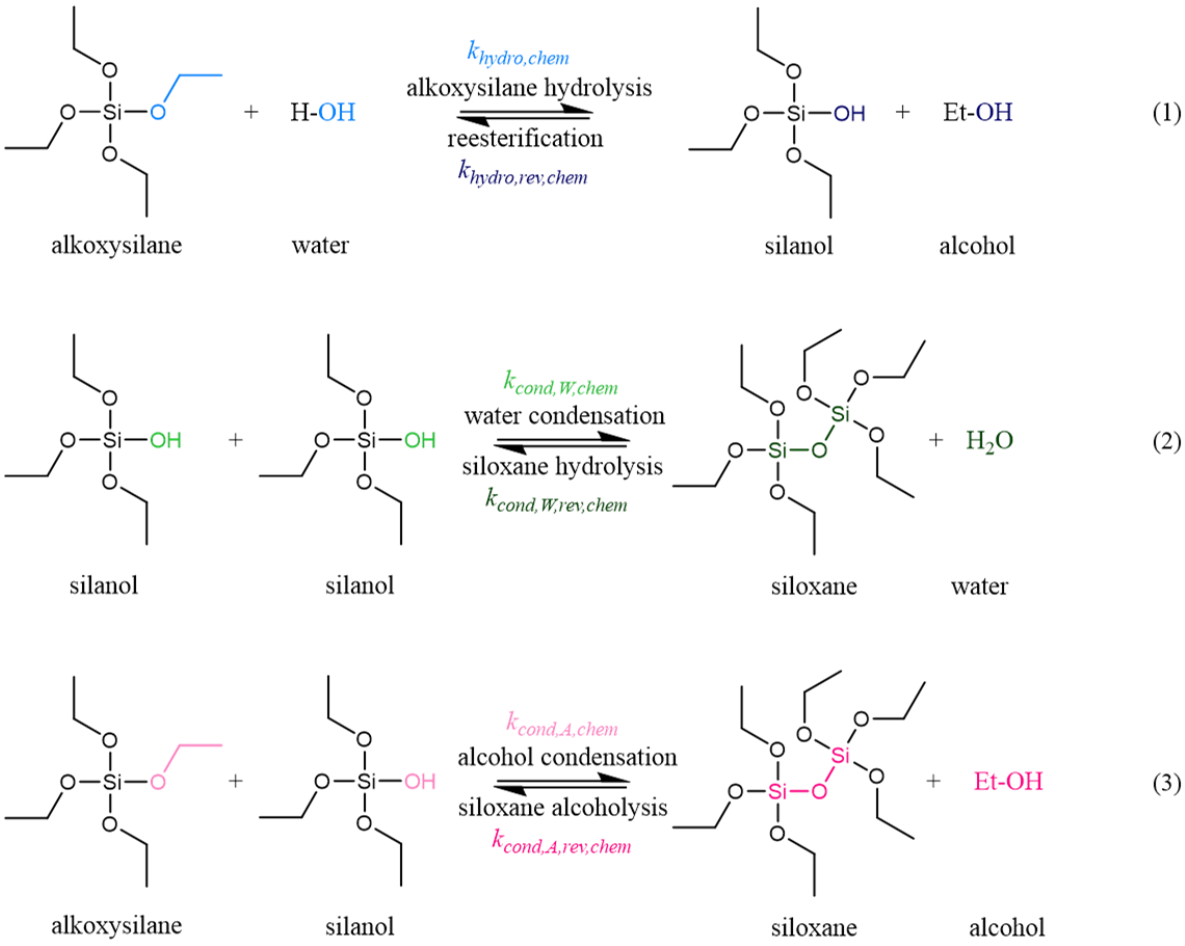

Supplementary Figure 5: General reaction scheme for organosilica-based network case (network chemistry 1 in the main text) as also used for Supplementary Figure 4; the chemical rate coefficients (k_{chem} values) are defined based on the functional groups (FGs) highlighted in a separate color (so-called single-event rate coefficients). For simplicity, only intermolecular reactions are depicted (no explicit mentioning of subscript inter as well). The subscript rev is employed to highlight that we are referring to a reverse reaction. For simplicity, no effect of the presence of already reacted FGs although upon the inspection of actual experimental data it becomes clear that this is needed (cf. the description of the kinetics via Supplementary Figure 8 and 11-12 and Supplementary Table 1, which also covers the intramolecular reactions). This inspection also reveals that the kinetic relevance of the reverse reactions is very low at the selected polymerization temperature of 298 K (for the actual application in the present work only reverse reaction needed for chemical process (1); cf. Supplementary Figure 11d).

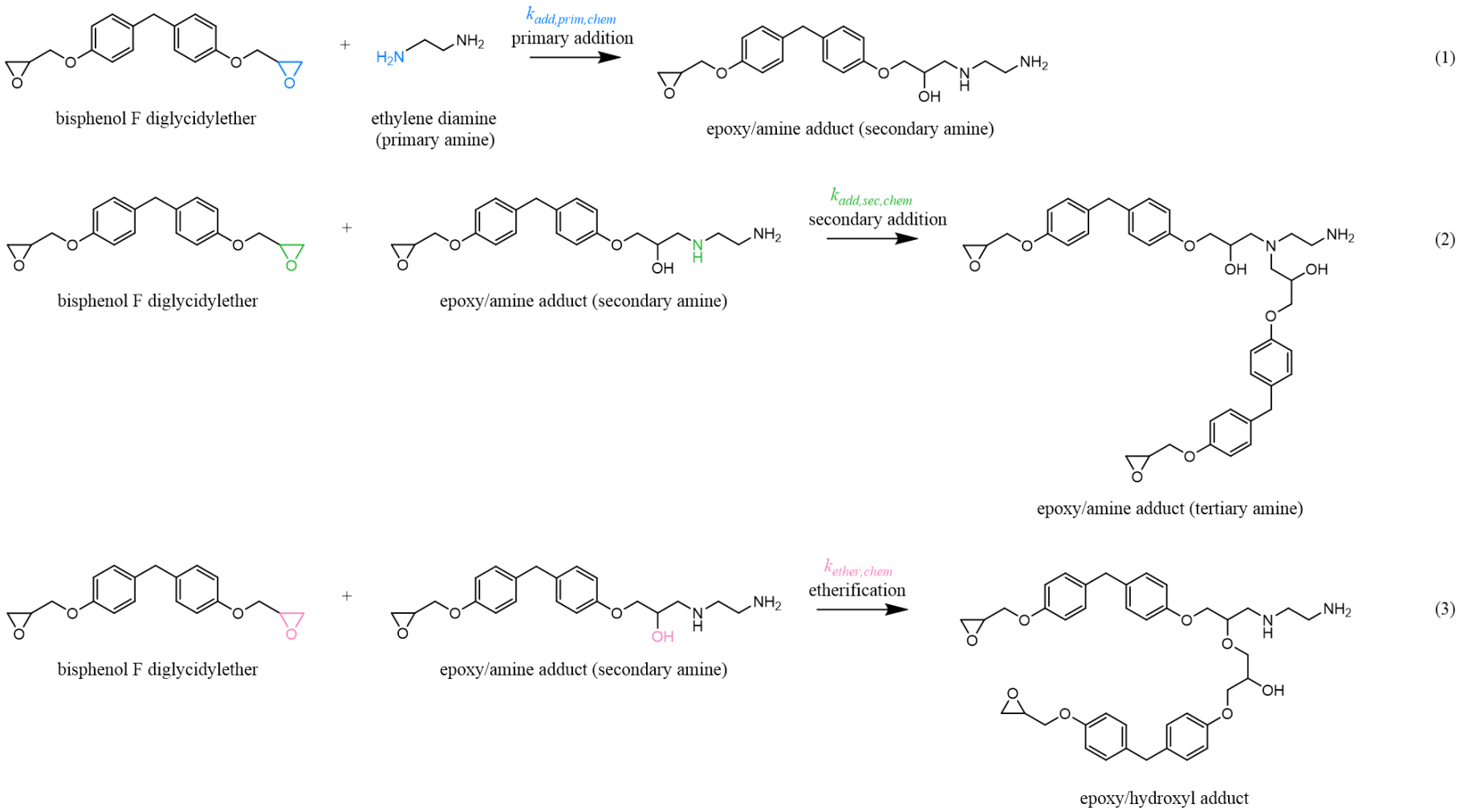

Supplementary Figure 6: General reaction scheme for the epoxy-amine curing case (network chemistry 2 in the main text); the chemical rate coefficients (k_{chem} values) are defined based on the functional groups (FGs) highlighted in a separate color (so-called single-event rate coefficients). For simplicity only intermolecular reactions are depicted and an autocatalytic effect is ignored (no explicit mentioning of subscript inter as well). The latter effect is although relevant upon inspection of experimental data, as demonstrated in Supplementary Figure 13 using the FG definitions in Supplementary Figure 9 and following from the k_{chem} values in Supplementary Table 2, which also covers the intramolecular reactions.

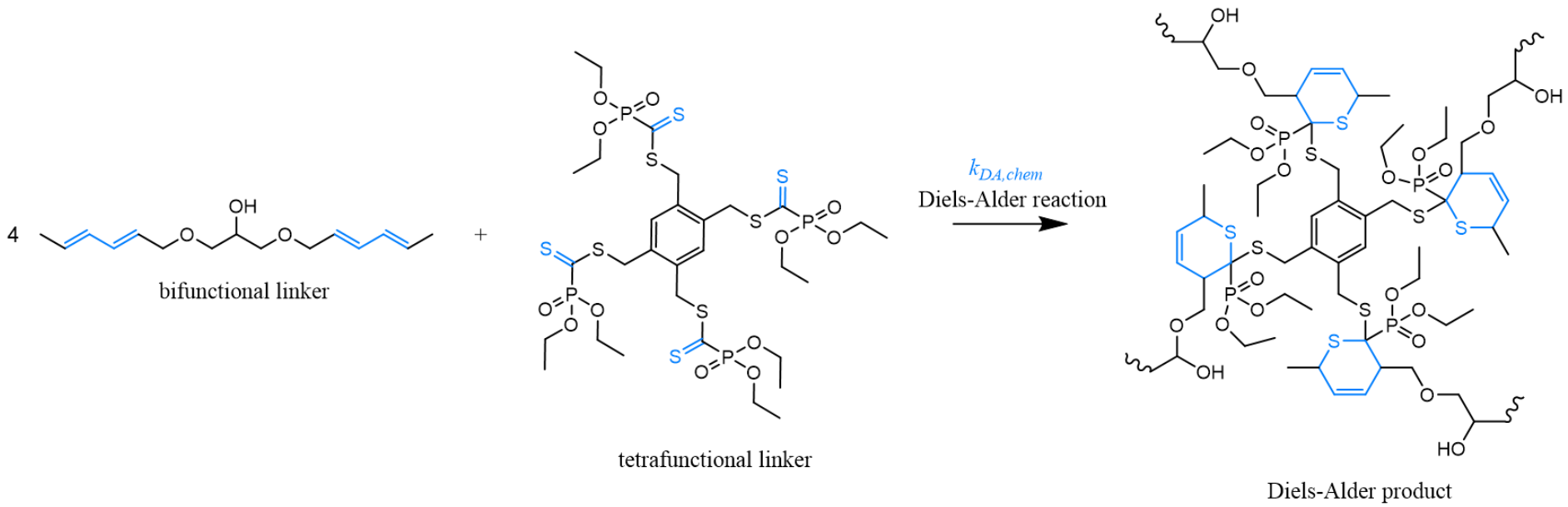

Supplementary Figure 7: General reaction scheme for Diels-Alder based network case (chemistry 3 in the main text); the chemical rate coefficients (k_{chem} values) are defined based on the functional groups (FGs) highlighted in a separate color (so-called single-event rate coefficients). For simplicity only intermolecular reactions are depicted although these are accounted for (see Supplementary Table 3); no explicit mentioning of subscript inter; Supplementary Figure 25 also highlights that the hydroxyl group can be replaced by a drug (there Fmoc is used as drug proxy).

(a) $\mathbf{Q_x(y,z)}$ = Si with

x bridging -O-

y -OH ligands

z – OEt ligands

→ *Information translated into **composition of building blocks (BB) matrix**:*

	x	*y*	*z*	
Si_1	0	0	4	$Q_0(0,4)$
Si_2	1	1	2	$Q_1(1,2)$
Si_3	2	2	0	$Q_2(2,0)$

*Corresponding **structures** for this specific matrix:*

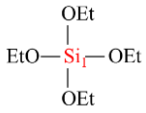

$Q_0(0,4)$

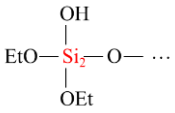

$Q_1(1,2)$

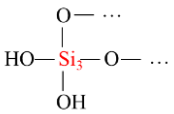

$Q_2(2,0)$

(b) ***Hydrolysis reaction possibilities**:*

$Q_0(0,4) + H_2O \rightarrow Q_0(1,3)$ $\quad f_4 k_{hydro,chem}$

$Q_0(1,3) + H_2O \rightarrow Q_0(2,2)$
$Q_1(0,3) + H_2O \rightarrow Q_1(1,2)$ $\quad f_3 k_{hydro,chem}$

$Q_0(2,2) + H_2O \rightarrow Q_0(3,1)$
$Q_1(1,2) + H_2O \rightarrow Q_1(2,1)$
$Q_2(0,2) + H_2O \rightarrow Q_2(1,1)$ $\quad f_2 k_{hydro,chem}$

$Q_0(3,1) + H_2O \rightarrow Q_0(4,0)$
$Q_1(2,1) + H_2O \rightarrow Q_1(3,0)$
$Q_2(1,1) + H_2O \rightarrow Q_2(2,0)$
$Q_3(0,1) + H_2O \rightarrow Q_3(1,0)$ $\quad f_1 k_{hydro,chem}$

***Condensation reaction possibilities**:*

$Q_w(u,v) + Q_z(x,y) \rightarrow Q_{w+1}(u-1,v) + Q_{z+1}(x-1,y)^{(*)}$ $\quad k_{cond,W,chem}$

$Q_w(u,v) + Q_z(x,y) \rightarrow Q_{w+1}(u,v-1) + Q_{z+1}(x-1,y)^{(*)}$ $\quad k_{cond,A,chem}$

$^{(*)}$ *w,z=0..3; u,v,x,y=0..4*
with w+u+v=4 and z+x+y=4

Supplementary Figure 8: Key input parameters n the matrix-based kinetic Monte Carlo algorithm are chemical rate coefficients (k_{chem} values; box A in Supplementary Figure 1). Here focus is first on the synthesis of the organosilica-based network case at smaller times at which only intermolecular chemical effects matter (chemistry 1 in the main text; no explicit mentioning of subscript inter). Preliminary research showed that we need to modify the general reaction scheme as depicted in Figure 5 to grasp the low time experimental kinetic data as included in Supplementary Figure 11a-c (symbols). Specifically we need to account for 4 hydrolysis reactivities instead of a lumped one (see Supplementary Figure 11d; relative comparison via the factors $f_{1\text{-}4}$ with f_4=1) and we can neglect the reverse reactions. Condensation reactivities can remain lumped. One reverse reaction (reesterification) is although needed if we also include intermediate times (Supplementary Figure 12b). To facilitate parameter determination a simplified kinetic Monte Carlo tool can be used. The principles are: (a) the use of an extra composition of building blocks (BB) matrix to track the species types (rows). This matrix covers the number of -O- bridges/crosslinks (first column; also subscript for associated Q notation), the number of OEt groups (second column; first index of Q), and the number OH groups (third column; second index of Q); (b) 6 reaction types of which 5 lumped are written down based on the Q species introduced in (a).

(a) $\mathbf{Q_x(y)}$ = $N(CH_2)_2N$ with | *x* epoxide additions
y -H ligands

*Examples of related **structures**:*

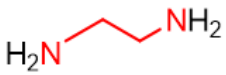

$Q_0(4)$

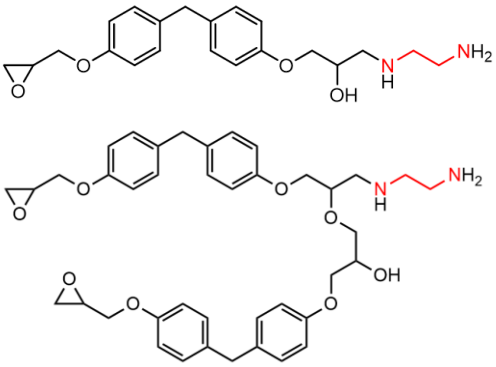

$Q_1(3)$

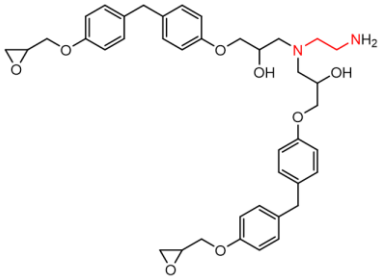

$Q_2(2)$

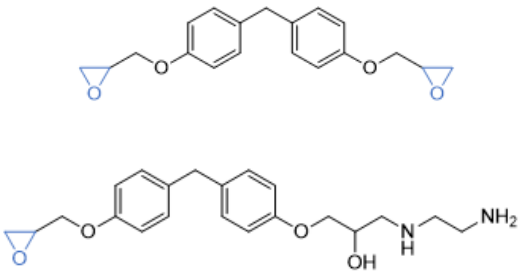

-epoxide

(b) ***Addition reaction possibilities**:*

$$Q_0(4) + (-\text{epoxide}) \rightarrow Q_1(3) + (-OH) \qquad f_4 k_{add,prim,chem}$$

$$Q_1(3) + (-\text{epoxide}) \rightarrow Q_2(2) + (-OH) \qquad k_{add,sec} = f_3 k_{add,prim,chem}$$

$$Q_2(2) + (-\text{epoxide}) \rightarrow Q_3(1) + (-OH) \qquad f_2 k_{add,prim,chem}$$

$$Q_3(1) + (-\text{epoxide}) \rightarrow Q_4(0) + (-OH) \qquad k_{add,sec} = f_1 k_{add,prim,chem}$$

***Etherification reaction possibility**:*

$$-OH + (-\text{epoxide}) \rightarrow -OH \qquad k_{ether,chem}$$

Supplementary Figure 9: Key input parameters in the matrix-based kinetic Monte Carlo algorithm are chemical rate coefficients (k_{chem} values; box A in Supplementary Figure 1). Here focus is on the small-time epoxy-curing network case (chemistry 2 in the main text with only the need to cover intermolecular chemical effects (no explicit mentioning of subscript inter). To facilitate the parameter determination a simplified kinetic Monte Carlo tool can be used similar to Supplementary Figure 8, with now 3 overall reaction types and focusing on the diamine. Model validation is performed to the low time experimental data in Supplementary Figure 13a. To enable relative comparison the factors $f_{1\text{-}4}$ are introduced in analogy with Supplementary Figure 8. Here we have $f_2 = f_4$ and $f_1 = f_3$.

(a) **$Q_x(y)$** = tetrafunctional linker with | *x* Diels-alder linkages
y original ligands

*Examples of related **structures**:*

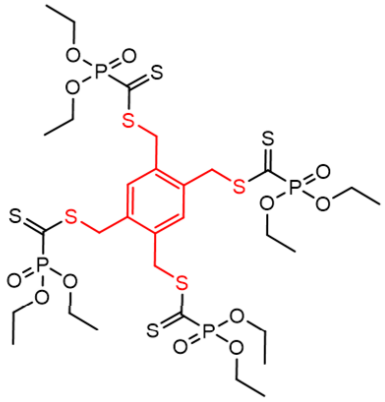

$Q_0(4)$

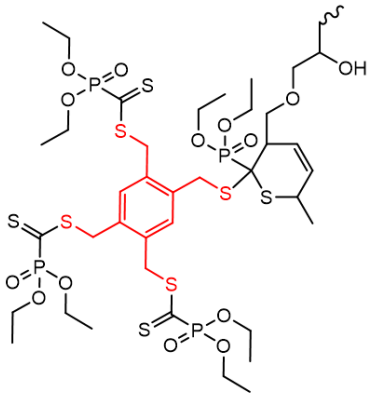

$Q_1(3)$

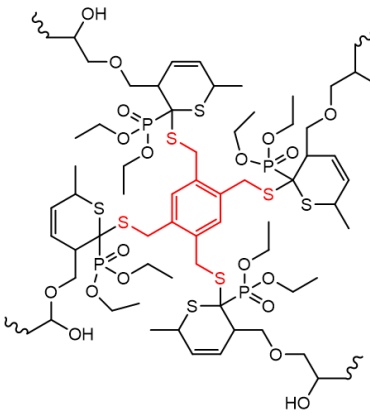

$Q_4(0)$

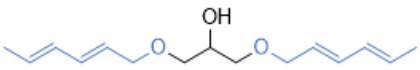

-hexa-2,4-dienoyl

(b) ***Diels-Alder reaction possibilities**:*

$$Q_0(4) + (-\text{hexa-2,4-dienyol}) \rightarrow Q_1(3) \qquad f_4 k_{DA,chem}$$

$$Q_1(3) + (-\text{hexa-2,4-dienyol}) \rightarrow Q_2(2) \qquad f_3 k_{DA,chem}$$

$$Q_2(2) + (-\text{hexa-2,4-dienyol}) \rightarrow Q_3(1) \qquad f_2 k_{DA,chem}$$

$$Q_3(1) + (-\text{hexa-2,4-dienyol}) \rightarrow Q_4(0) \qquad f_1 k_{DA,chem}$$

Supplementary Figure 10: Key input parameters in the matrix-based kinetic Monte Carlo algorithm are the chemical rate coefficients (k_{chem} values; box A in Supplementary Figure 1). Here we focus on the intermolecular k_{chem} values; no explicit mentioning of subscript inter; in contrast to the other 2 chemistries we can use first data of a monofunctional system (Supplementary Figure 14) to determine $k_{DA,chem}$. To enable relative comparison the factors $f_{1\text{-}4}$ can be introduced (with f_1=1). The current work although uses for all factors a value of 1. To facilitate the parameter determination a simplified kinetic Monte Carlo mathematical tool can again be used as for Supplementary Figure 8 and 9. We now put the tetrafunctional system central in the counting.

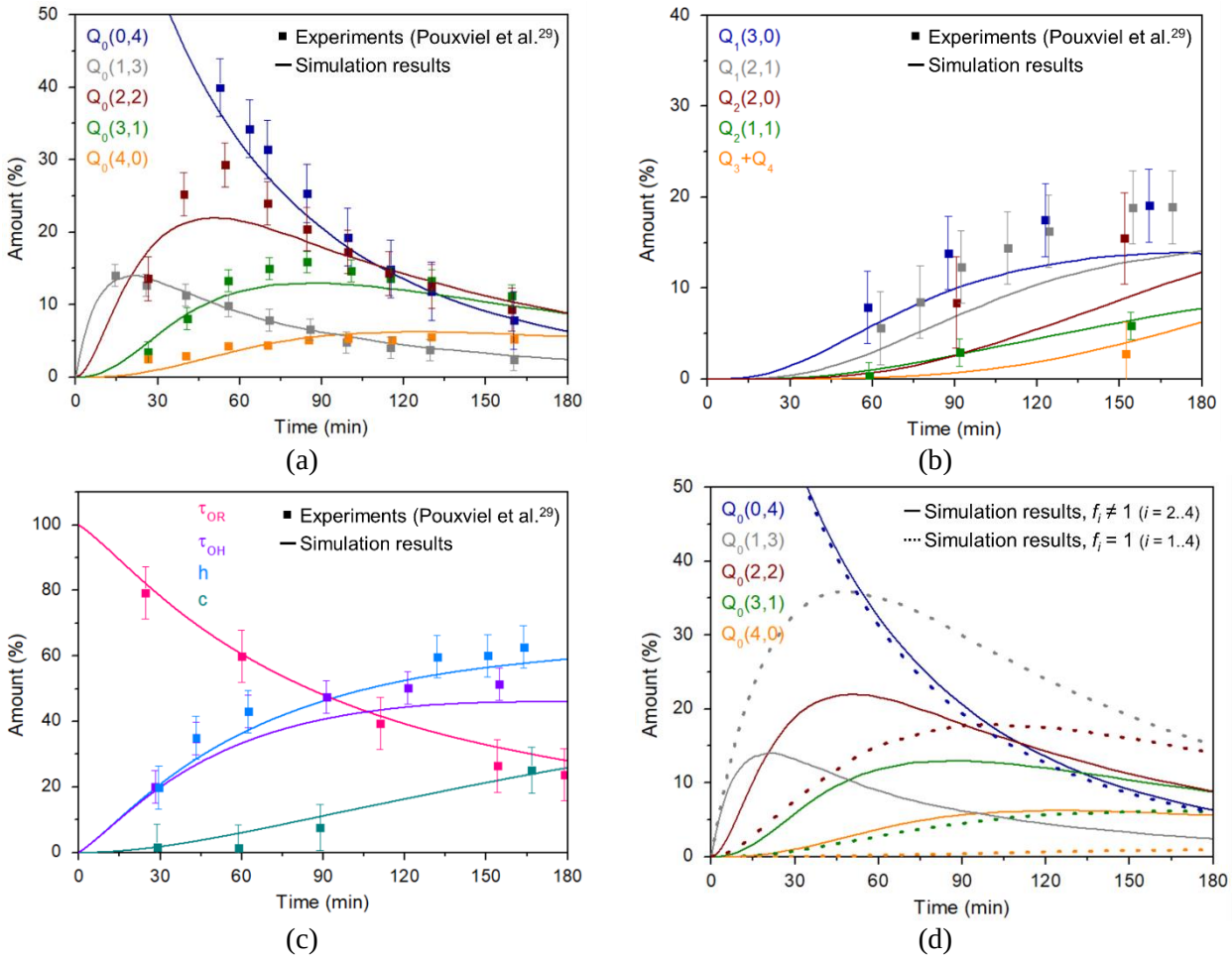

Supplementary Figure 11: For the organosilica case (network chemistry 1 in the main text; initial conditions in Supplementary Table 1; 298 K), the comparison of small time experimental data (taken from literature[29] based on ^{29}Si nuclear magnetic resonance (NMR) peak data) and kinetic Monte Carlo data (present work; parameters in Supplementary Table 1) regarding the variation of the (a) the relative amount of silanol species, (b) the relative amount of condensed species, (c) the hydrolysis ratio *h* and the condensation ratio *c*, the % of Si-OR remaining groups τ_{OR}, and the % of Si-OH remaining groups τ_{OH} (Supplementary equation (1)-(4)). The small-time data (up to 3 hours; 180 minutes) are used to determine the 6 forward intermolecular chemical rate coefficients based on the Q species types in Supplementary Figure 8; average error bars based on standard deviation. Additionally in (d) the comparison of simulation results in case no differentiation is made for the hydrolysis step for the *f* values (so same hydrolysis rate coefficients; dashed lines) with the simulations results in case a differentiation is made (full lines; from a) is given. It follows that such *f* values are needed. It should be noted that the model is inherent consistent and overall the description of the literature experimental data is acceptable and the data in b) are more prone to experimental error (also clear from the error bars).

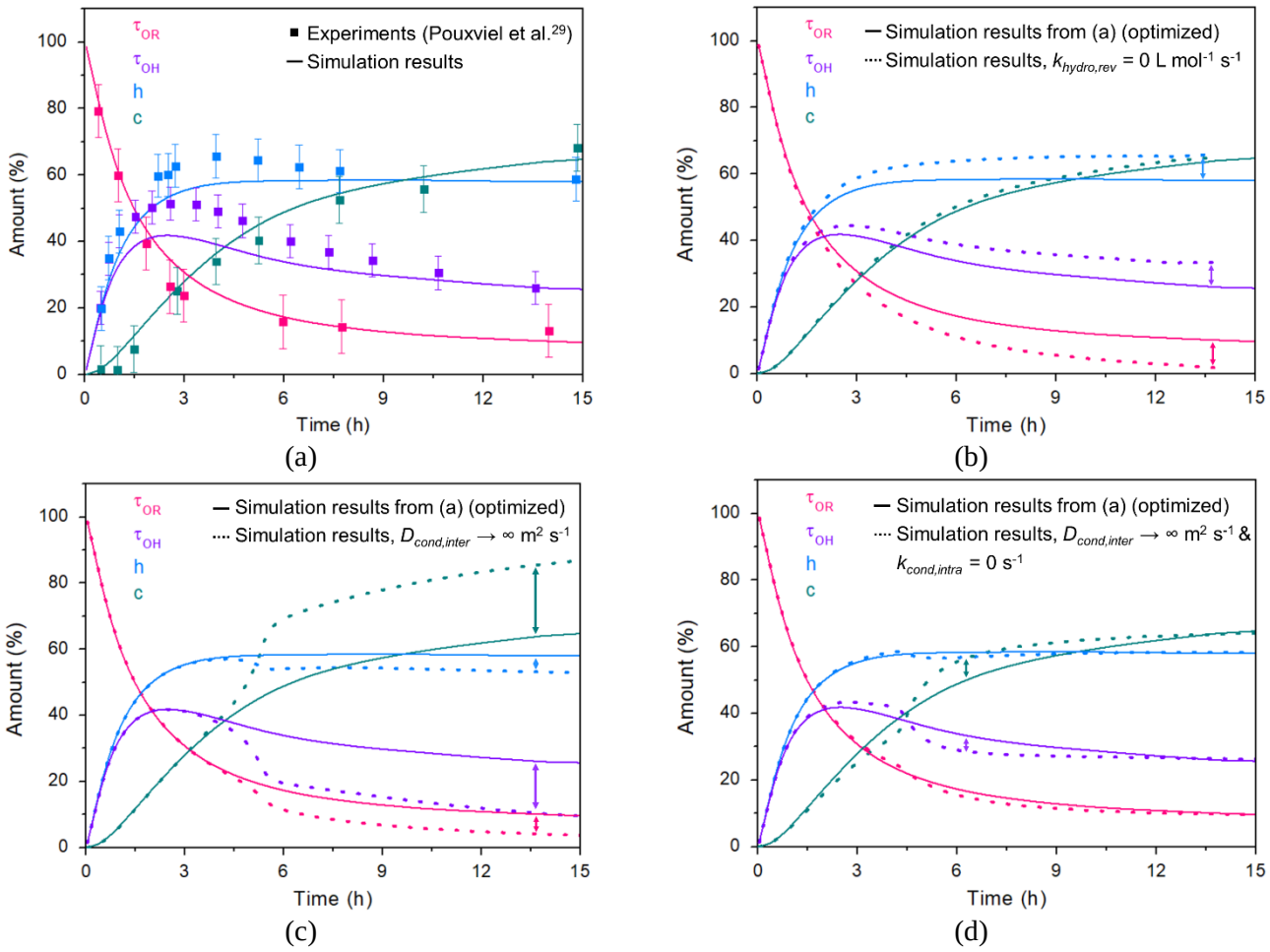

Supplementary Figure 12: (a) For the organosilica case (network chemistry 1 in the main text; initial conditions in Supplementary Table 1; 298 K), the comparison of longer time experimental data (taken from literature[29] based on ^{29}Si nuclear magnetic resonance (NMR) peak data) and kinetic Monte Carlo data (present work) for the variation of the hydrolysis ratio *h*, the condensation ratio *c*, the % of Si-OR remaining groups τ_{OR}, and the % of Si-OH remaining groups τ_{OH} is shown (Supplementary equation (1)-(4)); average error bars based on standard deviation. The extra large-time data in (a) compared to Supplementary Figure 11(a) are used to tune the reverse hydrolysis chemical rate coefficient (the last and 7th intermolecular chemical rate coefficient), to quantify to importance of diffusional limitations on intermolecular reactions and to highlight the relevance of the intramolecular condensation rate. These three aspects are further highlighted in the other subplots with in (b) the comparison of simulation results in case no reverse hydrolysis reactions take place (dashed lines; too fast kinetics; no plateaus) with the optimized simulation results from (a) (full lines); in (c) the comparison of the simulation results in case no diffusional limitations on intermolecular reactions are taken into account (dashed lines; too fast network formation) with the optimized simulation results from (a) (full lines); and in (d) the comparison of simulation results in case no intramolecular condensation reactions and no diffusional limitations on intermolecular reactions take place (dashed lines; less gradual variations) with the optimized simulation results from (a) (full lines) are shown. Arrows are added in subplots (b)-(d) to show the mismatches between full and dashed lines.

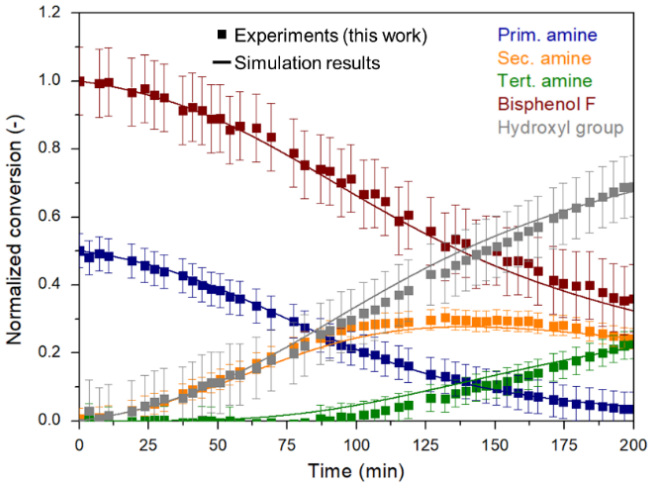

(a)

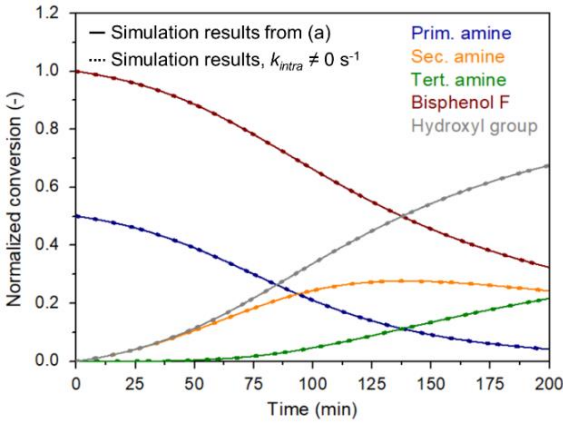

(b)

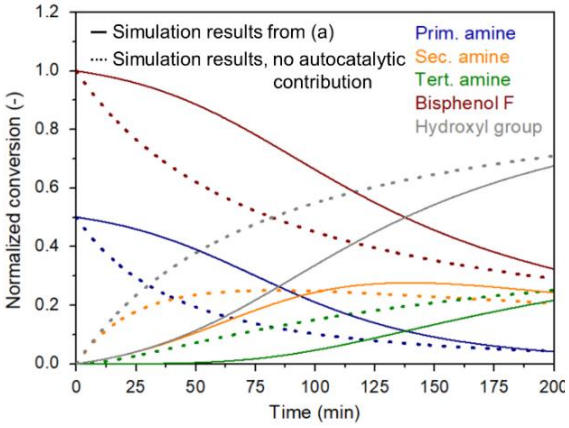

(c)

Supplementary Figure 13: (a) Determination of the 3 intermolecular chemical rate coefficients for the epoxy-amine curing case (chemistry 2 in the main text; cf. Supplementary Figure 9; parameters in Supplementary Table 2; 298 K). Both experimental and kinetic Monte Carlo data generated in the present work; average error bars based on standard deviation. (b) Comparison of simulations in (a) (full lines) with the additional consideration of intramolecular reactions (dashed lines). Due to the low times the effect is negligible. (c) Demonstration that autocatalytic contributions matter. Full lines from (a) are compared with the case without such reactions but aiming at similar rates (dashed lines; k_{PA} = 6.0 10^{-5} L mol^{-1} s^{-1}; k_{SA} = 3.0 10^{-5} L mol^{-1} s^{-1} ; k_{ether} = 0 L mol^{-1} s^{-1}). The dashed lines in subplot (c) have the incorrect shape in all cases.

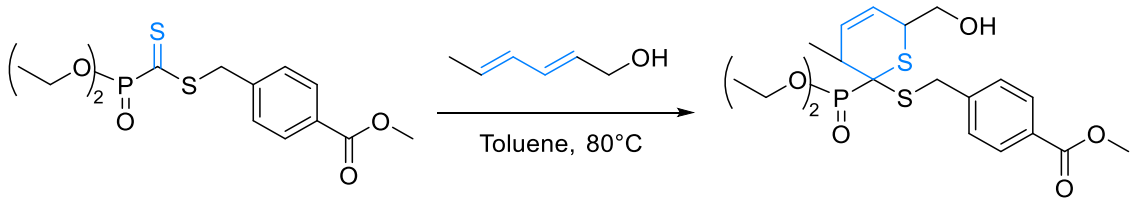

(a)

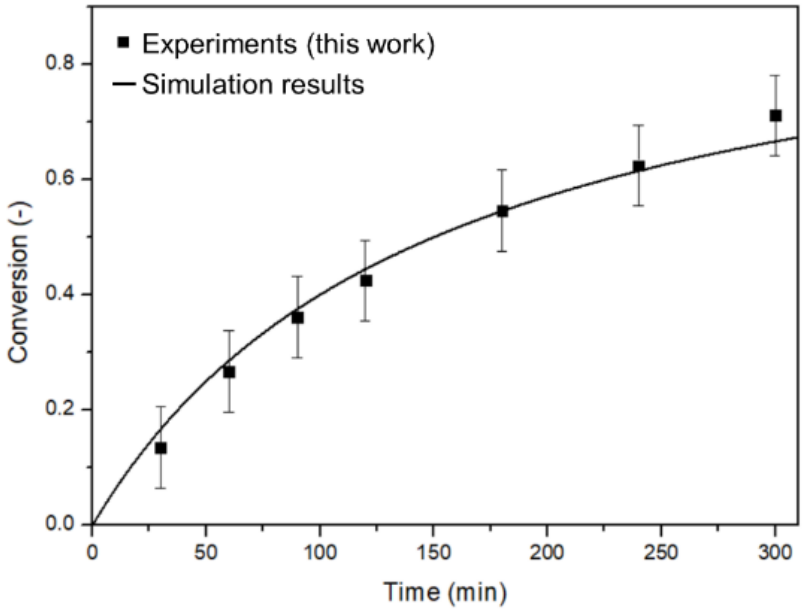

(b)

Supplementary Figure 14: Determination of the intermolecular chemical rate coefficient for the Diels-Alder network formation case (chemistry 3 in main text; cf. Supplementary Figure 10; parameters in Supplementary Table 2; 353 K). Both experimental and kinetic Monte Carlo data generated in the present work; (a) small molecule system used for parameter determination and (b) comparison of experimental and simulated data for this small molecule system.

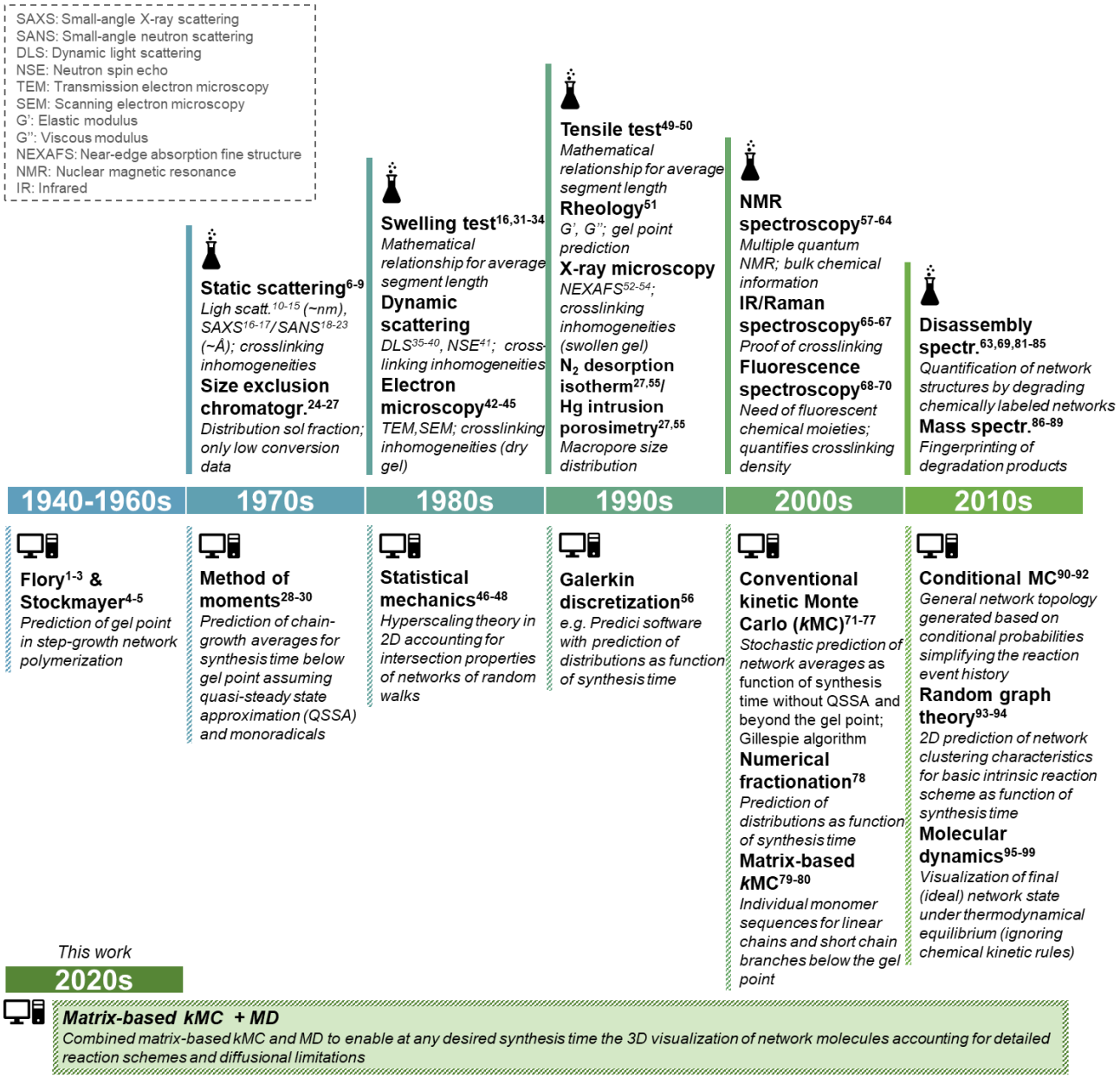

Supplementary Figure 15: State-of-the-art regarding experimental and theoretical characterization methodologies of polymer networks. Experimental contributions (first row) are often at scales larger than the molecular scale; theoretical contributions (second row) come from the field of chemical kinetics or physics. The ultimate goal, as covered in the present work (third row) by combining matrix-based kinetic Monte Carlo (*k*MC) and molecular dynamics (MD) simulations, is to visualize the synthesis time dependency of the incorporation of each building block/molecule/functionality; a list of references per characterization methodology is given on the next page.

Additional information for the reading of Supplementary Figure 15:

[1] PJ Flory, J. Am. Chem. Soc. 63 (11), 3083 (1941).
[2] PJ Flory, J. Phys. Chem. 46 (1), 132 (1942).
[3] PJ Flory, Chem. Rev. 39 (1), 137 (1946).
[4] WH Stockmayer, J. Chem. Phys. 11 (2), 45 (1943).
[5] WH Stockmayer, J. Chem. Phys. 12 (4), 125 (1944).
[6] K Dusek, in Polymer Networks, Structures and Mechanical Properties (1971), pp. 245.
[7] AM Hecht et al., Macromolecules 18 (11), 2167 (1985).
[8] SJ Canda et al., MRS Proceedings 177, 3 (1989).
[9] E Geissler et al., Macromol. Symp. 227, 27 (2005).
[10] T Tanaka et al., J. Chem. Phys. 59 (9), 5151 (1973).
[11] JP Munch et al., J. Polym. Sci.: Polym. Phys. Ed. 14 (6), 1097 (1976).
[12] M Shibayama et al., J. Chem. Phys. 107 (13), 5227 (1997).
[13] B Lindemann et al., Macromolecules 30 (14), 4073 (1997).
[14] MY Kizilay and O Okay, Macromolecules 36 (18), 6856 (2003).
[15] J Nie et al., Macromolecules 37 (17), 6558 (2004).
[16] S Mallam et al., Macromolecules 22 (8), 3356 (1989).
[17] GR Deen et al., Phys. Chem. Chem. Phys. 13 (8), 3108 (2011).
[18] J Bastide and L Leibler, Macromolecules 21 (8), 2647 (1988).
[19] F Ikkai et al., Macromolecules 31 (10), 3275 (1998).
[20] T Norisuye et al., Polymer 43 (19), 5289 (2002).
[21] M Stieger et al., J. Chem. Phys. 120 (13), 6197 (2004).
[22] E Mendes et al., Europhys. Lett. 32, 273 (2007).
[23] M Shibayama, Polym. J. 43 (1), 18 (2011).
[24] S Kuga, J. Chromatogr. A 206 (3), 449 (1981).
[25] T Crispin and I Halász, J. Chromatogr. A 239, 351 (1982).
[26] QC Wang et al., J. Polym. Sci. Pol. Chem. 32 (13), 2577 (1994).
[27] O Okay, Prog. Polym. Sci. 25 (6), 711 (2000).
[28] H Tobita and AE Hamielec, Makromol. Chem-M. Symp. 20-21 (1), 501 (1988).
[29] E Vivaldo-Lima et al., Polym. React. Eng. 2 (1-2), 87 (1994).
[30] P López-Domínguez et al., Macromol. Theor. Simul. 27 (1), 1700064 (2017).
[31] T Norisuye et al., Macromolecules 36 (16), 6202 (2003).
[32] N Gundogan et al., Macromol. Chem. Phys. 205 (6), 814 (2004).
[33] HML Thijs et al., J. Mater. Chem. 17 (46), 4864 (2007).
[34] W Chassé et al., Soft Matter 9 (29), 6943 (2013).
[35] JGH Joosten et al., Macromolecules 24 (25), 6690 (1991).
[36] H Oikawa and K Murakami, Macromolecules 24 (5), 1117 (1991).
[37] E Geissler, in Dynamic Light Scattering, edited by W. Brown (1993), pp. 471.
[38] M Shibayama et al., Macromolecules 29 (20), 6535 (1996).
[39] Y Rabin and S Panyukov, Macromolecules 30 (2), 301 (1997).
[40] S Mitsuhiro, B. Chem. Soc. Jpn. 79 (12), 1799 (2006).
[41] S Koizumi et al., J. Chem. Phys. 121 (24), 12721 (2004).
[42] T-P Hsu and C Cohen, Polymer 25 (10), 1419 (1984).
[43] IM Huxham et al., Polymer 33 (13), 2768 (1992).
[44] J Shan et al., Polym. J. 28 (10), 886 (1996).
[45] G Patras et al., Macromolecules 34 (18), 6396 (2001).
[46] B Duplantier, Phys. Rev. Lett. 57 (8), 941 (1986).
[47] B Duplantier et al., Phys. Rev. Lett. 57 (25), 3179 (1986).
[48] B Duplantier, J. Stat. Phys. 54 (3), 581 (1989).
[49] MS Eroğlu, J. Appl. Polym. Sci. 70 (6), 1129 (1998).
[50] T Yang et al., J. Polym. Sci. Polym. Chem. 49 (18), 4044 (2011).
[51] GM Kavanagh and SB Ross-Murphy, Prog. Polym. Sci. 23 (3), 533 (1998).
[52] H Ade et al., Polymer 36 (9), 1843 (1995).
[53] GE Mitchell et al., Macromolecules 35 (4), 1336 (2002).
[54] B Watts and H Ade, Mater. Today 15 (4), 148 (2012).
[55] SJ Gregg and KSW Sing, Adsorption, surface area, and porosity, 2nd ed. (1995).
[56] AM Fuxman et al., Macromol. Theor. Simul. 12 (9), 647 (2003).
[57] K Saalwächter, J. Am. Chem. Soc. 125 (48), 14684 (2003).
[58] K Saalwächter, Prog. Nucl. Mag. Res. Sp. 51 (1), 1 (2007).
[59] JL Valentín et al., Macromolecules 43 (9), 4210 (2010).
[60] F Lange et al., Macromolecules 44 (24), 9666 (2011).
[61] W Chassé et al., Macromolecules 45 (2), 899 (2012).
[62] K Saalwächter et al., Soft Matter 9 (29), 6587 (2013).
[63] J Höpfner et al., Macromolecules 47, 4251 (2014).
[64] Y Gu et al., Trends in Chemistry 1 (3), 318 (2019).
[65] P Musto et al., Polymer 48 (13), 3703 (2007).
[66] F Cavalli et al., Polym. Chem. 8 (25), 3778 (2017).
[67] R Guterman et al., Polym. Chem. 8 (22), 3425 (2017).
[68] H Aoki et al., Macromolecules 33 (26), 9650 (2000).
[69] FB Madsen et al., RSC Adv. 4 (14), 6939 (2014).
[70] D Estupiñán et al., Angew. Chem. Int. Edit. 57 (20), 5925 (2018).
[71] J Šomvársky and K Dusek, Polym. Bull. 33, 369 (1994).
[72] N Gilra et al., J. Chem. Phys. 112 (15), 6910 (2000).
[73] M Wen et al., Macromolecules 36 (11), 4151 (2003).
[74] AG Balabanyan et al., Polymer 46 (12), 4248 (2005).
[75] S Hamzehlou et al., Macromolecules 46 (22), 9064 (2013).
[76] AK Tripathi et al., Macromolecules 48 (1), 184 (2015).
[77] AK Tripathi et al., Polymer 96, 130 (2016).
[78] S Kizilel et al., Macromol. React. Eng. 1 (6), 587 (2007).
[79] PHM Van Steenberge et al., Macromolecules 45 (21), 8519 (2012).
[80] DR D'hooge et al., Polym. Chem. 6 (40), 7081 (2015).
[81] H Zhou et al., P. Natl. A. Sci. 109 (47), 19119 (2012).
[82] H Zhou et al., J. Am. Chem. Soc. 136 (26), 9464 (2014).
[83] K Kawamoto et al., Macromolecules 48 (24), 8980 (2015).
[84] J Wang et al., ACS Macro Lett. 7 (2), 244 (2018).
[85] X Xu et al., Polym. Chem. 10 (35), 4837 (2019).
[86] AK Burkoth and KS Anseth, Macromolecules 32 (5), 1438 (1999).
[87] A Höglund et al., J. Polym. Sci. Pol. Chem. 46 (13), 4617 (2008).
[88] SE Whitson et al., Anal. Chem. 80 (20), 7778 (2008).
[89] V Mass et al., Macromol. Chem. Phys. 210 (22), 1957 (2009).
[90] I Kryven et al., Macromol. React. Eng. 7 (5), 205 (2013).
[91] YR Zhao et al., Macromol. Theor. Simul. 23 (6), 383 (2014).
[92] K Dusek et al., Macromol. React. Eng. 6 (11), 426 (2012).
[93] I Kryven et al., Macromol. Theor. Simul. 25 (5), 449 (2016).
[94] V Schamboeck et al., Macromol. Theor. Simul. 26 (6), 1700047 (2017).
[95] J Chua and Q Tu, Polymers 10 (1), 64 (2018).
[96] M Huang and C Abrams, Macromol. Theor. Simul. 28 (6), 1900030 (2019).
[97] VY Rudyak et al., Sci. Rep. 9 (1), 13052 (2019).
[98] FK Schwab and C Denniston, Polym. Chem. 10 (32), 4413 (2019).
[99] GG Vogiatzis et al., Macromol. Theor. Simul. 28 (6), 1900036 (2019).

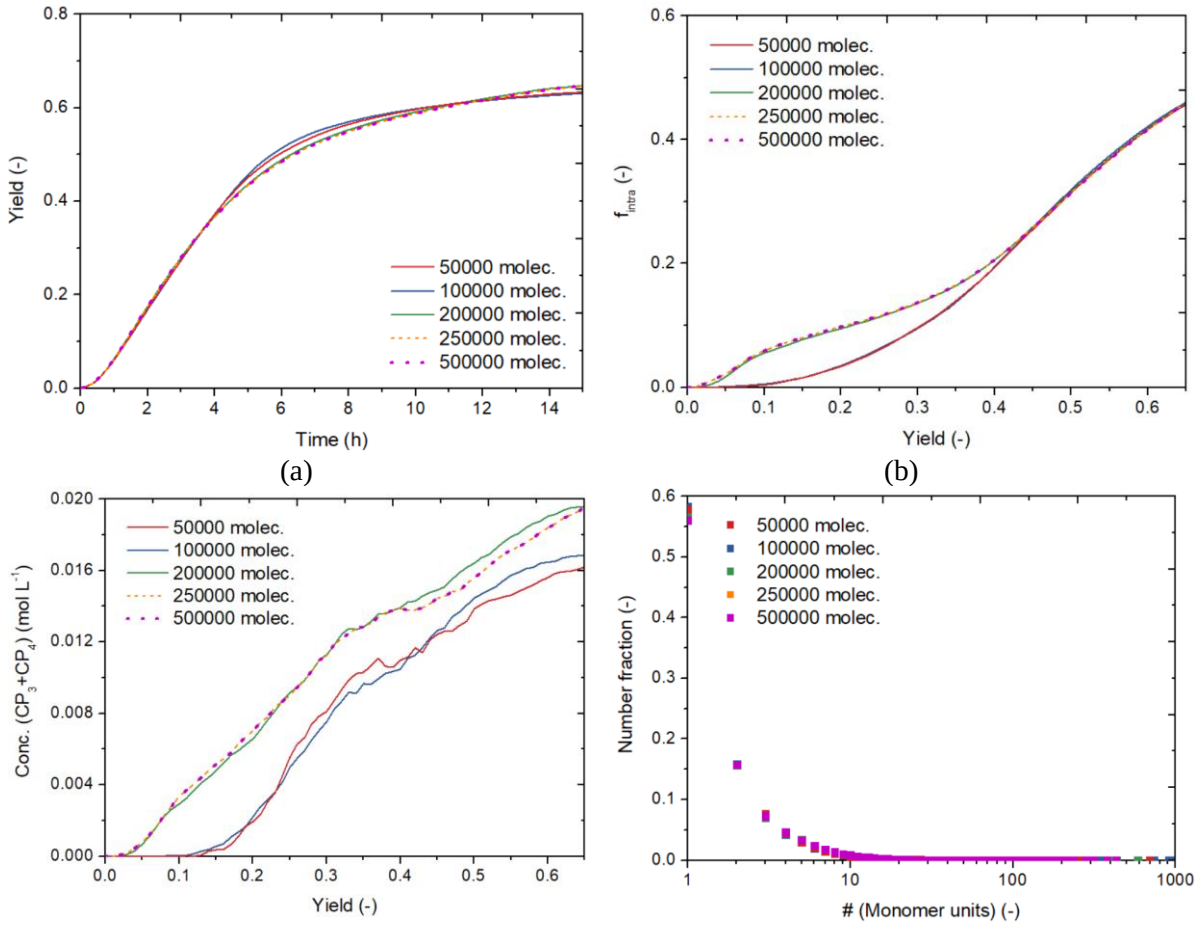

Supplementary Figure 16: Check on numerical convergence of the kinetic Monte Carlo (*k*MC) simulations. By sufficiently increasing the initial total number of molecules $n_{tot,0}$ we are able to obtain representative numerical simulation results reflecting the reaction probabilities. Examples given for network chemistry 1 (initial conditions and parameters in Supplementary Table 1): (a) Yield as function of synthesis time, (b) Fraction of intramolecular reactions as function of yield, (c) Concentration of molecules with at least 3 crosslinking points thus crosslinked 3 or 4 times (CP_3+CP_4) as function of yield and (d) number chain length distribution for yield of 0.6; simulation results for $n_{tot,0}$ = 50000 (red), $n_{tot,0}$ = 100000 (blue), $n_{tot,0}$ = 200000 (green), $n_{tot,0}$ = 250000 (orange), and $n_{tot,0}$ = 500000 (purple); It follows that at least 200000 initial TEOS molecules are necessary to obtain acceptable numerical convergence and thus appropriate *k*MC simulation results. A recommended value for excellent convergence for all characteristics is 250000.

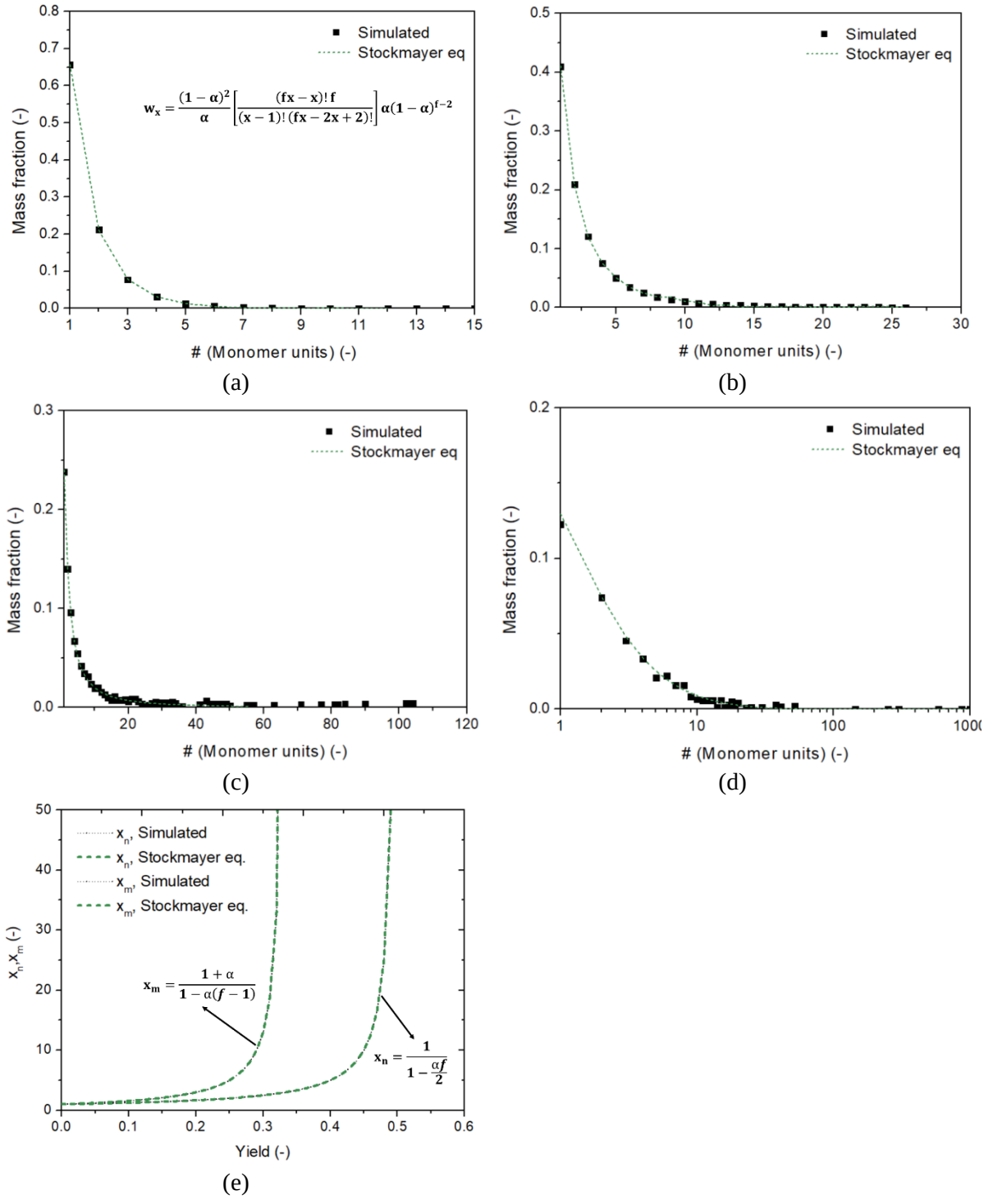

Supplementary Figure 17: Benchmark for simulations results considering network chemistry 1 for (a)-(d) mass chain length distribution at different yields (0.1, 0.2, 0.3, 0.4) and (e) number average chain length x_n and mass average chain length x_m as function of yield. An excellent match is obtained with the analytical expression of Stockmayer[59] for multifunctional condensation polymerization (see extra equations in (a) and (e): f = functionality of monomer unit, x is the number of units in the molecule and α the yield of reaction, so our Supplementary equation (5); extension of the work of Flory for linear condensation polymerizations). The assumptions for this analytical derivation, as included for the benchmark, are equal functional group reactivity and the absence of intramolecular reactions (Supplementary Figure 20a with such reactions).

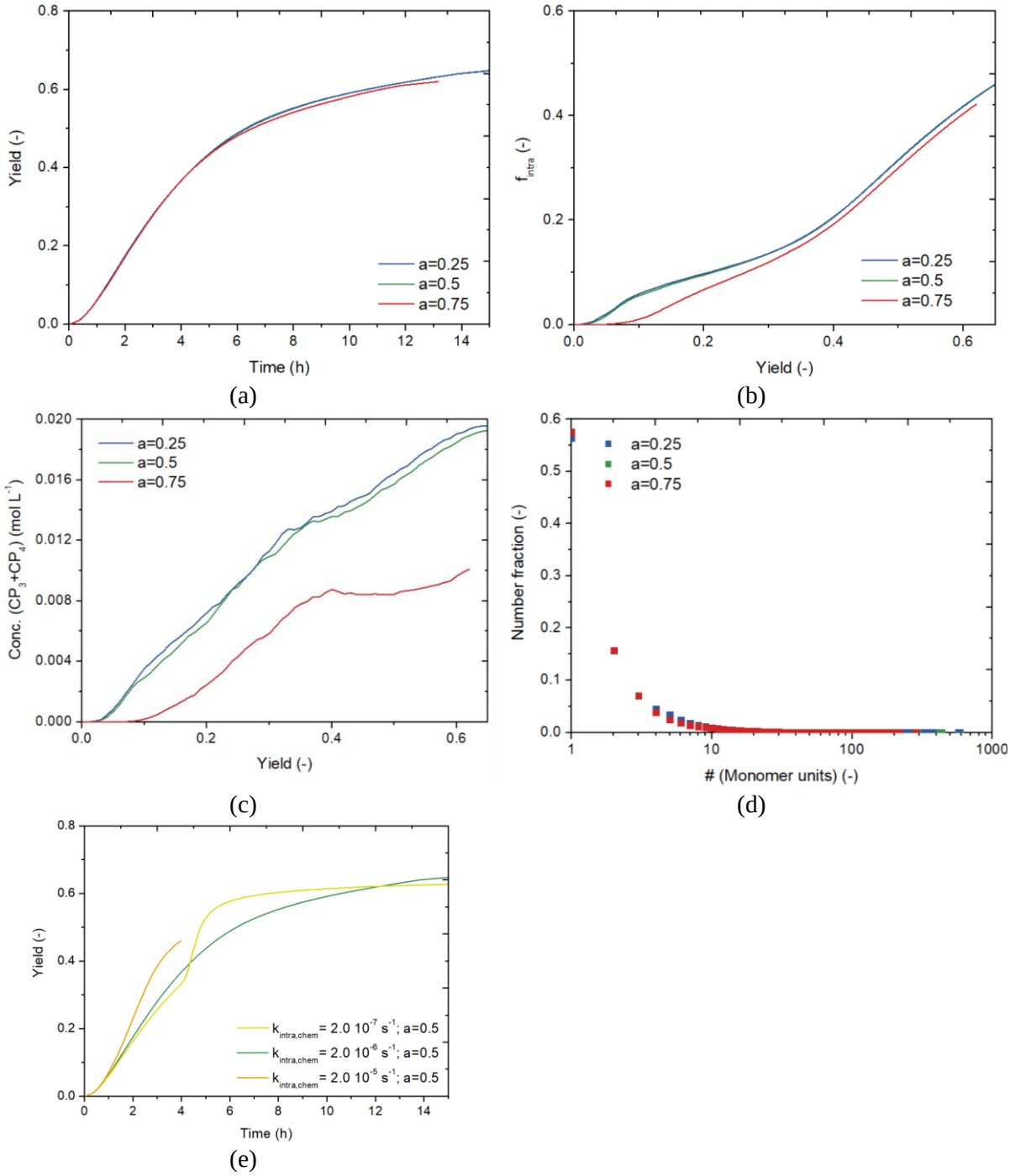

Supplementary Figure 18: Illustration of the relevance of diffusional limitations for intramolecular reactions in polymer network synthesis by formally varying the necessary compactness of the molecules as expressed by $\sqrt{N_c'/n'}$ (N_c' = number of CPs and n' = number of monomer units along shortest path between two FGs; Supplementary Equation (15); box F in Supplementary Figure 1). Examples given for network chemistry 1 (initial conditions and parameters in Supplementary Table 1): (a) Yield as function of synthesis time, (b) Fraction of intramolecular reactions as function of yield, (c) Concentration of molecules with at least 3 crosslinking points (CP(s) crosslinked 3 or 4 times (CP_3+CP_4) as function of yield and (d) number chain length distribution at yield of 0.6; simulation results for a = 0.25 (blue), a = 0.5 (green; selected value in the main text) and a = 0.75 (red). It follows that the use of a value of 0.5 is a physical boundary. (e) Parameter screening for the determination of the intrinsic intramolecular rate coefficient once a value of 0.5 is selected for the distance rule criteria (green line as in Figure 3 in main text thus according to the experimental data).

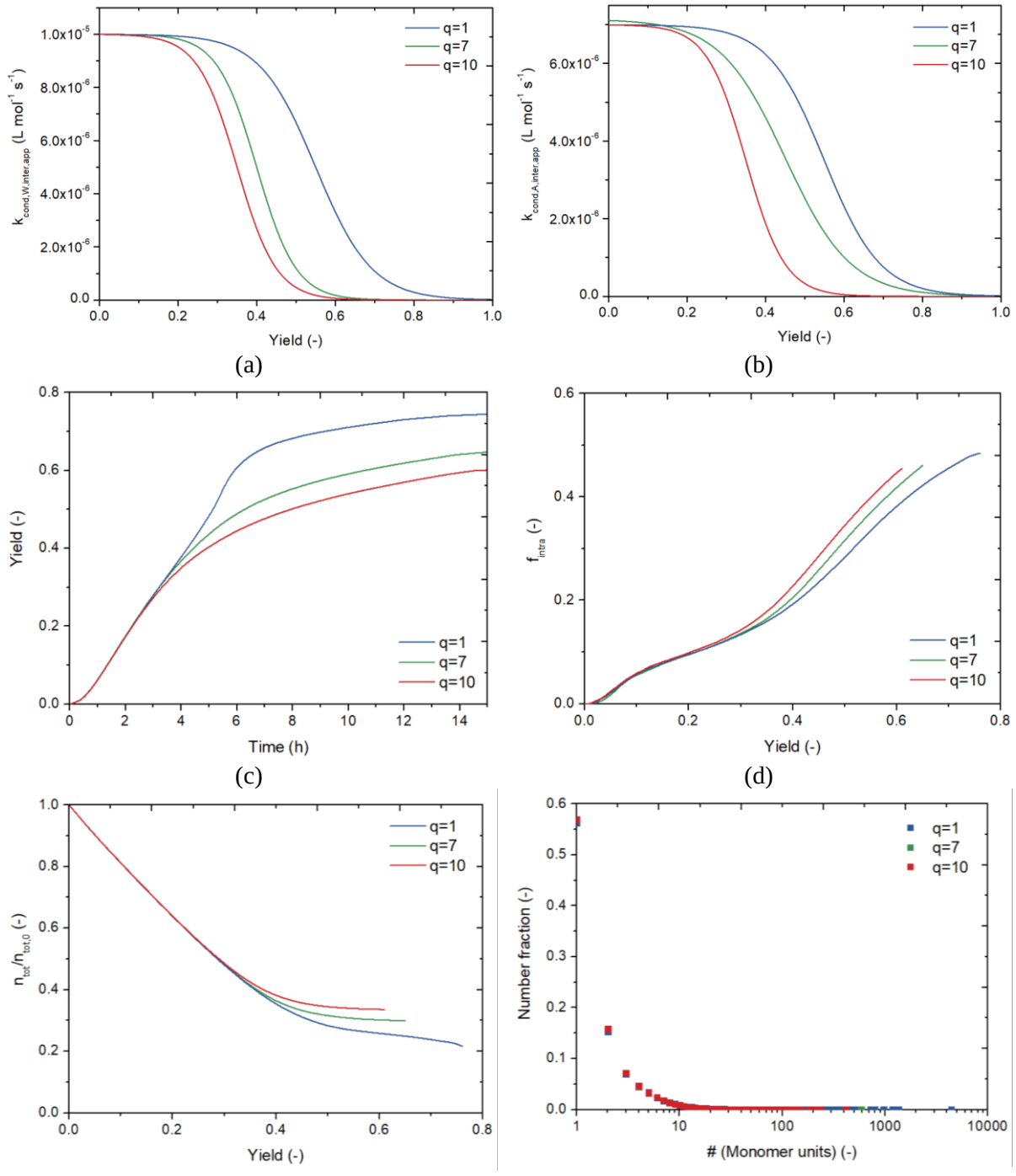

Supplementary Figure 19: Illustration of the relevance of diffusional limitations for intermolecular reaction in polymer network synthesis by formally varying the impact of the number of crosslinking points to the decrease in the diffusion coefficient as represented by *q* in Supplementary Equation (14). Examples given for network chemistry 1 (initial conditions and parameters in Supplementary Table 1): (a) apparent rate coefficient for intermolecular water condensation (L mol^{-1} s^{-1}) as function of yield, (b) apparent rate coefficient for intermolecular alcohol condensation (L mol^{-1} s^{-1}) as function of yield, (c) yield as function of synthesis time, (d) fraction of intramolecular reactions as function of yield, (e) decrease in number of molecules as function of yield and (f) number chain length distribution for yield of 0.6; simulation results for *q* = 1 (blue), *q* = 7 (green; optimized value based on Supplementary Figure 12a) and *q* = 10 (red).

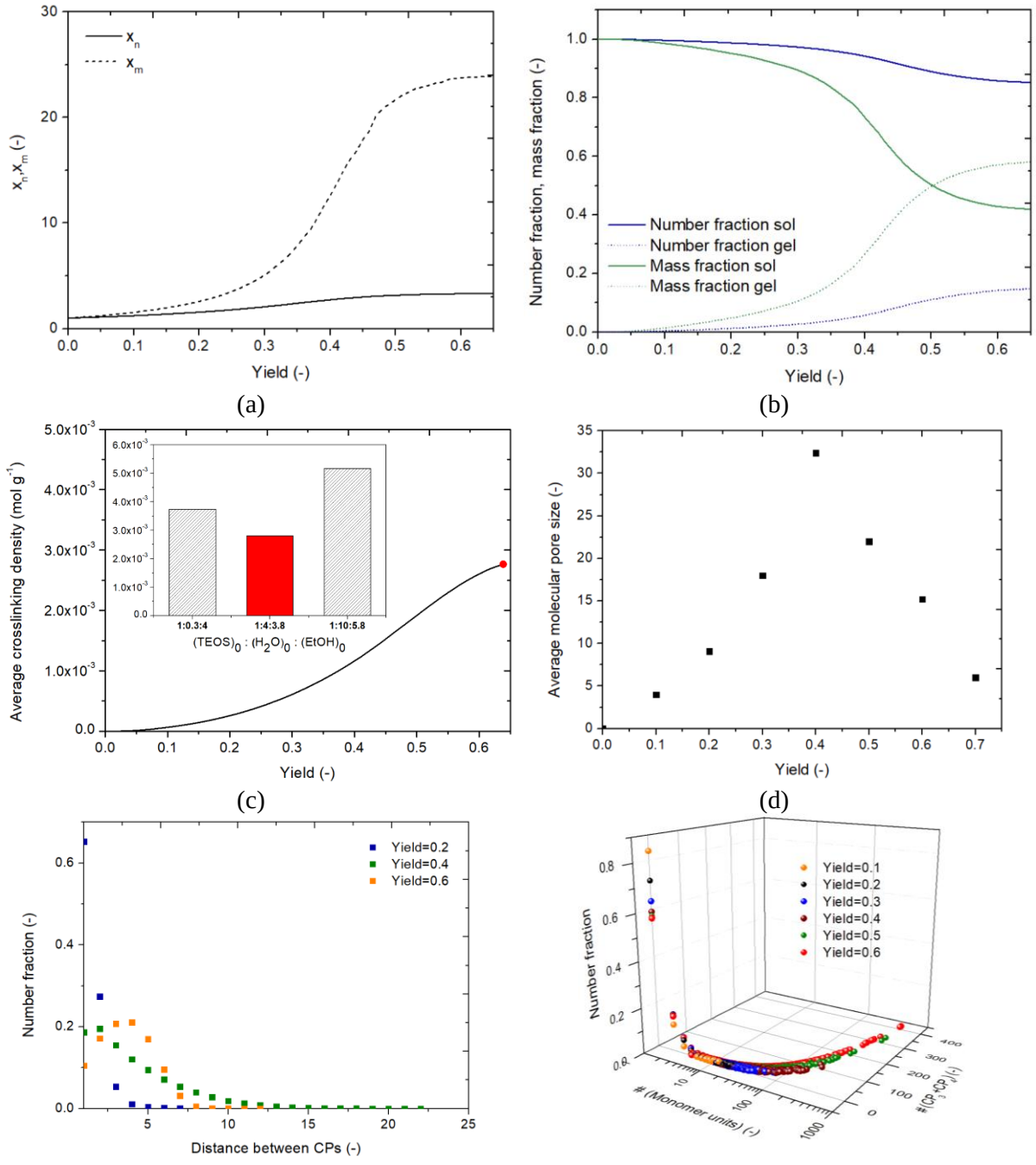

Supplementary Figure 20: Examples of molecular descriptors that can be derived from the developed generic modeling platform as defined by the flowsheets in Supplementary Figure 1-4. This figure is complementary to the bottom layer of Figure 3 in the main text; Examples given for network chemistry 1 (initial conditions and parameters in Supplementary Table 1): (a) number and mass average chain length x_n and x_m as function of yield, (b) number/mass fraction sol/gel as function of yield, (c) average crosslinking density (mol g^{-1}; with respect to the initial TEOS mass) as function of yield and also final value for this condition and two more (extra upper graph), (d) number average molecular pore size as a function of yield; (e) number distribution of distance between crosslinking points (CPs) in number of monomer units (the average distance between CPs first increases due to the dominance of intermolecular reactions and then decreases due to the dominance of intramolecular reactions) and (f) bivariate distribution over number of monomer units and number of CPs with at least 3 crosslinks (notation CP_3 + CP_4).

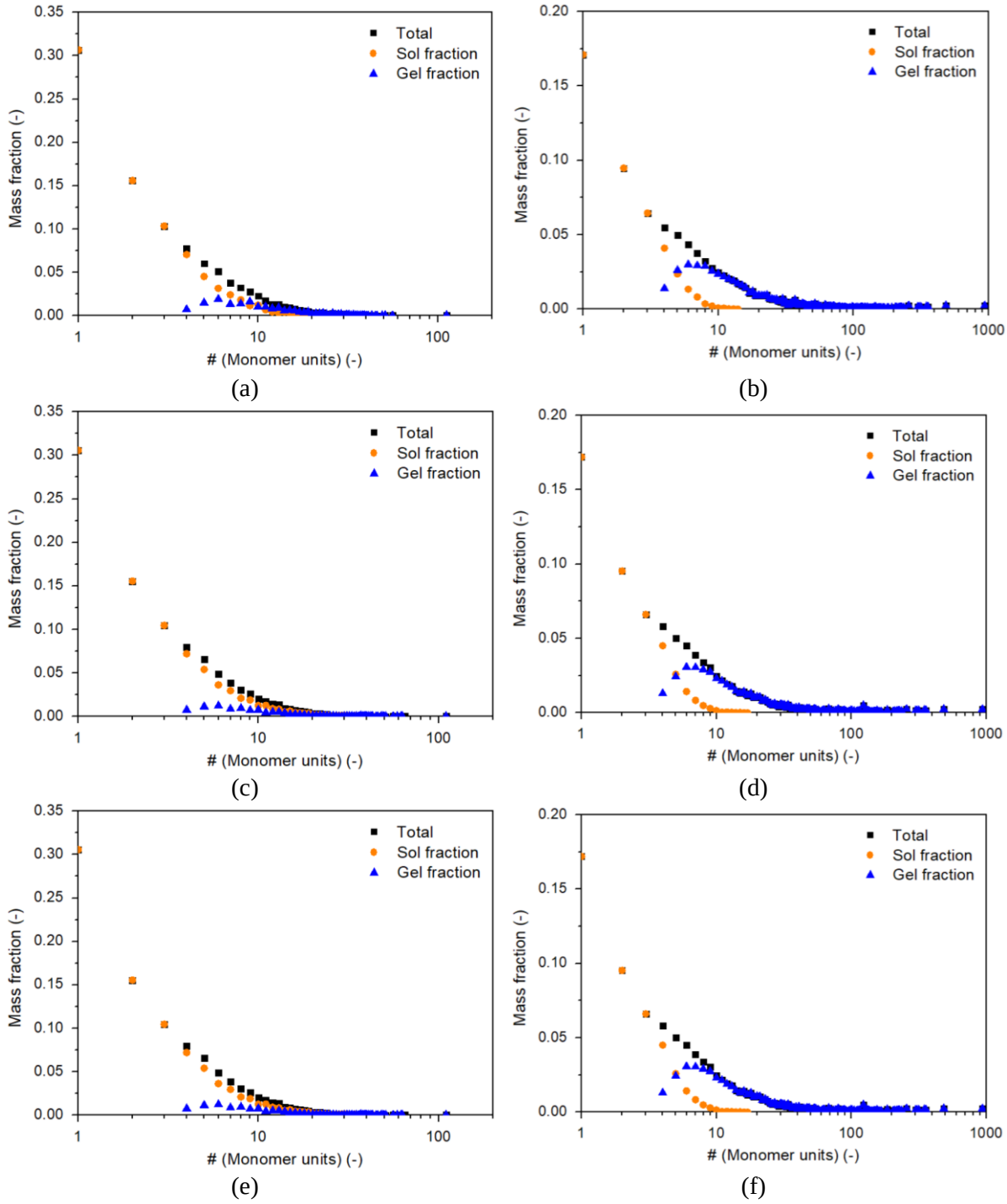

Supplementary Figure 21: Sensitivity analysis regarding the split-up in a sol and gel contribution for the mass chain length distribution (CLD) based on the compactness of the complete molecule as represented by N_c/n (N_c = number of CPs (CP_3+CP_4) in a molecule and n = number of monomer units in a molecule). (Top) with cut-off $N_c/n = 0.3$; (Middle; used in the main text) with cut-off $N_c/n = 0.5$; (Bottom) with cut-off $N_c/n = 0.7$; Examples given for network chemistry 1 (initial conditions and parameters in Supplementary Table 1): (a), (c) and (e) yield = 0.3; (b), (d) and (f) yield = 0.6. Minor differences are observed displaying the strength of the selected criterion.

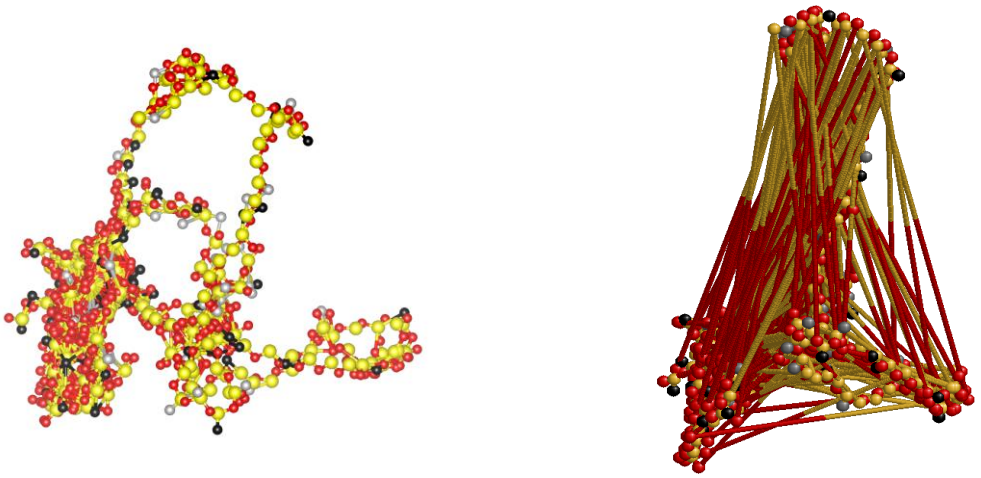

(a)

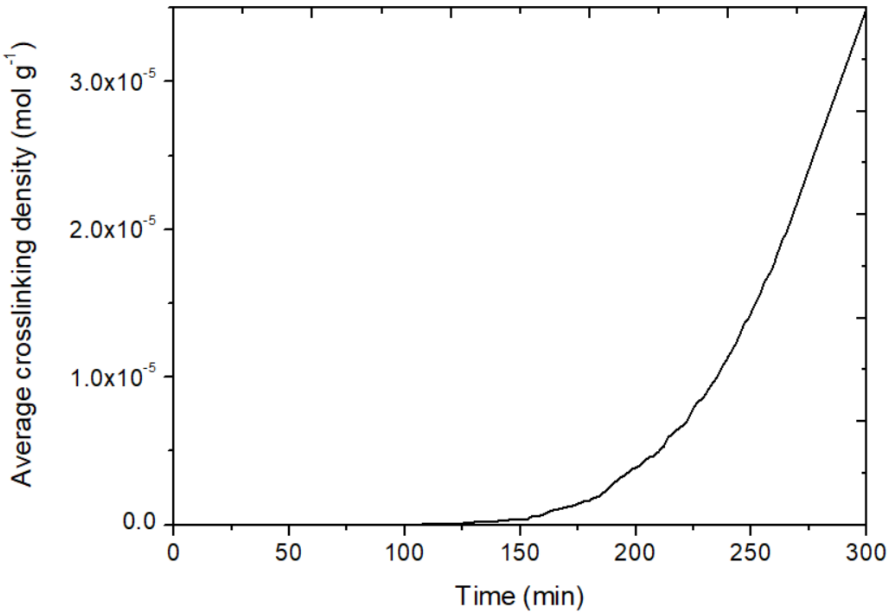

(b)

Supplementary Figure 22: (a) Left figure is the same is in Figure 4a focusing on the main loops. Right figure formally highlights all connectivities and (b) additional information for Figure 4b in the main text displaying the variation of the average crosslinking density (with respect to initial bisphenol F diglycidylether mass)

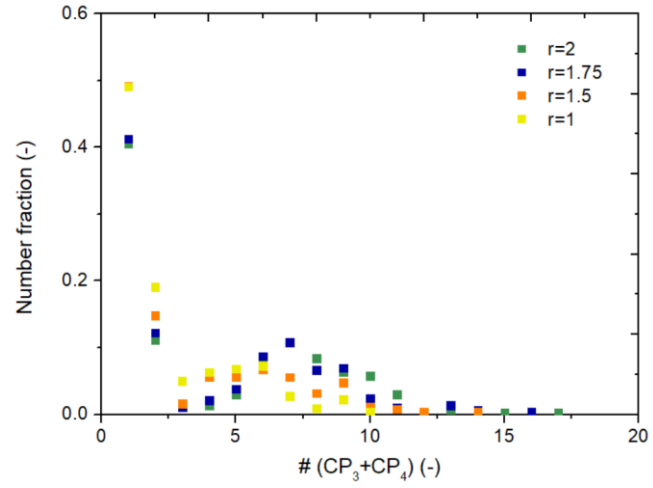

(a)

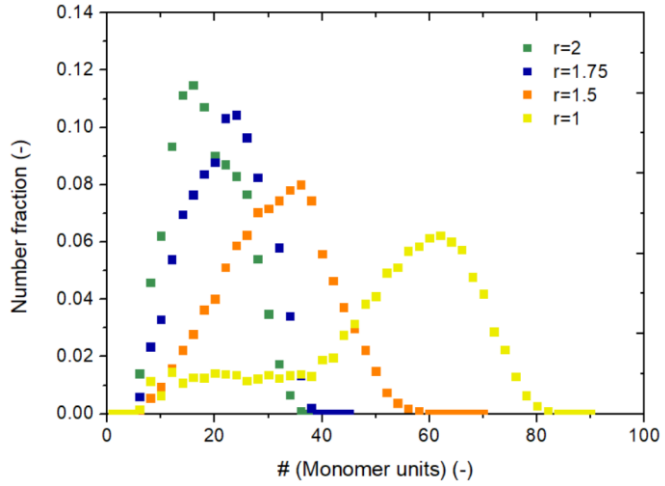

(b)

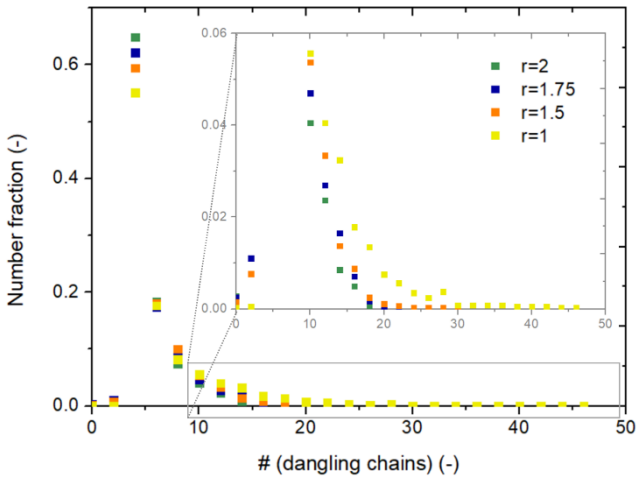

(c)

Supplementary Figure 23: Molecular distributions corresponding to Figure 4c in the main text (chemistry 3): (a) crosslinking point CP distribution (at least 3 crosslinks; CP_3 + CP_4 notation), (b) molecular pore size distribution (mPSD) and (c) dangling chain distribution; *r* represents the initial molar ratio of bifunctional monomer to tetrafunctional monomer.

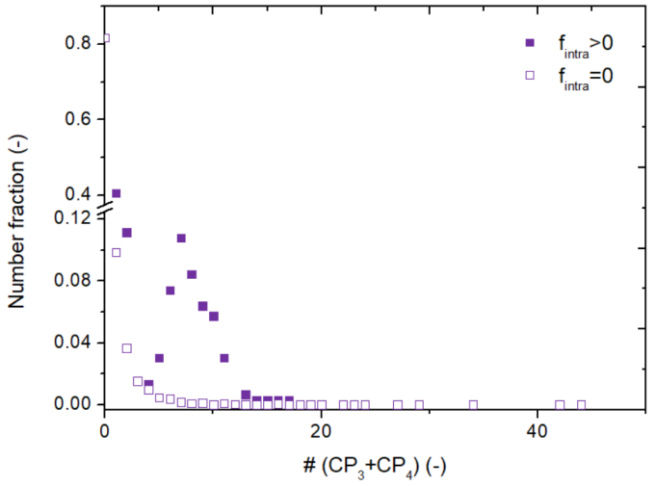

(a)

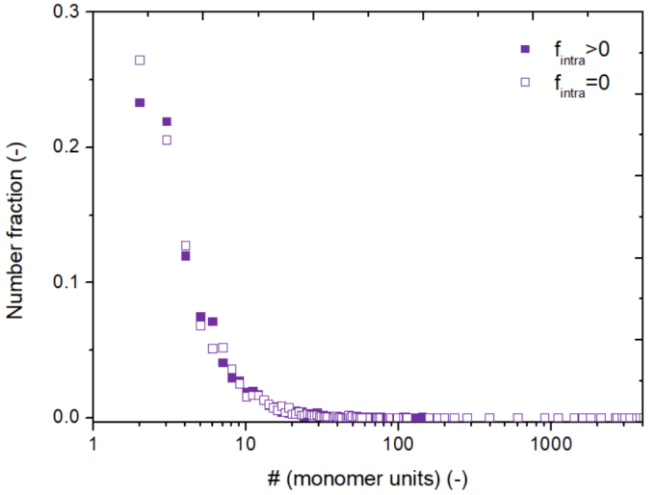

(b)

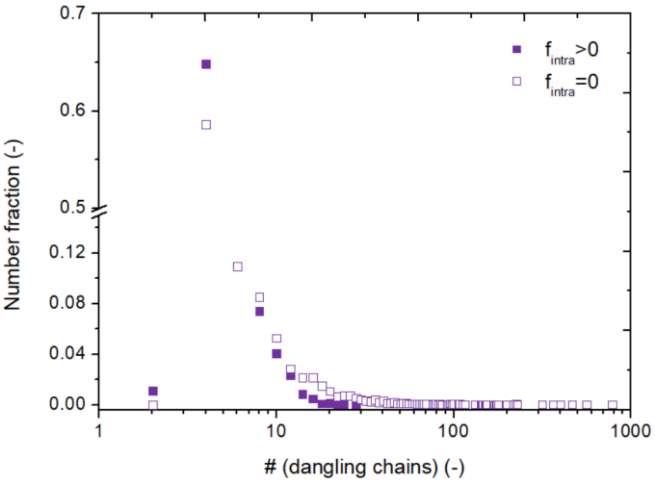

(c)

Supplementary Figure 24: Impact of non-ideality as illustrated using chemistry 3 (additional information for Figure 4c and 5a in the main text); ideal: f_{intra} = 0 and open symbols, and non-ideal: f_{intra} > 0 and closed symbols; r = 2; (a) crosslinking point (CP) distribution (at least 3 crosslinks; CP_3 + CP_4 notation), (b) chain length distribution and (c) dangling chain distribution.

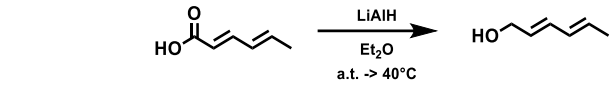

(1)

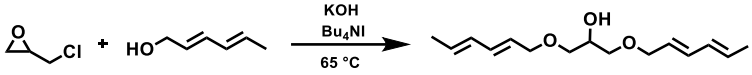

(2)

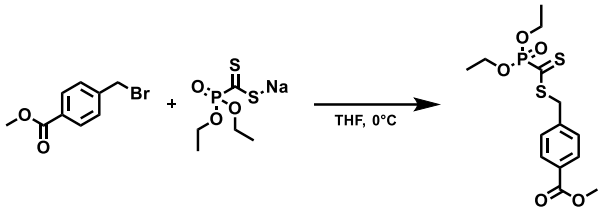

(3)

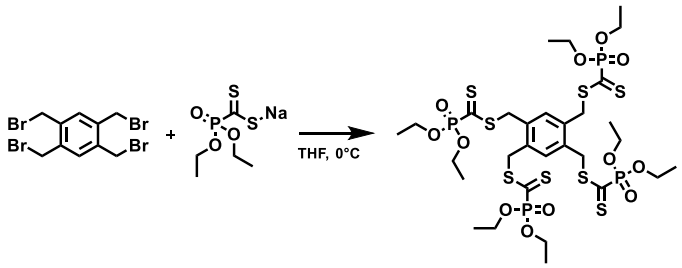

(4)

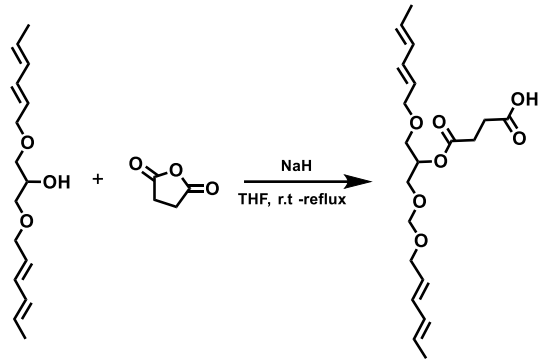

(5)

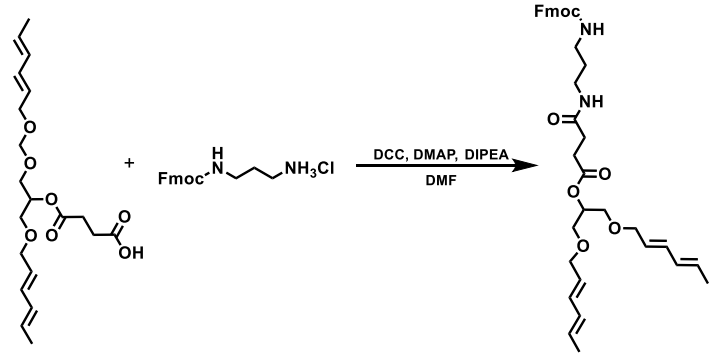

(6)

Supplementary Figure 25: Reactions related to preparation of monomers for chemistry 3: trans,trans-hexa-2,4-dienol (sorbic alcohol) (1); 1,3-bis(((2E,4E)-hexa-2,4-dien-1-yl)oxy)propan-2-ol (bifunctional linker) (2); methyl 4-((((diethoxyphosphoryl)carbonothioyl)-thio)methyl)benzoate (3); benzene-1,2,4,5-tetrayltetrakis(methylene)tetrakis((diethoxy-phos-phoryl)methanedithioate) (tetrafuncti-onal linker) (4); 4-((1-(((2E,4E)-hexa-2,4-dien-1-yl)oxy)-3-((((2E,4E)-hexa-2,4-dien-1-yl)oxy)methoxy)propan-2-yl)oxy)-4-oxobutanoic acid (bifunctional linker-COOH) (5) and 1,3-bis(((2E,4E)-hexa-2,4-dien-1-yl)oxy)propan-2-yl-4-((3-((((9H-fluoren-9-yl)methoxy)carbonyl) amino)propyl)amino)-4-oxobutanoate (bifunctional linker-Fmoc) (6). Phase 3b in het main text is between the products of reaction (3) and (4); phase 3c between a 50/50 molar mixture of the products of reaction (3) and (6), and (4); FMOC can be released.

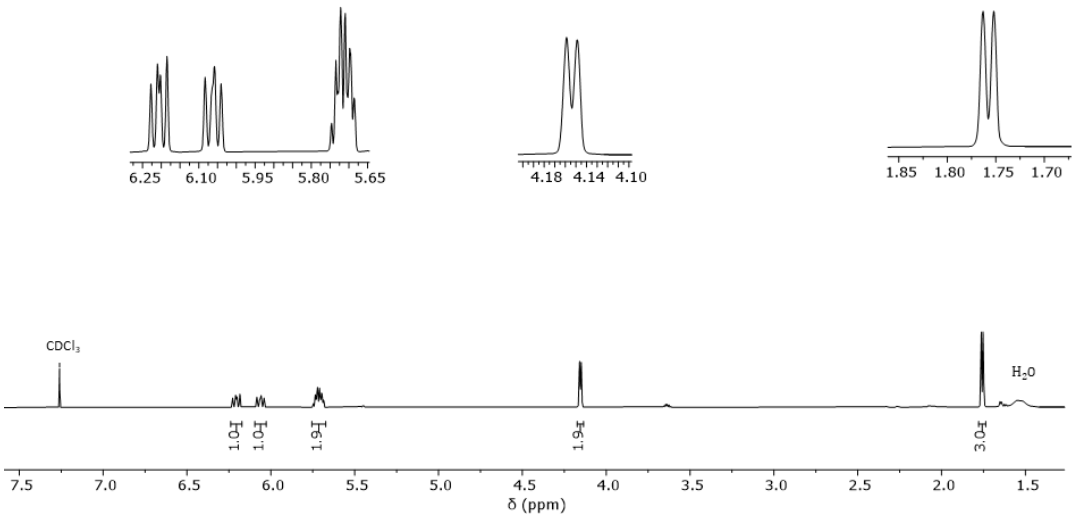

(a)

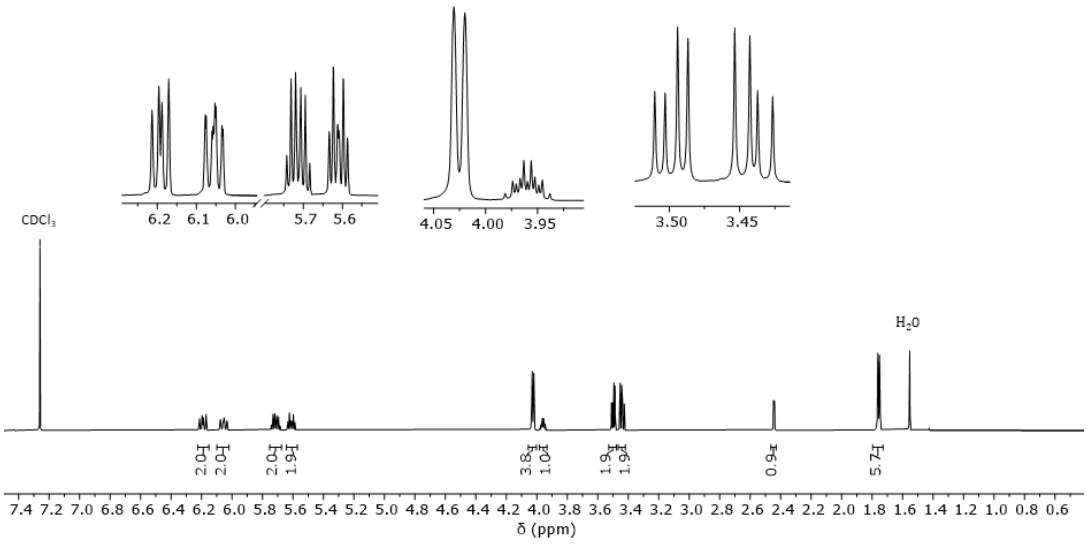

(b)

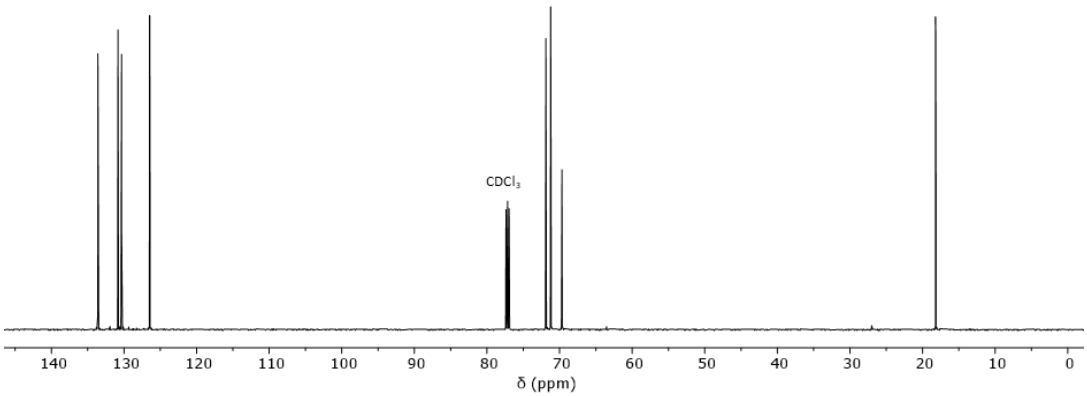

(c)

Supplementary Figure 26: Extra analytical details related to Supplementary Figure 25: (a) ^{1}H-nuclear magnetic resonance (NMR) spectrum of sorbic alcohol in deuterated chloroform (CDCl3) and (b) ^{1}H-NMR spectrum of phase 3b bifunctional linker in CDCl3 and (c) ^{13}C-NMR spectrum of bifunctional linker in CDCl3.

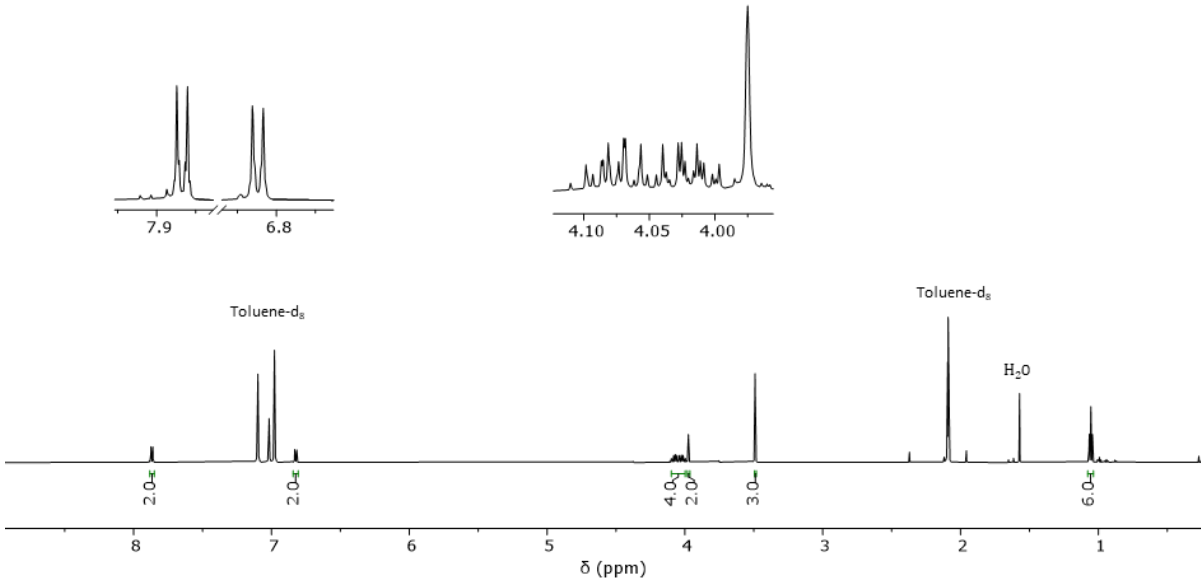

(a)

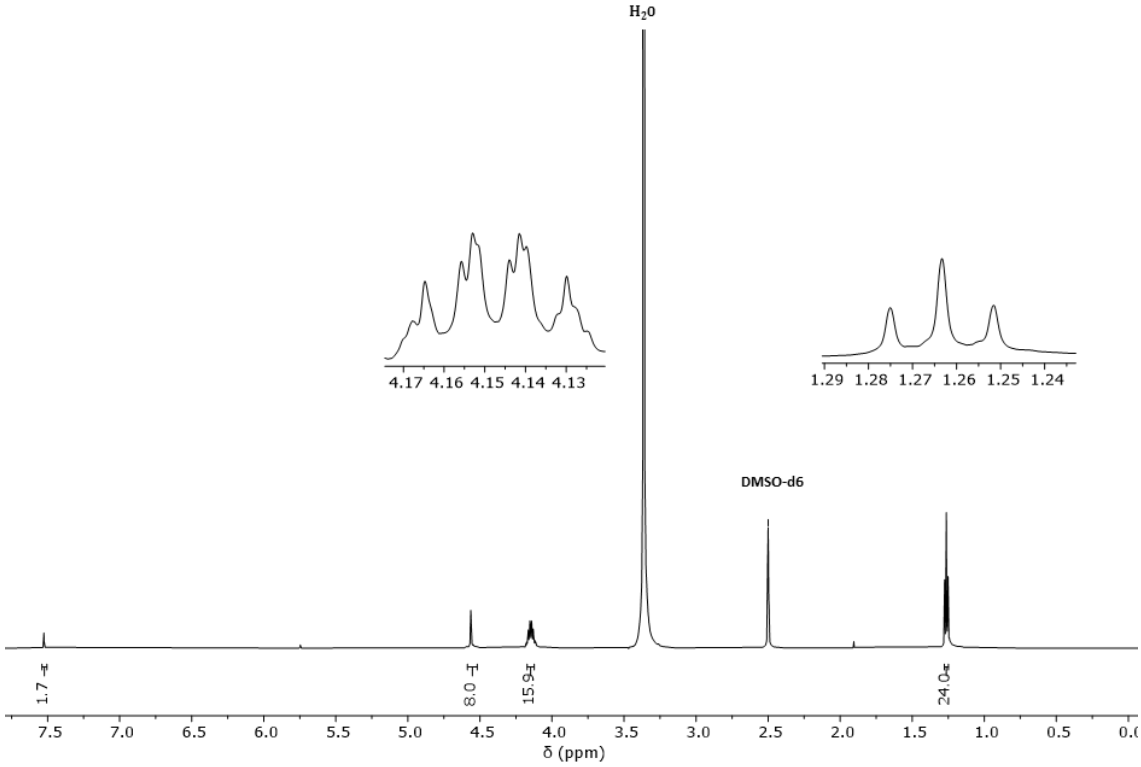

(b)

Supplementary Figure 27: Extra analytical details related to Supplementary Figure 25: (a) ^{1}H-nuclear magnetic resonance (NMR) spectrum of methyl 4-((((diethoxyphosphoryl)carbonothioyl)-thio)methyl)benzoate in toluene-d8 and (b) ^{1}H-NMR spectrum of tetrafunctional linker in dimethylsulfoxide-d_6.

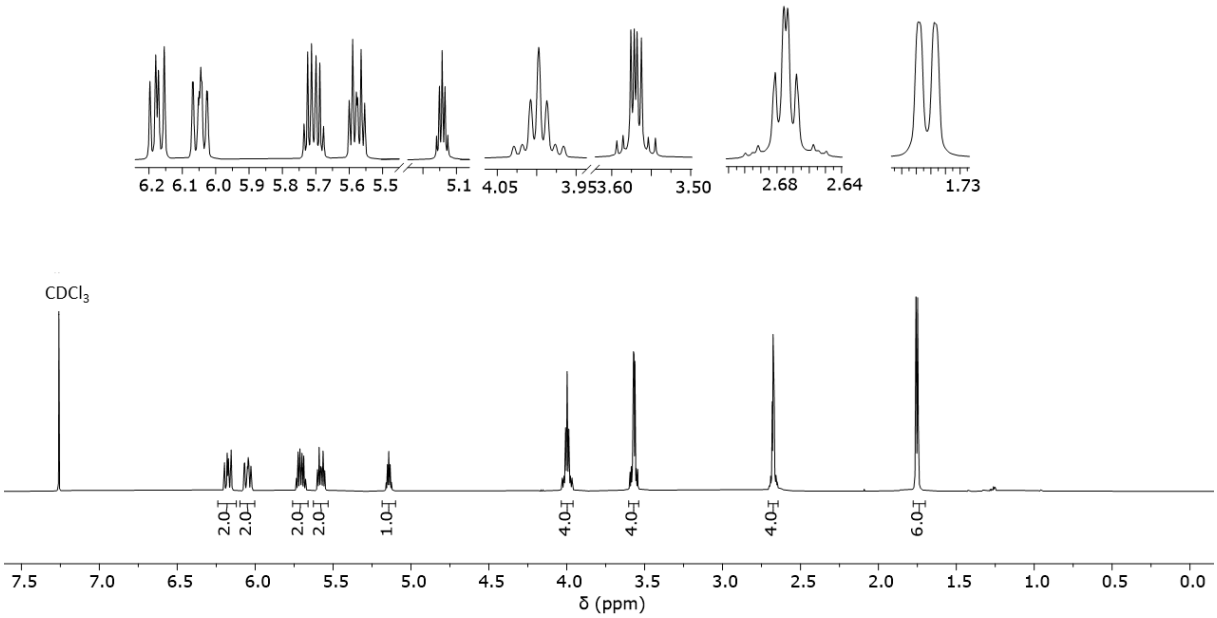

(a)

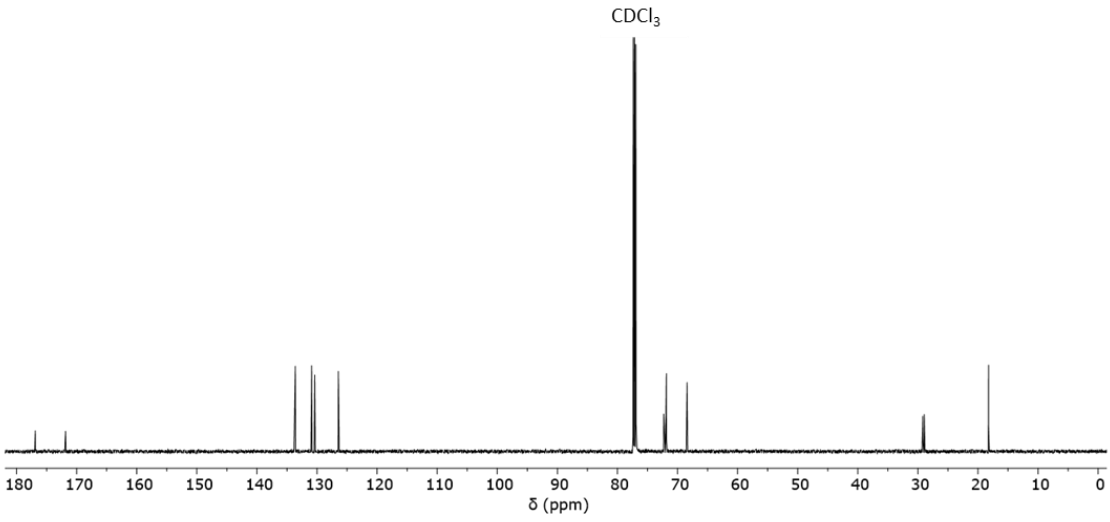

(b)

Supplementary Figure 28: Extra analytical details related to Supplementary Figure 25 (phase 3c): (a) ^{1}H-nuclear magnetic resonance (NMR) spectrum of bifunctional linker-COOH in $CDCl_3$ and (b) ^{13}C-NMR spectrum of bifunctional linker-COOH in $CDCl_3$.

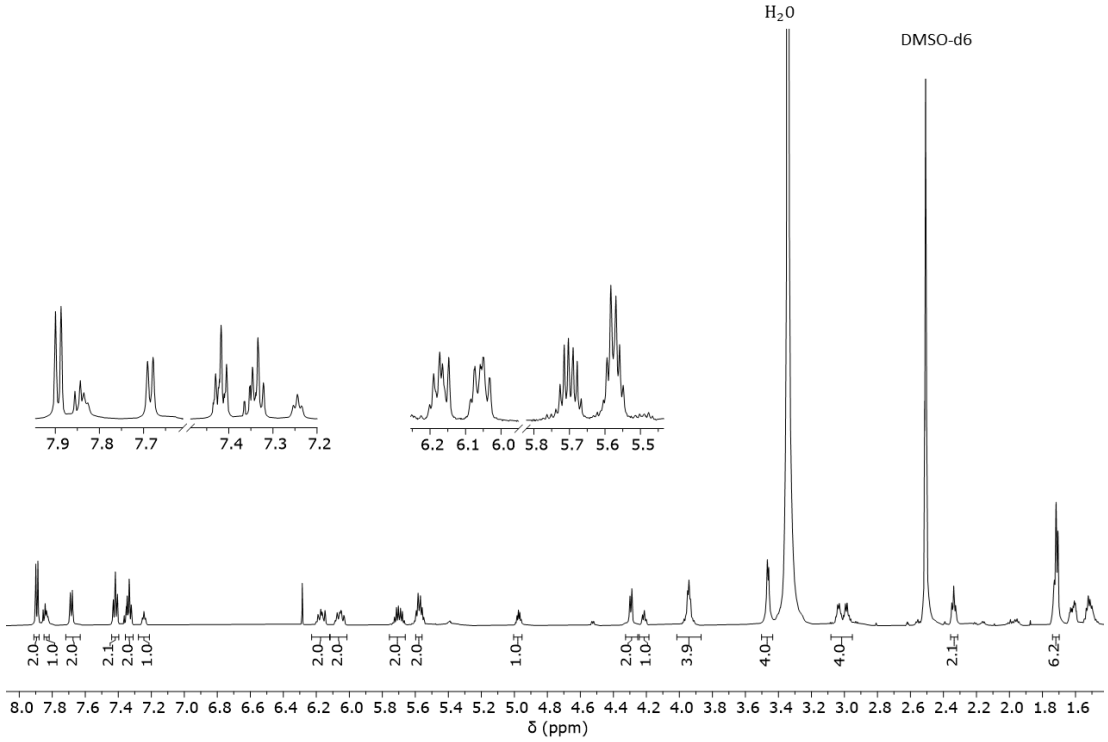

(a)

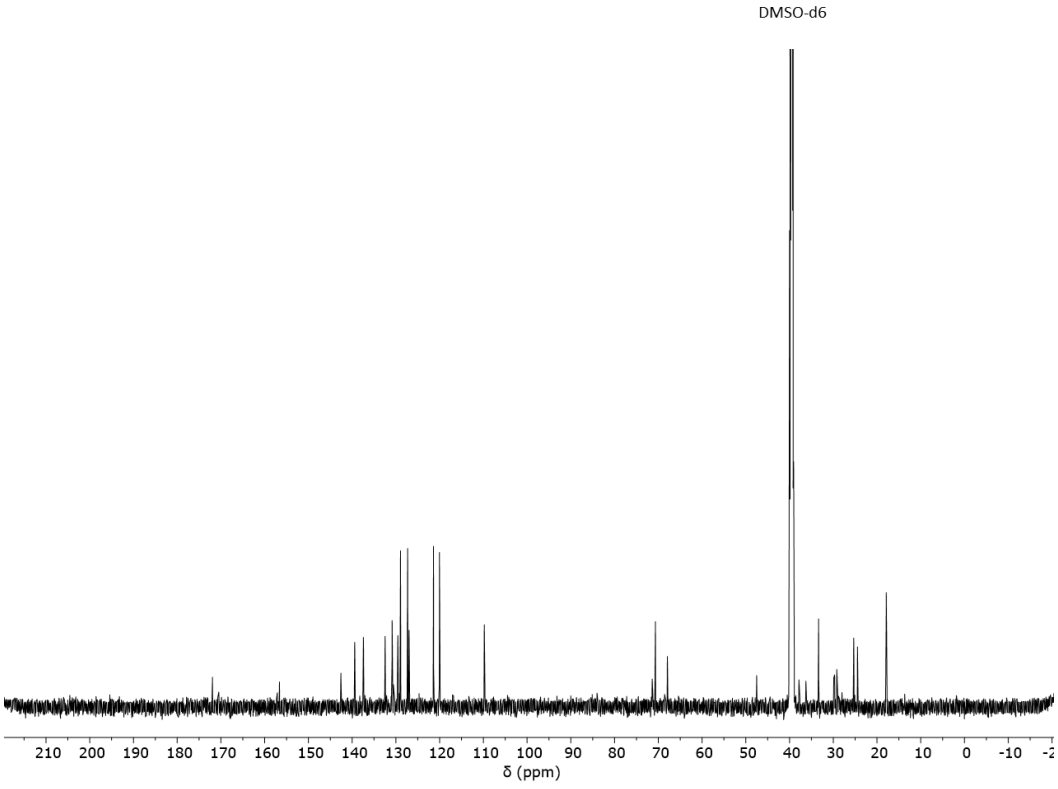

(b)

Supplementary Figure 29: Extra analytical details related to Supplementary Figure 25 (phase 3c): (a) ^{1}H-nuclear magnetic resonance (NMR) spectrum of bifunctional linker-Fmoc in DMSO-*d*$_6$ and (b) ^{13}C-NMR spectrum of bifunctional linker-Fmoc in DMSO-*d*$_6$.

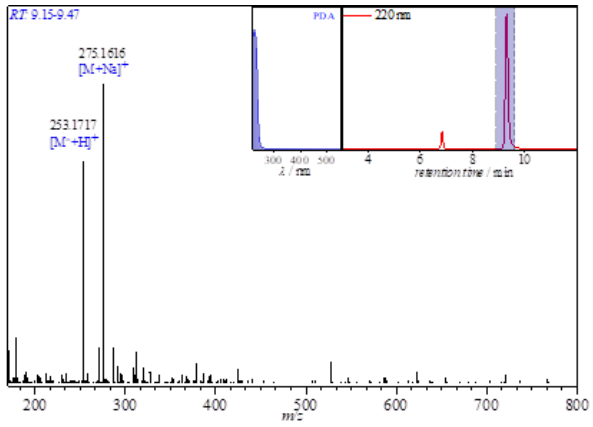

(a)

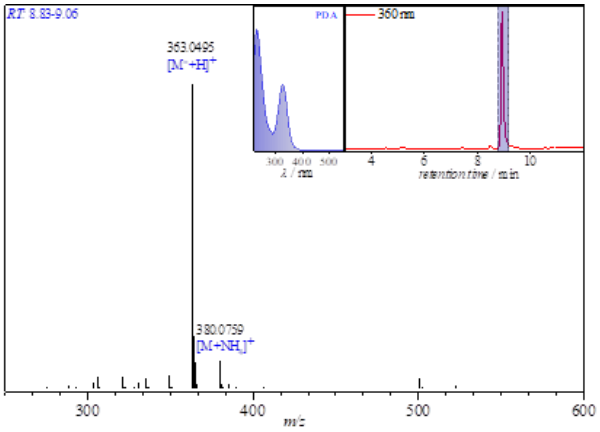

(b)

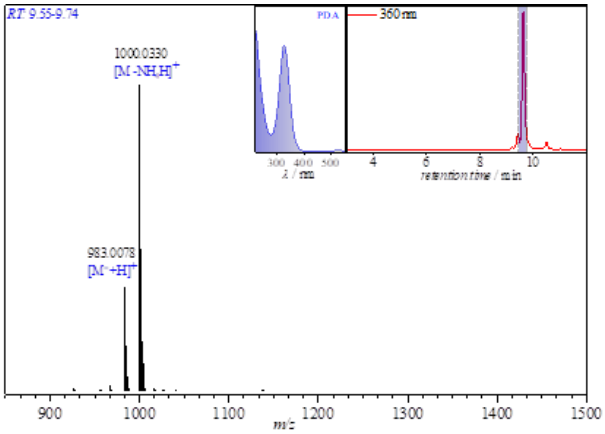

(c)

Supplementary Figure 30: Extra analytical details related to Supplementary Figure 25: (a) LC-ESI-HRMS spectrum of bifunctional linker (phase 3b), (b) LC-ESI-HRMS spectrum of methyl 4-((((diethoxyphosphoryl)carbonothioyl)-thio)methyl)benzoate (phase 3b) and (c) LC-ESI-HRMS spectrum of tetrafunctional linker (phase 3b and 3c)

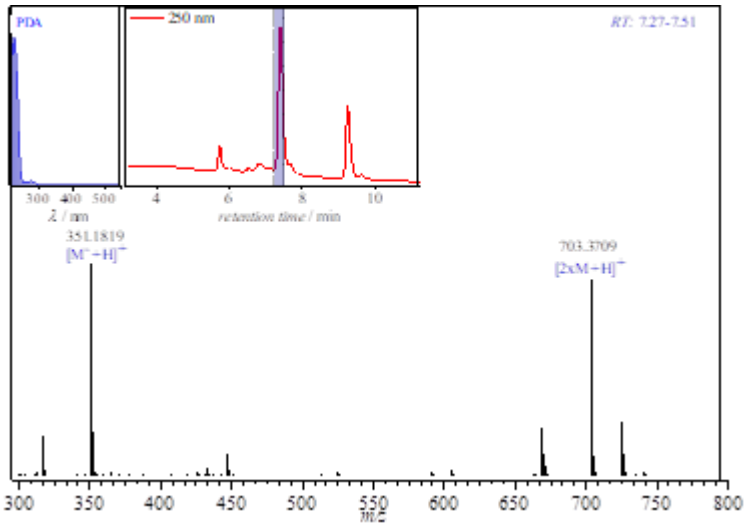

(a)

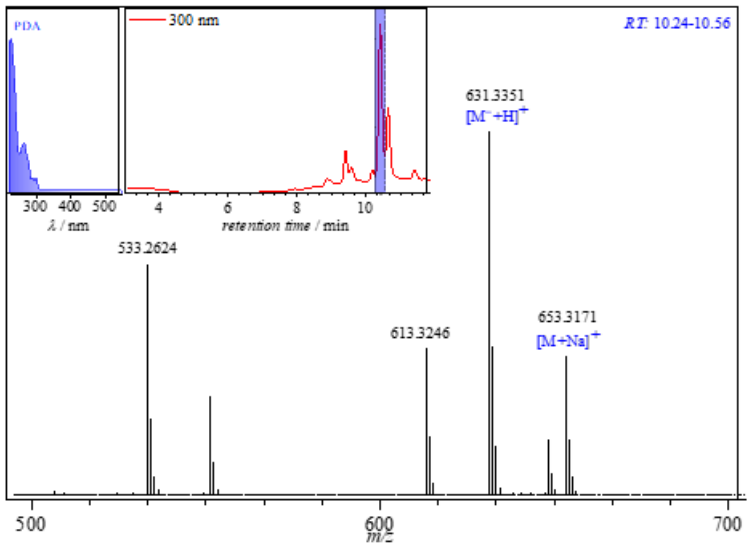

(b)

Supplementary Figure 31: Extra analytical details related to Supplementary Figure 25 (phase 3c): (a) LC-ESI-HRMS spectrum of bifunctional linker-COOH and (b) LC-ESI-HRMS spectrum of bifunctional linker-Fmoc.

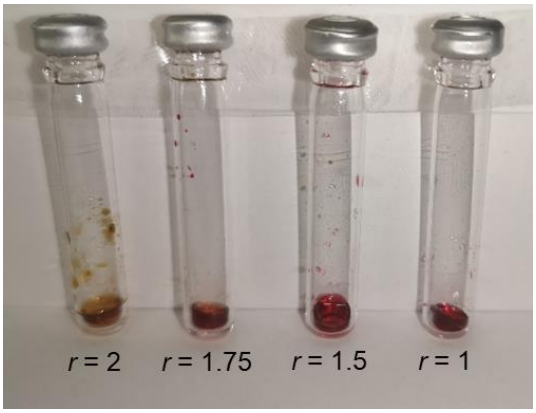

(a)

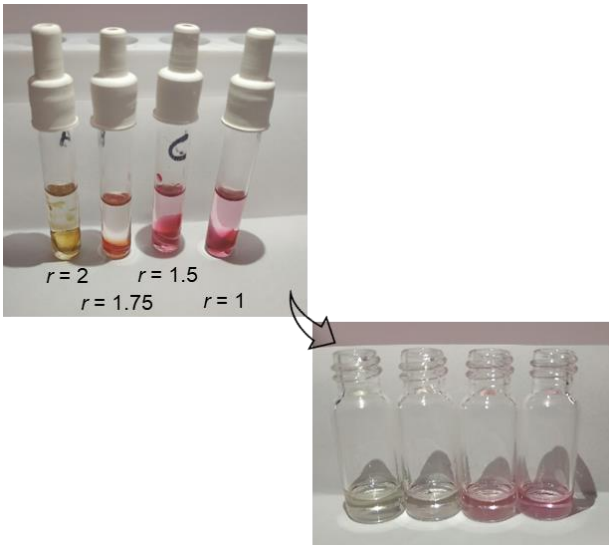

(b)

(c)

Supplementary Figure 32: Images of synthesized networks using the original bifunctional monomer (phase 3b) (a) and the Fmoc-loaded bifunctional monomer (phase 3c) (c); additionally in (b) the networks with the original bifunctional monomer shown after swelling in toluene, together with the remaining solution after swelling upon removal of the networks; a pink solution is obtained for the most off-stoichiometric initial conditions (*r*=1) due to the remaining presence of the tetrafunctional linker.

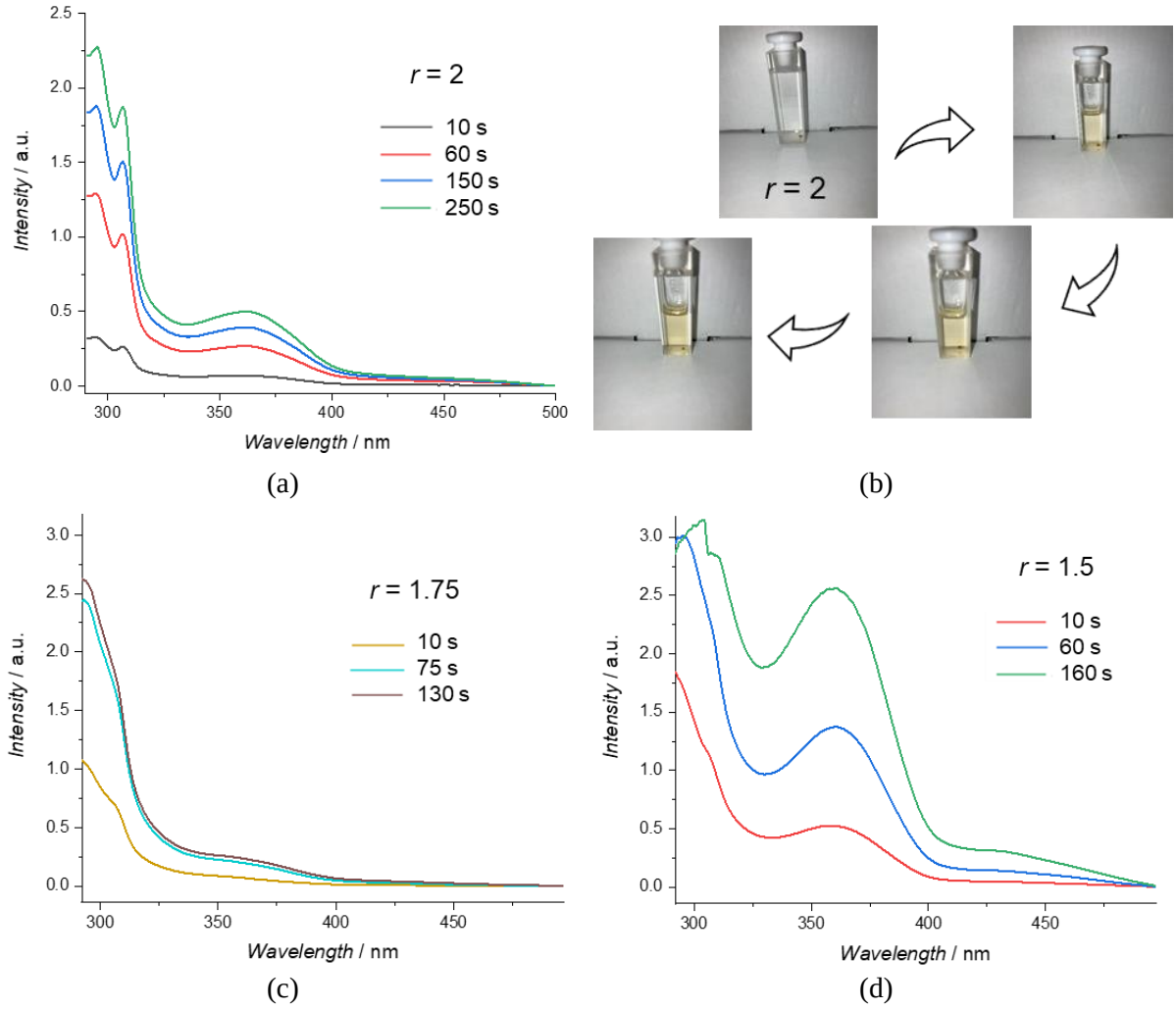

Supplementary Figure 33: UV/Vis spectrum of Fmoc release related to Figure 5 in main text for the network synthesis with different *r* values (*r* = initial molar ratio of Fmoc-loaded bifunctional monomer to tetrafunctional monomer): (a) *r* = 2, additionally pictures in (b) showing the change in color intensity with increasing release time, (c) *r* = 1.75 and (d) *r* = 1.5; quantification of Fmoc release at 304 nm.

Supplementary Tables

Supplementary Table 1: Input variables for the kinetic Monte Carlo (*k*MC) simulation (Supplementary Figure S1; box A) for the organosilica network synthesis case (network chemistry 1 in the main text; employed for Figure 3 and Figure 4a in the main text); distinction between inter- and intramolecular reactions.

	Equation	k_{chem} **at 298 K[a] ((L mol^{-1}) s^{-1})**
Hydrolysis	$-OR + H-OH \xrightarrow{f_i k_{hydro}} -OH + R-OH$	1.2 10^{-5} f_4=1; f_3=6; f_2=3; f_1=2
Reesterification	$-OH + R-OH \xrightarrow{k_{hydro,rev}} -OR + H-OH$	2.4 10^{-6}
Water condensation - intermolecular	$-OH + -OH \xrightarrow{k_{cond,W,inter}} -O- + H_2O$	1.0 10^{-5}
Water condensation – intramolecular	$-OH + -OH \xrightarrow{k_{cond,W,intra}} -O- + H_2O$	2.0 10^{-6}
Hydrolysis siloxane bonds	$-O- + H_2O \xrightarrow{k_{cond,W,rev}} -OH + -OH$	0.0
Alcohol condensation – intermolecular	$-OR + -OH \xrightarrow{k_{cond,A,inter}} -O- + R-OH$	7.0 10^{-6}
Alcohol condensation – intramolecular	$-OR + -OH \xrightarrow{k_{cond,A,intra}} -O- + R-OH$	1.4 10^{-6}
Alcoholysis	$-O- + R-OH \xrightarrow{k_{cond,A,rev}} -OR + -OH$	0.0

Initial concentrations and number of molecules[g]

	Initial concentration (mol L^{-1})	**Initial nr of molecules[b] (-)**
TEOS monomer[c]	2.0	250000
H_2O	8.0	1000000
EtOH	7.6	950000

Diffusion parameters[d]

	V_i^* **(m^3 kg^{-1})**	$M_{j,i}$ **(kg mol^{-1})**	$K_{1,i}/\gamma$ **(m^3 kg^{-1} K^{-1})**	$K_{2,i}$-$T_{g,i}$ **(K)**	$D_{0,i}$ **(m^2 s^{-1})**
TEOS monomer[e]	0.905 10^{-3}	0.208	9.32 10^{-7}	-81.0	1.5 10^{-8}
H_2O	1.071 10^{-3}	0.018	2.18 10^{-6}	-152.29	8.55 10^{-8}
EtOH[f]	0.961 10^{-3}	0.046	1.17 10^{-6}	-48.41	8.75 10^{-8}
Lennard Jones parameter	6.0 10^{-10} m				

[a]for intermolecular contributions based on data in Supplementary Figure 11a-c and Supplementary Figure 12a; reactions in Supplementary Figure 5 and 8; for intermolecular contributions based on data in Supplementary Figure 12d and Figure 4b in the main text; [b]allowing numerical convergence as shown in Supplementary Figure 16; [c]df (degree of functionalization)=4; [d]based on literature data;[51,60] parameter q in Supplementary equation 14 equal to 7 based on Supplementary Figure 12(c); [e]values taken for poly(dimethylsiloxane); [f]values taken for methanol; [g]for Fig. 4a in the main text this becomes 2.5 10^5 TEOS, 7.5 10^4 H_2O and 1.2 10^7 EtOH molecules for $(H_2O)_0$:$(TEOS)_0$ = 0.3, 2.5 10^5 TEOS, 1.0 10^6 H_2O and 1.2 10^7 EtOH molecules for $(H_2O)_0$:$(TEOS)_0$ = 4 and 2.5 10^5 TEOS, 2.5 10^6 H_2O and 1.2 10^7 EtOH molecules for $(H_2O)_0$:$(TEOS)_0$ = 10; conditions taken from Xia et al.[61]

Supplementary Table 2: Input variables for the kinetic Monte Carlo (*k*MC) simulation (Supplementary Figure S1; box A) for the epoxy-amine curing case (network chemistry 2 in the main text; employed for Figure 4b in the main text); distinction between inter- and intramolecular reactions.

	Equation	k_{chem} at 298 K[a] ($(L^{(2)}\ mol^{-(2)})\ s^{-1}$)
Primary amine curing – intermolecular	$-PA + -EP \xrightarrow{k_{PA,inter}} -SA + -OH$	6.0 10^{-6} [c]
Primary amine curing – intermolecular[d]	$-PA + -EP + -OH \xrightarrow{k_{PA,inter,cat}} -SA + -OH$	2.0 10^{-6}
Primary amine curing – intramolecular[d]	$-PA + -EP + -OH \xrightarrow{k_{PA,intra,cat}} -SA + -OH$	4.0 10^{-7}
Secondary amine curing – intermolecular[d]	$-SA + -EP + -OH \xrightarrow{k_{SA,inter,cat}} -TA + -OH$	1.0 10^{-6}
Secondary amine curing – intramolecular[d]	$-SA + -EP + -OH \xrightarrow{k_{SA,intra,cat}} -TA + -OH$	2.0 10^{-7}
Etherification – intermolecular[d]	$-OH + -EP + -OH \xrightarrow{k_{ether,inter,cat}} -X$	0.0
Etherification – intramolecular[d]	$-OH + -EP + -OH \xrightarrow{k_{ether,intra,cat}} -X$	0.0

Initial concentrations and number of molecules

	Initial concentration ($mol\ L^{-1}$)	**Initial nr of molecules[b] (-)**
Ethylene diamine[e]	1.7	250000
Bisphenol F diglycidylether[f]	3.4	500000

Diffusion parameters[g]

	V_i^* ($m^3\ kg^{-1}$)	$M_{j,i}$ ($kg\ mol^{-1}$)	$K_{1,i}/\gamma$ ($m^3\ kg^{-1}\ K^{-1}$)	$K_{2,i}$-$T_{g,i}$ (K)	$D_{0,i}$ ($m^2\ s^{-1}$)
Ethylene diamine[h]	1.005 10^{-3}	0.060	8.17 10^{-7}	-175.3	1.5 10^{-8}
Bisphenol F diglycidylether[i]	0.732 10^{-3}	0.312	5.64 10^{-7}	-362.7	1.5 10^{-8}
Lennard Jones parameter	6.0 10^{-10} m				

[a]for intermolecular contributions based on data in Supplementary Figure 13a; reactions in Supplementary Figure 6 and 9; for intramolecular contributions based on data in Supplementary Figure 13b) and Figure 4b in the main text; [b]allowing numerical convergence; [c]$L\ mol^{-1}\ s^{-1}$; [d]autocatalyzed reaction (see Supplementary Discussion); [e]df (degree of functionalization)=4; [f]df=2; [g]based on literature data;[51,60] parameter q in Supplementary equation 14 also here equal to 7; [h]values taken for poly(ethylene); [i]values taken for poly(carbonate).

Supplementary Table 3: Input variables for the kinetic Monte Carlo (*k*MC) simulation (Supplementary Figure S1; box A) for the Diels-Alder network synthesis case (network chemistry 3 in the main text; employed for Figure 4c in the main text); distinction between inter- and intramolecular reactions.

	Equation				**k_{chem} at 353 K[a] ((L mol^{-1}) s^{-1})**
Diels-Alder reaction – intermolecular	$-RAFT + -hexa-2,4-dienyol \xrightarrow{k_{DA,inter}} -DA-$				1.0 10^{-2}
Diels-Alder reaction – intramolecular	$-RAFT + -hexa-2,4-dienyol \xrightarrow{k_{DA,intra}} -DA-$				2.0 10^{-3}
***Initial concentrations and number of molecules*[h]**					
	Initial concentration (mol L^{-1})		**Initial nr of molecules[b] (-)**		
RAFT agent[c]	1.0		250000		
Sorbic alcohol[d]	2.0		500000		
Toluene (solvent)	2.5 10^{-5} L		1.9 10^{9}		
***Diffusion parameters*[e]**					
	V_i^* (m^3 kg^{-1})	**$M_{j,i}$ (kg mol^{-1})**	**$K_{1,i}/\gamma$ (m^3 kg^{-1} K^{-1})**	**$K_{2,i}$-$T_{g,i}$ (K)**	**$D_{0,I}$ (m^2 s^{-1})**
RAFT agent[f]	0.732 10^{-3}	0.983	5.64 10^{-7}	-362.7	1.5 10^{-8}
Sorbic alcohol[g]	0.954 10^{-3}	0.252	6.10 10^{-7}	-111.5	1.5 10^{-8}
Lennard Jones parameter	6.0 10^{-10} m				

[a]for intermolecular contributions based on data in Supplementary Figure 14; reactions in Supplementary Figure 7 and 10 and Figure 4c in the main text; [b]allowing numerical convergence; [c]df (degree of functionalization)=4; [d]df=2; [e]based on literature data;[51,60] parameter q in Supplementary equation 14 also here equal to 7 but multiplied with 1.2 for the Fmoc modification; [f]values taken for poly(carbonate); [g]values taken for poly(butadiene); [h]for Fig. 4c in the main text this becomes 2.5 10^5 RAFT agent and 4.4 10^5 sorbic alcohol molecules for (2-func. linker)$_0$:(4-func. linker)$_0$ = 1.75, 2.5 10^5 RAFT agent and 3.8 10^5 sorbic alcohol molecules for (2-func. linker)$_0$:(4-func. linker)$_0$ = 1.5 and 2.5 10^5 RAFT agent and 2.5 10^5 sorbic alcohol molecules for (2-func. linker)$_0$:(4-func. linker)$_0$ = 1.

Supplementary Table 4: Input parameters and conditions for molecular dynamics (MD) simulations and modifications of MD output; symbol *T* here temperature.

Parameter	Number
Number of atoms	6400
(1) Soft potential to prevent overlap	NVT T = 6000 K 20000 time steps[a]
(2) Annealing parameters simulation	NPT T = 12000 → 6000 K p = 90000 → 60000 bar 10000 time steps[a] T = 6000 → 300 K p = 60000 → 1 bar 100000 time steps[a]
(3) Equilibrating resulting structure	T = 300 K p = 1 bar 10000 time steps[a]

[a]time step = 0.001 ps; total number of time steps = 140000 or 140 ps

Supplementary Table 5: Corrections for intramolecular loops in 3D visualization internal coordinates; shown here up to 12 atom(s) groups (examples regarding box N in Supplementary Figure 2; organosilica-based network case thus network chemistry 1 in the main text; similar for other cases).

Nr of atom(s) groups	Configuration (top view)	3D Bond angle	3D Dihedral angle[a]
4		90	0
6		109.5	60 & (-60)
8	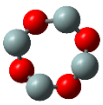	109.5	100 & (-100)
10		109.5	116 & (-116)
12		109.5	127 & (-127)

[a]determined for every number of atom(s) groups (so also > 12) by calculating the dihedral angle between two planes defined by three consecutive atom(s) groups of the intramolecular loops; (x,y,z) coordinates of the atom(s) groups are calculated considering two regular $\frac{n}{2}$ polygons (n = number of atom(s) groups) connecting the red and grey atoms respectively.

Supplementary references

1. D'hooge, D. R., Van Steenberge P. H. M., Reyniers M. F. & Marin G. B. Fed-Batch Control and Visualization of Monomer Sequences of Individual ICAR ATRP Gradient Copolymer Chains. *Polymers* **6,** 1074-1095 (2014).

2. Fierens, S. K., Van Steenberge P. H. M., Reyniers M. F., Marin G. B. & D'hooge D. R. How Penultimate Monomer Unit Effects and Initiator Influence ICAR ATRP of n-Butyl Acrylate and Methyl Methacrylate. *Aiche Journal* **63,** 4971-4986 (2017).

3. Van Steenberge, P. H. M. & Hutchinson R. A. Design of 2-hydroxyethyl methacrylate-functional macromonomer dispersants by semi-batch cobalt chain transfer polymerization. *Aiche Journal* 13

4. Fierens, S. K. et al. An evaluation of the impact of SG1 disproportionation and the addition of styrene in NMP of methyl methacrylate. *Aiche Journal* **64,** 2545-2559 (2018).

5. Payne, K. A. et al. ARGET ATRP of Butyl Methacrylate: Utilizing Kinetic Modeling To Understand Experimental Trends. *Macromolecules* **46,** 3828-3840 (2013).

6. Al-Harthi, M., Soares J. B. R. & Simon L. C. Dynamic Monte Carlo simulation of atom-transfer radical polymerization. *Macromolecular Materials and Engineering* **291,** 993-1003 (2006).

7. Van Steenberge, P. H. M. et al. Kinetic Monte Carlo Generation of Complete Electron Spray Ionization Mass Spectra for Acrylate Macromonomer Synthesis. *Macromolecules* **50,** 2625-2636 (2017).

8. Gegenhuber, T. et al. Fusing Light-Induced Step-Growth Processes with RAFT Chemistry for Segmented Copolymer Synthesis: A Synergetic Experimental and Kinetic Modeling Study. *Macromolecules* **50,** 6451-6467 (2017).

9. Gillespie, D. T. General method for numerically simulating stochastic time evolution of coupled chemical-reactions. *Journal of Computational Physics* **22,** 403-434 (1976).

10. Gillespie, D. T. Exact stochastic simulation of coupled chemical reactions. *The Journal of Physical Chemistry* **81,** 2340-2361 (1977).

11. Wang, L. & Broadbelt L. J. Kinetics of Segment Formation in Nitroxide-Mediated Controlled Radical Polymerization: Comparison with Classic Theory. *Macromolecules* **43,** 2228-2235 (2010).

12. Van Steenberge, P. H. M. et al. Linear Gradient Quality of ATRP Copolymers. *Macromolecules* **45,** 8519-8531 (2012).

13. D'hooge, D. R., Van Steenberge P. H. M., Reyniers M. F. & Marin G. B. The strength of multi-scale modeling to unveil the complexity of radical polymerization. *Progress in Polymer Science* **58,** 59-89 (2016).

14. Barner-Kowollik, C. & Russell G. T. Chain-length-dependent termination in radical polymerization: Subtle revolution in tackling a long-standing challenge. *Progress in Polymer Science* **34,** 1211-1259 (2009).

15. D'Hooge, D. R., Reyniers M. F. & Marin G. B. The Crucial Role of Diffusional Limitations in Controlled Radical Polymerization. *Macromolecular Reaction Engineering* **7,** 362-379 (2013).

16. Tripathi, A. K., Tsavalas J. G. & Sundberg D. C. Monte Carlo Simulations of Free Radical Polymerizations with Divinyl Cross-Linker: Pre- and Postgel Simulations of Reaction Kinetics and Molecular Structure. *Macromolecules* **48,** 184-197 (2015).

17. Achilias, D. S. A Review of Modeling of Diffusion Controlled Polymerization Reactions. **16,** 319-347 (2007).

18. Johnston-Hall, G. & Monteiro M. J. Bimolecular radical termination: New perspectives and insights. *Journal of Polymer Science Part a-Polymer Chemistry* **46,** 3155-3173 (2008).

19. Chaffey-Millar, H., Stewart D., Chakravarty M. M. T., Keller G. & Barner-Kowollik C. A parallelised high performance Monte Carlo simulation approach for complex polymerisation kinetics. *Macromolecular Theory and Simulations* **16,** 575-592 (2007).

20. Van Steenberge, P. H. M., D'hooge D. R., Reyniers M. F. & Marin G. B. Improved kinetic Monte Carlo simulation of chemical composition-chain length distributions in polymerization processes. *Chemical Engineering Science* **110,** 185-199 (2014).

21. Hernández-Ortiz, J. C. et al. Modeling the reaction event history and microstructure of individual macrospecies in postpolymerization modification. **63,** 4944-4961 (2017).

22. Pavlopoulos, G. A., Paez-Espino D., Kyrpides N. C. & Iliopoulos I. Empirical Comparison of Visualization Tools for Larger-Scale Network Analysis %J Advances in Bioinformatics. **2017,** 8 (2017).

23. Garcia-Valverde, M., Cordero N. A. & de la Cal E. S. GAUSSVIEW (R) AS A TOOL FOR LEARNING ORGANIC CHEMISTRY. In: GomezChova L, LopezMartinez A, CandelTorres I (eds). *Edulearn15: 7th International Conference on Education and New Learning Technologies*. Iated-Int Assoc Technology Education a& Development: Valenica, 2015, pp 4366-4370.

24. Burg, J. A. & Dauskardt R. H. Elastic and thermal expansion asymmetry in dense molecular materials. *Nature Materials* **15,** 974 (2016).

25. Burg, J. A. et al. Hyperconnected molecular glass network architectures with exceptional elastic properties. *Nature Communications* **8,** 1019 (2017).

26. Johnson, D. B. Finding All the Elementary Circuits of a Directed Graph. *SIAM Journal on Computing* **4,** 77-84 (1975).

27. Tiernan, J. C. An efficient search algorithm to find the elementary circuits of a graph. *Commun. ACM* **13,** 722-726 (1970).

28. Tang, J., Chen Z., Fu A. W. & Cheung D. W. Capabilities of outlier detection schemes in large datasets, framework and methodologies. *Knowl. Inf. Syst.* **11,** 45-84 (2007).

29. Pouxviel, J. C., Boilot J. P., Beloeil J. C. & Lallemand J. Y. NMR-STUDY OF THE SOL-GEL POLYMERIZATION. *Journal of Non-Crystalline Solids* **89,** 345-360 (1987).

30. Brinker, C. J. HYDROLYSIS AND CONDENSATION OF SILICATES - EFFECTS ON STRUCTURE. *Journal of Non-Crystalline Solids* **100,** 31-50 (1988).

31. Ro, J. C. & Chung I. J. SOL-GEL KINETICS OF TETRAETHYLORTHOSILICATE (TEOS) IN ACID CATALYST. *Journal of Non-Crystalline Solids* **110,** 26-32 (1989).

32. Van Steenberge, P. H. M. et al. Visualization and design of the functional group distribution during statistical copolymerization. *Nature Communications* **10,** 3641 (2019).

33. Karkanas, P. I. & Partridge I. K. Cure modeling and monitoring of epoxy/amine resin systems. I. Cure kinetics modeling. *Journal of Applied Polymer Science* **77,** 1419-1431 (2000).

34. Vyazovkin, S. & Sbirrazzuoli N. Mechanism and kinetics of epoxy-amine cure studied by differential scanning calorimetry. *Macromolecules* **29,** 1867-1873 (1996).

35. Swier, S. et al. Role of complex formation in the polymerization kinetics of modified epoxy-amine systems. *Macromolecules* **38,** 2281-2288 (2005).

36. Buback, M. et al. CONSISTENT VALUES OF RATE PARAMETERS IN FREE-RADICAL POLYMERIZATION SYSTEMS .2. OUTSTANDING DILEMMAS AND RECOMMENDATIONS. *Journal of Polymer Science Part a-Polymer Chemistry* **30,** 851-863 (1992).

37. Vivaldo-lima, E., Hamielec A. E. & Wood P. E. AUTOACCELERATION EFFECT IN FREE-RADICAL POLYMERIZATION - A COMPARISON OF THE CCS AND MH MODELS. *Polymer Reaction Engineering* **2,** 17-85 (1994).

38. Smoluchowski, M. Versuch einer mathematischen theorie der koagulationskinetic kolloider losungen. *Z. Phys. Chem.* **92,** 129-168 (1917).

39. Achilias, D. S. & Kiparissides C. Development of a general mathematical framework for modeling diffusion-controlled free-radical polymerization reactions. *Macromolecules* **25,** 3739-3750 (1992).

40. Vrentas, J. S. & Duda J. L. Diffusion in polymer—solvent systems. I. Reexamination of the free-volume theory. **15,** 403-416 (1977).

41. Vrentas, J. S. & Duda J. L. Diffusion in polymer-solvent systems .2. Predictive theory for dependence of diffusion-coefficients on temperature, concentration, and molecular-weight. *Journal of Polymer Science Part B-Polymer Physics* **15,** 417-439 (1977).

42. Vrentas, J. S. & Vrentas C. M. *Diffusion and Mass Transfer* (CRC Press, London, 2012).

43. Willemse, R. X. E. & van Herk A. M. Copolymerization kinetics of methyl methacrylate-styrene obtained by PLP-MALDI-ToF-MS. *Journal of the American Chemical Society* **128,** 4471-4480 (2006).

44. Marien, Y. W. et al. Kinetic Monte Carlo Modeling Extracts Information on Chain Initiation and Termination from Complete PLP-SEC Traces. *Macromolecules* **50,** 1371-1385 (2017).

45. D.W., v. K. & Klaas t. N. Properties of Polymers *Elsevier* (2009).

46. D'Hooge, D. R., Reyniers M. F. & Marin G. B. Methodology for Kinetic Modeling of Atom Transfer Radical Polymerization. *Macromolecular Reaction Engineering* **3,** 185-209 (2009).

47. D'Hooge, D. R. et al. Assessment of end-group functionality in atom transfer radical polymerization of N-isopropylacrylamide. *European Polymer Journal* **49,** 2344-2355 (2013).

48. D'Hooge, D. R. et al. Atom Transfer Radical Polymerization of Isobornyl Acrylate: A Kinetic Modeling Study. *Macromolecules* **43,** 8766-8781 (2010).

49. Young, R. J. & Lovell P. A. Introduction to Polymers. *CRC press* (2011).

50. Tonge, M. P. & Gilbert R. G. Testing free volume theory for penetrant diffusion in rubbery polymers. *Polymer* **42,** 1393-1405 (2001).

51. Hong, S. U. PREDICTION OF POLYMER-SOLVENT DIFFUSION BEHAVIOR USING FREE-VOLUME THEORY. *Industrial & Engineering Chemistry Research* **34,** 2536-2544 (1995).

52. Yamaguchi, T., Wang B.-G., Matsuda E., Suzuki S. & Nakao S.-I. Prediction and estimation of solvent diffusivities in polyacrylate and polymethacrylates. **41,** 1393-1400 (2003).

53. Achilias, D. S. A review of modeling of diffusion controlled polymerization reactions. *Macromolecular Theory and Simulations* **16,** 319-347 (2007).

54. Russell, G. T., Gilbert R. G. & Napper D. H. CHAIN-LENGTH-DEPENDENT TERMINATION RATE-PROCESSES IN FREE-RADICAL POLYMERIZATIONS .1. THEORY. *Macromolecules* **25,** 2459-2469 (1992).

55. Griffiths, M. C., Strauch J., Monteiro M. J. & Gilbert R. G. Measurement of diffusion coefficients of oligomeric penetrants in rubbery polymer matrixes. *Macromolecules* **31,** 7835-7844 (1998).

56. Mueller, P. A., Storti G. & Morbidelli M. Detailed modelling of MMA dispersion polymerization in supercritical carbon dioxide. *Chemical Engineering Science* **60,** 1911-1925 (2005).

57. Doi, M. & Edwards S. F. DYNAMICS OF CONCENTRATED POLYMER SYSTEMS .1. BROWNIAN-MOTION IN EQUILIBRIUM STATE. *Journal of the Chemical Society-Faraday Transactions Ii* **74,** 1789-1801 (1978).

58. Vilgis, T. A. & Boué F. Brownian motion of chains and crosslinks in a permanently linked network: The dynamic form factor. **26,** 2291-2302 (1988).

59. Stockmayer, W. H. Distribution of Chain Lengths and Compositions in Copolymers. *The Journal of Chemical Physics* **13,** 199-207 (1945).

60. Clay, P. A., Gilbert R. G. & Russell G. T. Molecular weight distributions in free-radical polymerizations .2. Low-conversion bulk polymerization. *Macromolecules* **30,** 1935-1946 (1997).

61. Xia, B. et al. Preparation of silica coatings with continuously adjustable refractive indices and wettability properties via sol–gel method. *RSC Advances* **8,** 6091-6098 (2018).